Dissertation

submitted to the
Combined Faculties for the Natural Sciences and for Mathematics
of the Ruperto-Carola University of Heidelberg, Germany
for the degree of
Doctor of Natural Sciences

presented by

Dipl.-Phys. Ruth Barth

born in Sinsheim, Germany

Oral examination: May 14th, 2008

Digital In-Line X-Ray Holographic Microscopy with Synchrotron Radiation

This dissertation was carried out at the
Institute of Physical Chemistry

Referees

Prof. Dr. Michael Grunze

Prof. Dr. Annemarie Pucci

Digitale in-line röntgenholographische Mikroskopie mit Synchrotronstrahlung

In-line Holographie kann als eine linsenlose Mikroskopietechnik verwendet werden, welche dreidimensionale Bilder des Objektes liefert und deren Auflösung nur von der verwendeten Wellenlänge und der numerischen Apertur des Systems abhängt. In der vorliegenden Arbeit wurde Holographie in der in-line Geometrie mit Wellenlängen im vakuum-ultravioletten und weichen Röntgenbereich verwendet. Durch Beugung der Synchrotronstrahlung an Lochblenden mit geeignetem Durchmesser wurden divergente Wellenfronten erzeugt. Das holographische Interferenzmuster wurde mit einer CCD-Kamera aufgenommen, und die Bilder wurden mit Hilfe der Kreuzer-Implementierung der Kirchhoff-Helmholtz-Transformation numerisch rekonstruiert. Mit dieser Mikroskopietechnik wurden lithographische Strukturen in Photolack, Mischungen aus Polystyrolkugeln und Eisenoxidpartikeln, und getrocknete biologische Proben wie Rattenfibroblasten, die Grünalge *Ulva linza* und menschliche Chromosomen abgebildet. Die erreichte Auflösung wurde über verschiedene Kriterien bestimmt und mit den theoretischen Vorhersagen verglichen. Es konnte gezeigt werden, dass durch Erhöhung der numerischen Apertur mittels kleinerer Lochblendendurchmesser und durch nachträgliche Korrektur des Abdriftens der Probe die experimentell erreichte Auflösung von $\delta_{\mathrm{exp}} = 1.13 \pm 0.35$ µm auf $\delta_{\mathrm{exp}} = 0.37 \pm 0.04$ µm verbessert werden konnte. Dieser Wert entspricht den theoretischen Erwartungen. Desweiteren konnte durch Aufnahmen bei verschiedenen Wellenlängen ein Kontrast zwischen unterschiedlichen chemischen Elementen erzeugt werden.

Digital in-line X-ray holographic microscopy with synchrotron radiation

In-line holography is a lensless microscopy method yielding three-dimensional images of the object, where the resolution limit depends on the illuminating wavelength and the numerical aperture of the system, only. In this work, an in-line holographic setup was implemented with radiation in the vacuum-ultraviolet and soft X-ray region. Diverging wavefronts were generated by diffraction of the synchrotron radiation from a pinhole with suitable diameter. The holographic interference pattern was recorded with a CCD camera, and the images were numerically reconstructed using the Kreuzer implementation of the Kirchhoff-Helmholtz transform. With this microscopic technique, lithographic structures in photo resist, mixtures of polystyrene beads and iron oxide particles, and dried biological samples such as rat embryonic fibroblast cells, green algae *Ulva linza*, and human chromosomes were imaged. The achieved resolution was determined via different criteria and was compared to the theoretical expectations. It was shown, that by increasing the numerical aperture with smaller pinholes and by correcting for drift effects, the experimental resolution could be improved from $\delta_{\mathrm{exp}} = 1.13 \pm 0.35$ µm to $\delta_{\mathrm{exp}} = 0.37 \pm 0.04$ µm, meeting the theoretical prediction of $\delta_{\mathrm{theo}} = 0.34$ µm. Furthermore, by recording holograms at different energies, element contrast was obtained.

Contents

1 Introduction and Context

For a broad range of natural sciences, foremost physics, biology, medicine, and material sciences, optical imaging of smaller and smaller structures becomes more and more essential. Therefore various techniques, each with its own advantages and disadvantages and fields of application, have been developed.

With approximately 400 years the oldest and still most common technique is optical light microscopy. It is easily applicable and the only requirement is sufficient transparency, so thin samples (up to the mm range) are preferred. Also, living systems can be examined in solution without damaging them. But with the discovery of the so called diffraction limit by the German mathematician and physicist Ernst K. Abbe [1], it became clear that even with perfect lenses objects less than

$$\delta_{lat} \approx \frac{\lambda}{2n \sin \theta} \tag{1.1}$$

apart cannot be resolved. Here, λ is the wavelength of the light used, n is the refractive index of the medium, and the semi aperture angle of the lens is denoted as θ. Since up to now the best numerical apertures ($\mathrm{NA} = n \sin \theta$) range from 0.95 for dry to 1.42 for oil immersion objectives ($n_{oil} = 1.52$) [2, 3], structures smaller than 200 nm are not discernible using visible light. To circumvent this barrier, great efforts have been taken and numerous different techniques arose.

The next popular far-field method, Fluorescence Microscopy, does not yield better spatial resolution, but since most dyes bind specifically to certain tissue in cells, the identification of cells and sub-microscopic cellular components with a high degree of specificity even down to single molecule level is achieved. Therefore, the sample must be intrinsically fluorescent or must be stained with a fluorescent dye, which is sometimes difficult with living cells. Normally, the cell has to be permeabilized so that the dye can be introduced. In addition to that, since the fluorescence photons must be able to leave the sample and reach the detector, thin samples are preferred.

An important step toward better depth resolution was the development of Confocal Laser Microscopy. By introducing two pinholes at the two focal spots of the microscope and thus blocking the light that arrives at the detector from planes in the sample other than the focal plane, depth resolutions of 500 to 900 nm are attained with lateral resolution of 200 nm [4]. This does not yet break the diffraction barrier, but improves the depth resolution, since noise effects are lessened.

Taking images at several focal depths provides full 3D information. However, this makes Confocal Laser Microscopy a scanning method, so dynamics cannot be observed. Additionally, when using it as a Confocal Fluorescence Microscope, the sample is exposed to high energy radiation which might damage it, because of the low quantum efficiency of fluorophores and since a major part of the light is blocked by the pinhole.

A different approach to better resolution is abandoning visible light in favor of smaller wavelengths as probes. As it becomes clear from equation (1.1), resolution is linearly dependent on the wavelength of the probe. Therefore, using soft X-rays (λ =0.1 to 10 nm) or even electrons (E =20 to 200 eV [5]) structures as small as 30 nm (X-rays) [6] down to 0.2 nm (electrons) can be resolved.

There are two types of Electron Microscopes, surface sensitive Scanning Electron Microscope (SEM) or Transmission Electron Microscope (TEM). Both variants require high vacuum to prevent signal losses through collisions with the remaining gas. Therefore dehydrated or frozen samples are needed. Moreover, SEM needs conductive samples, and in TEM only thin slices up to 100 nm can be penetrated [6]. However, resolutions down to 2 nm can be achieved. Charging effects and impairment by energy exposure are possible disadvantages [7].

In X-Ray Microscopy, the specimen can be observed in solution and at atmospheric pressure, sample thicknesses up to 10 µm are possible. Operating at the so called water window (λ =2.34 to 4.38 nm), the different absorption cross sections yield good contrast between water (oxygen) and proteins (carbon) without staining [6, 8]. Additionally, a 3D tomographic setup is possible, where several 2D projections are recorded and later digitally combined to a full 3D object [9]. But the price of longer acquisition times has to be paid, and high exposure doses might damage biological samples. A means to minimize the radiation damage is cryogenic preparation [6].

Compared to electron microscopy, an important advantage of X-rays is their large penetration depth. Thus, biological samples can be observed without preparation in thin slices [10]. A second advantage is that the photon energy of synchrotron radiation can be varied over a large energy region. With spectroscopic methods it is therefore possible to obtain chemical information of a sample with high spatial resolution down to 15 to 50 nm [8, 10, 11, 12, 13, 14]. The limiting factor for the achievable resolution is the quality and the focal length of the zone plates [15].

Other scanning non-optical techniques, so called Near-Field Microscopy, as Atomic Force Microscope (AFM) and Scanning Tunneling Microscope (STM), reach atomic resolution but are purely surface sensitive [16, 17, 18, 19]. (Scanning) Near-Field Optical Microscopy (SNOM) combines those non contact methods with near-field optical measurements, so that not only the topography but also the optical properties of the sample can be determined with resolutions as small as 20 nm [20]. Yet, those methods are bound to the surface of the sample and the technical

demands are high.

In light microscopy, there are two principle approaches to achieve resolution below the diffraction limit using interference techniques. Firstly, at M. Gustafssons lab at University of California, San Francisco, the image of a fluorescent sample is detected by two opposing object lenses that are focused on the same plane within the sample. The light of both beams interferes on the CCD camera forming an interference pattern that holds high resolution information about the axial position of the respective molecule. They named this method 'image interference microscopy', I^2M [21]. If, instead, the sample is illuminated through both lenses, the intensity varies along the axial direction, enabling more selective excitation similar to standing wave microscopy. This is referred to as 'incoherent interference illumination', I^3 [21]. Combining both techniques, that is illuminating and detecting through both lenses, gives I^5M, a wide field fluorescence microscopy method with axial resolution better than 100 nm. Since the full plane of focus can be recorded in a single image, the acquisition of a $512 \times 512 \times 160$ pixel data set only takes 10 to 20 min [21].

In the second approach, a major breakthrough in bypassing the diffraction limit was achieved by the group of Stefan Hell at the Max Planck Institute for Biophysical Chemistry in Göttingen. In 2005, they attained spatial resolution down to 16 nm in the focal plane [22]. They achieve this by combining two methods: 4Pi Microscopy and Stimulated Emission Depletion (STED) [23]. 4Pi Microscopy is similar to I^5M, with the difference that it is in a confocal setup [24]. STED restricts fluorescence to spot sizes of 16 nm in the focal plane and 33 nm axial resolution [25] by exciting molecules with a laser pulse and then depleting the vicinity of the focal spot by a doughnut shaped redshifted pulse inducing stimulated emission. While pure 4Pi Microscopy is compatible with living cells [24, 26], the high intensities demanded in STED inflict photostress on the dye that leads to bleaching and live cell incompatibility [23]. On the other hand, STED is not restricted to fluorescence, but any photostable three-level system with adequate excited state lifetimes and considerable cross-sections for stimulated emission qualifies [25].

Recapitulating one can say, of those methods mentioned above, one part has the capability to measure in-situ with high temporal resolution, but lacks high spatial resolution, the other part achieving good spatial resolution, but does not work under in-situ conditions and images are often taken in scanning mode.

Demand is there for a technique that combines the following important criteria:

- Simultaneous capture of the whole image with high acquisition frequency
- 3D information in one picture
- High spatial resolution in three dimensions
- In-situ capability

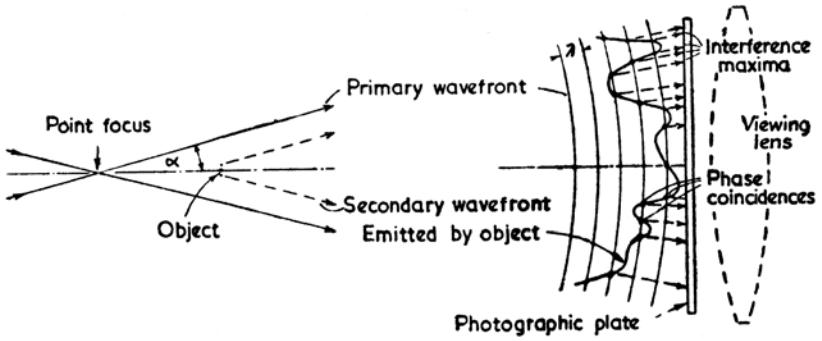

Fig. 1. INTERFERENCE BETWEEN HOMOCENTRIC ILLUMINATING WAVE AND THE SECONDARY WAVE EMITTED BY A SMALL OBJECT

Figure 1.1: Gabor's original holography setup
This is Gabor's drawing of his setup as published in his article 'A New Microscopic Principle' [27]. A diverging reference wave (primary wavefront) illuminates an object. Part of the wave is scattered by the object. This secondary wave interferes with the reference wave, and the interference pattern is recorded on a photographic plate.

Almost 60 years ago D. Gabor proposed 'A New Microscopic Principle' capable to circumvent the diffraction barrier due to being completely lensless [27]. Therefore, the resolution is limited only by the wavelength and the numerical aperture of the setup. Additionally, though unintended by Gabor, all 3D information of the mapped object is contained in one single image. What he named 'electron interference microscope' is now known as holography (from Greek: *holos = complete, integral* and *graphein = to write*) due to its property to record all 3D information in one single image. But how does it work?

Image recording devices such as photo plates or modern CCD cameras only record the amplitude but not the phase of the light impinging on it. But the phase is crucial for complete 3D information. However, the interference pattern generated by superimposing two components of coherent light—one fraction interacts with the object (object wave) while the other part reaches the detector undisturbed (reference wave)—contains amplitude and phase information in its intensity profile. The image can be optically or digitally reconstructed revealing full 3D information of the object. Originally suggested for electrons [27, 28, 29, 30], holography can also be performed with photons [31, 32], neutrons [33], X- [34, 35, 36, 37], and γ-rays [38, 39], if only the coherence length is sufficiently large.

Three basic setups can be distinguished, off axis, in-line and Fourier geometry [40, 41]. Gabor's initial proposal used in-line geometry (see figure 1.1) [27]. An electron beam is brought to a fine focus, then diverges, one part interacts with the object and interferes with the primary wavefront at the detector, a

photographic plate, where the interference pattern is recorded. This pattern does not necessarily resemble the object since it is recorded in great distance to it. The only required properties for the sample are a preferably small size and mounting on a transmittive support, so that a considerable part of the reference wave reaches the detector. For reconstructing the image one develops the photograph by reversal and then illuminates it with an optical imitation of the electronic wave. An observer looking through the slide sees the original object behind it, but will also see a second image of the object at the same distance in front of the hologram. This undesired twin image superimposes the reconstructed images and disturbs it since it is out of focus leading to a poor image quality. Another drawback is the strong coherent background from the directly transmitted beam. Those disadvantages were the reason that Gabor's method did not find much attention. Until 14 years later, when E.N. Leith and J. Upatnieks introduced an off axis setup [42]. In this configuration the object beam is spatially separated from the reference beam, resulting in image and twin image sufficiently far apart from each other and from the reference beam. Additionally, with the invention of the laser in 1960 coherent light sources were available, an important step was done to developing holography as an imaging technique.

One also distinguishes between applying parallel or spherical waves as probes [40]. While plane waves are used in the off axis as well as in the in-line geometry, spherical waves are used exclusively in the in-line setup. For producing a spherical wavefront, a small pinhole is placed in the beam path of the probe beam. If the diameter of the pinhole is of the order of the wavelength of the light, a spherical wave propagates behind it. Although using plane waves is experimentally slightly easier, spherical waves have one big advantage. Because of the radial propagation of the light a magnifying effect occurs, so holography with spherical waves can be considered a microscopy technique [40, 41].

Digital in-line holography with spherical waves at optical wavelengths has been impressively demonstrated in the group of Kreuzer at Dalhousie University, Halifax [43]. Three dimensional imaging of biological samples like diatom, *Ditylum brightwellii*, and the head of the fruit fly, *Drosophila melanogaster*, is routinely performed with lateral and depth resolution at least at the micron level [29, 43, 44]. The three dimensional positions of microspheres can be determined within an accuracy of a few hundred nanometers [45]. Due to the large focal depth of the technique, volumes up to several cubic centimeters can be recorded in one single hologram, and by collecting several holograms over an extended time period, particle tracking in four dimensions is possible [31, 32]. In analogy to optical microscopy, oil immersion techniques can be applied to enhance the achievable resolution [46].

As mentioned above, in holography the resolution is not limited by diffraction, since no lenses are needed, it only depends on the wavelength λ and the numerical aperture NA of the setup. Therefore, the lateral and depth resolution are given

by [31]

$$\delta_{\text{lateral}} \approx \frac{\lambda}{2\text{NA}} \quad \text{and} \tag{1.2}$$

$$\delta_{\text{depth}} \approx \frac{\lambda}{2\text{NA}^2}, \tag{1.3}$$

$$\text{with} \quad \text{NA} = \frac{D/2}{L}. \tag{1.4}$$

As can be seen from equation (1.4), the numerical aperture is only constrained by the ratio of the detector size D to the distance L between source and detector. Otherwise, any desired resolution should in principle be achievable. Already in 1987, it could be shown, that spatial resolution as small as 40 nm using an synchrotron radiation can be achieved [47], although exposure times of one hour or longer were needed. In the same year, the applicability of X-ray lasers in holography has been demonstrated [48], where a resolution of 10 µm was demonstrated. So the problem of sufficiently coherent X-ray sources was solved. Almost one decade later, holograms from complex biological specimen recorded with soft X-rays in the water window generated by synchrotron radiation achieved a resolution of 40 nm [49]. Those holograms were recorded in a photoresist and reconstructed after readout with atomic-force micrsocsopy (AFM). By digitally recording several holograms from various positions and using tomographic principles for reconstruction, three dimensional images with a resolution of 1 µm were achieved with soft X-ray holography [34]. Soft X-rays with full spatial coherence can be generated by high-order harmonics [50]. Employing them in digital in-line holographic microscopy, 800 nm resolution was obtained [50].

Concerning the Fourier approach to X-ray holography, experiments have been performed in the groups of McNulty [51] and Eisebitt [52, 53]. Both groups use the lensless geometry, and spatial resolutions down to 50 nm and below are reported for gold patterns [51] and magnetic nanostructures [52, 53]. Also in this geometry, holographic tomography is possible, yielding three-dimensional imaging of gold-bar pattern [10]. In the optical implementation, color holographic images have been presented [54].

A new development is off-axis holography with hard X-rays [35]. Coherent cone beams are formed by a pair of X-ray waveguides, the obtained hologram is digitally reconstructed. Spatial resolution of about 100 nm has been achieved, and the approach of the fundamental limit of 10 nm is predicted [35].

On the other hand, X-ray holography with atomic resolution is reported [55]. This technique, also called X-ray fluorescence microscopy (XFM), differs from the ones introduced above. It was first proposed by A. Szöke almost 20 years ago [56]. In this case, the atoms in a periodic structure like a singlecrystal are exited by an X-ray source. The atoms themselves serve as internal sources when emitting coherent fluorescence radiation during the relaxation process. Part

of this wavefront will reach the detector directly forming the reference wave, while the other part will interact with the surrounding atoms on the way to the detector and there interferes with the reference wave. Moving the detector around the sample, an angle-dependent intensity distribution is recorded which is the hologram. The reconstruction reveals the average vicinity of one atom in real space. A very similar method, the so called 'inverse' XFM, switches the positions of source and detector [39, 57]. External radiation reaches the atoms in the sample either directly or after scattering elastically off neighboring atoms, interfering at the place of the atom. Hence, the strength of the fluorescence emitted by an atom depends on the intensity of the interference, and is recorded by the detector. The detector stays fixed, while the radiation source is moved around the sample. Using those two methods, the atomic structure of several crystals was reconstructed [57, 58], even light atoms could be imaged [59].

Today, all those methods employ numerical means of image reconstruction rather than optical means. Probably all reconstruction algorithms use the Kirchhoff-Helmholtz formula, which is a Fourier transformation of the hologram, as presented by J.J. Barton [60]. In the same paper, Barton suggests recording holograms at several wavelengths, since properly phased combinations of these reconstructions will yield better twin image suppression and resolution enhancement, especially in axial direction. Experiments testing this Multiple-Energy X-Ray Holography (MEXH) were performed and confirmed the predictions [57, 58, 59].

Another method, which is related to holography, has been developed in the past years, which is called diffraction microscopy. It corresponds to an implementation of holography without a reference wave. Therefore, the image cannot be reconstructed via the Kirchhoff-Helmholtz transform, but an iterative phase retrieval is necessary. Nevertheless, three-dimensional reconstruction of a noncrystalline nanostructured material at 50 nm resolution [61] and two-dimensional imaging of a biological sample at 30 nm [62] have been reported. Even 7 nm resolution was obtained for non-periodic test pattern [63].

With the realization of sources for extremely brilliant, coherent and ultrashort X-rays such as free electron lasers (for example FLASH at DESY, Hamburg), new possibilities for those imaging methods arise. Due to the ultrashort pulses, diffraction pattern of biological samples without radiation damage may be recorded before the sample explodes and turns into a plasma [64]. Test structures have been imaged with 62 nm resolution [64]. Also, the dynamics of the explosion of polystyrene spheres have been examined with time-delay X-ray holography [65].

Altogether, the field of holography has widely spread in the past 60 years, such that the overview given above is far from exhaustive.

In summary, X-ray holography is a method which is capable of contributing to life-science investigations in the future [10], since it has the potential of low spatial resolution, provides a means for three-dimensional imaging, and is suitable to

flash exposures—at least in its two-dimensional form [10].

The experiments presented in this thesis were performed in in-line geometry with spherical waves. Coherent X-rays generated by synchrotron radiation were used as probe. The divergent wavefronts were obtained by diffraction from a pinhole of appropriate diameter. The holograms were recorded digitally on a CCD-chip, and the images were reconstructed numerically on a computer using a Kreuzer implementation of the Kirchhoff-Helmholtz transform.

In the following chapter, an introduction to the basic theory of holography will be given. Details of the experimental setup as well as the generation of X-rays by synchrotron radiation will be the topic of the subsequent chapter. Since the resolution limit is an important parameter for imaging systems, the resolution limit of digital in-line holography will be derived and the parameters, which influence this limit will be discussed in chapter 4. The pinholes and the samples which were used in the experiments are described in the next two chapters. Experimental results obtained in the course of this thesis are presented in chapter 7 to chapter 9, and the achieved resolution will be determined. Finally, an outlook to future experimental development concludes this work.

2 Theory of Holography

In this chapter, the fundamental theory of digital in-line holography shall be introduced. The main focus will be put on the formation of holograms and the reconstruction of the image from the hologram. Other experimental geometries than the in-line setup will be briefly discussed. This introduction is based on corresponding chapters in common textbooks [40, 41, 66, 67, 68, 69, 70].

Since the basic mechanisms for holography—interference and diffraction—are wave phenomena, first a short overview over the properties of light waves necessary for the subsequent theory of holography will be given. A more detailed introduction can be found in most optics textbooks, the one presented here coarsely follows [40, 41, 69, 70].

2.1 Properties of light waves

2.1.1 Wavefunction and complex amplitude

Light as an electromagnetic wave can be described by a complex wavefunction. A monochromatic wave can be represented by the harmonic wavefunction [41]

$$U(\vec{r},t) = A_0(\vec{r}) \exp\{i\varphi(\vec{r})\} \exp\{i\omega t\}, \tag{2.1}$$

where $A_0(\vec{r})$ is the amplitude, $\varphi(\vec{r})$ the phase, and $\omega = 2\pi\nu$ the angular frequency. This wavefunction describes the wave completely and satisfies the wave equation [41, 69]

$$\nabla^2 U - \frac{1}{c^2}\frac{\partial^2 U}{\partial t^2} = 0. \tag{2.2}$$

Here, ∇^2 is the Laplace operator [41, 69],

$$\nabla^2 = \frac{\partial^2}{\partial x^2} + \frac{\partial^2}{\partial y^2} + \frac{\partial^2}{\partial z^2}, \tag{2.3}$$

and c the speed of light. Inserting equation (2.1) in the wave equation (2.2) leads to the time-independent Helmholtz equation [69]

$$\nabla^2 A(\vec{r}) + k^2 A(\vec{r}) = 0, \tag{2.4}$$

where $k = \omega/c = 2\pi\nu/c$ is called the wavenumber, and $A(\vec{r})$ is the time-independent factor in equation (2.1)

$$A(\vec{r}) = A_0(\vec{r}) \exp\{i\varphi(\vec{r})\}, \tag{2.5}$$

which is referred to as complex amplitude [69]. Wavefronts are surfaces of equal phase, that is where $\varphi(\vec{r}) = \text{const.}$.

Physical quantities as for example the modulus of the electric field vector $E(\vec{r}, t)$ are given by the real part of the corresponding complex wavefunction [41]

$$\begin{aligned} E(\vec{r}, t) &= \Re\{U(\vec{r}, t)\} \\ &= A_0(\vec{r})\, \Re\{\exp\{i\varphi(\vec{r})\} \exp\{i\omega t\}\} \\ &= A_0(\vec{r}) \cos\{\omega t + \varphi(\vec{r})\}. \end{aligned} \tag{2.6}$$

However, this quantity is not observable. The human eye as well as recording media only perceive intensities.

The optical power per unit area, the intensity $I(\vec{r}, t)$, is calculated by averaging the squared wavefunction over a time interval which is much longer than the period $T = 1/\nu$ [69]. It is thus given by

$$I(\vec{r}) = \frac{1}{2}\epsilon_0 c\, |A(\vec{r})|^2 = \frac{1}{2}\epsilon_0 c\, A^*(\vec{r})\, A(\vec{r}), \tag{2.7}$$

with $A^*(\vec{r})$ being the complex conjugate of $A(\vec{r})$. For a monochromatic wave, the intensity does not vary with time [69]. The constant factor $1/2\epsilon_0 c$, where ϵ_0 is the vacuum permittivity, is usually neglected in practical calculations [41].

2.1.2 The plane wave and the spherical wave

Two simple solutions of the Helmholtz equation (2.4) are the plane wave and the spherical wave. The plane wave is described by the complex amplitude [69]

$$A(\vec{r}) = A_0 \exp\{-i\vec{k} \cdot \vec{r} - \varphi_0\}. \tag{2.8}$$

A_0 is called amplitude, and φ_0 is a phase offset. The wavefronts are parallel planes perpendicular to the wavevector $\vec{k} = k\vec{n}$, where $\vec{n}$ is a unit vector in propagation direction. The distance between two wavefronts $\lambda = c/\nu$ is named wavelength [69]. So the modulus of the wavevector, the wavenumber k, and the wavelength λ are connected via

$$k = \frac{2\pi}{\lambda}. \tag{2.9}$$

The intensity of a plane wave, $I(\vec{r}) = |A_0|^2$, is constant in space [69].

A spherical wave is given by the complex amplitude [69]

$$A(\vec{r}) = \frac{A_0}{r} \exp\{-ikr - \varphi_0\}, \tag{2.10}$$

where r is the distance from the origin. The wavefronts are concentric spheres separated by the radial distance λ, the intensity $I(\vec{r}) = |A_0|^2/r^2$ decreases with increasing distance from the origin.

2.1.3 Interference

In general, more than one wavefunction is present in a certain region of space and time. Since the wave equation 2.2 is a linear differential equation, the resulting total wavefunction is the sum of the individual functions. This superposition is called interference [41]. Here, monochromatic waves with equal frequency (and polarization) are regarded.

Two waves with complex amplitudes

$$\begin{aligned} A_1(\vec{r}) &= a_1 \exp\{i\varphi_1\} \qquad \text{and} \\ A_2(\vec{r}) &= a_2 \exp\{i\varphi_2\} \end{aligned} \tag{2.11}$$

result again in one monochromatic wave with the same frequency and the complex amplitude [41]

$$A(\vec{r}) = A_1(\vec{r}) + A_2(\vec{r}). \tag{2.12}$$

According to equation (2.7), the total intensity now is [41]

$$\begin{aligned} I(\vec{r}) &= |A_1(\vec{r}) + A_2(\vec{r})|^2 = (A_1(\vec{r}) + A_2(\vec{r}))^*(A_1(\vec{r}) + A_2(\vec{r})) \\ &= A_1^*(\vec{r})A_1(\vec{r}) + A_2^*(\vec{r})A_2(\vec{r}) + A_1^*(\vec{r})A_2(\vec{r}) + A_2^*(\vec{r})A_1(\vec{r}) \\ &= a_1^2 + a_2^2 + 2a_1a_2\cos\{\varphi_1 - \varphi_2\} \\ &= I_1 + I_2 + 2\sqrt{I_1 I_2}\cos\{\varphi\}. \end{aligned} \tag{2.13}$$

The individual intensities are $I_1 = a_1^2$ and $I_2 = a_2^2$, and the phase difference is $\varphi = \varphi_1 - \varphi_2$. So the total intensity is not just the sum of the individual intensities, but the so called interference term $2\sqrt{I_1 I_2}\cos\{\varphi\}$ has to be added, which can be positive or negative. This term causes a modulation of the intensity visible as dark and bright fringes depending on the phase difference φ. At points where φ is an even multiple of π,

$$\varphi = 2n\pi, \qquad n \in \mathbb{Z}, \tag{2.14}$$

the intensity reaches its maximum, $I_{\max} = I_1 + I_2 + 2\sqrt{I_1 I_2}$. This is called constructive interference [41, 69]. At points where φ is an odd multiple of π,

$$\varphi = (2n+1)\pi, \qquad n \in \mathbb{Z}, \tag{2.15}$$

the intensity reaches its minimum, $I_{\min} = I_1 + I_2 - 2\sqrt{I_1 I_2}$. This is called destructive interference [41, 69]. The visibility of the interference fringes is defined as [41]

$$V = \frac{I_{\max} - I_{\min}}{I_{\max} + I_{\min}} = \frac{2\sqrt{I_1 I_2}}{I_1 + I_2}. \tag{2.16}$$

It is a measure for the contrast of the interference pattern.

2.1.4 Coherence

The prerequisite for interference phenomena is a constant correlation of the phases of the contributing waves. The correlation of a wave with itself at different points in time is described by temporal coherence, while the correlation of different parts of the same wavefront is described by spatial coherence.

Temporal coherence

Light emitted from a single source does not consist of a single wave but of different wave trains with finite length L and statistical phase difference. Only partial waves belonging to the same wave train have a constant phase correlation and can interfere with each other. Therefore, the length of the wave train, L, is called coherence length. The corresponding time

$$\tau = \frac{L}{c} \tag{2.17}$$

is named coherence time [41]. A wave train of length L corresponds to light with spectral width $\Delta\nu$, so the coherence length can be expressed as [41]

$$L = \frac{c}{\Delta\nu} = \frac{\lambda^2}{\Delta\lambda}. \tag{2.18}$$

Monochromatic light, that is having a narrow bandwidth, therefore has a long coherence length.

The coherence length of a light bulb is in the range of some micrometers, while the coherence lengths of lasers can be from some millimeters (e. g. a multi-mode diode laser) up to several hundred meters (e. g. a stabilized single mode Nd:YAG-laser) [41].

Spatial coherence

In the considerations above, a point source was assumed. However, real light sources are extended sources, and the size of the source influences the interference

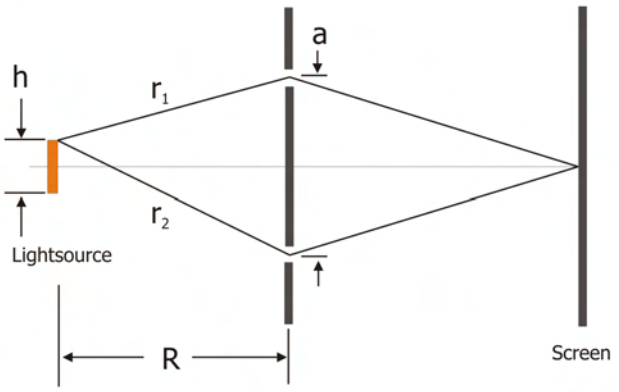

Figure 2.1: Young's interferometer
Light emitted by an extended light source passes an aperture with two holes separated by a distance a. The resulting interference pattern is observed on a screen. If the distance of the holes exceeds a critical distance a_k, the path difference is larger than $\lambda/2$, and the interference pattern vanishes. After [41].

phenomena. In figure 2.1 the schematic of a Young's interferometer is depicted. With this interferometer, the coherence distance of the extended light source can be measured. Light emitted by the source passes an aperture with two holes separated by a distance a. The resulting interference pattern is observed on a screen. If the distance of the holes exceeds a critical distance a_k, the interference pattern vanishes. This distance is called coherence distance [41].

Every point of the source emits light incoherently with respect to the other points, so an interference pattern is only visible, if for every point of the source the optical path difference $r_2 - r_1$ satisfies [41]

$$r_2 - r_1 < \frac{\lambda}{2}. \tag{2.19}$$

The optical path difference is largest for the edges of the source. If the source is of width h in a distance R to the aperture, for a point at the edge follows

$$\begin{aligned} r_1^2 &= R^2 + \left(\frac{a-h}{2}\right)^2 \qquad \text{and} \\ r_2^2 &= R^2 + \left(\frac{a+h}{2}\right)^2. \end{aligned} \tag{2.20}$$

Assuming that $a \ll R$ and $h \ll R$ it follows [41]

$$r_2 - r_1 \approx \frac{ah}{2R}. \tag{2.21}$$

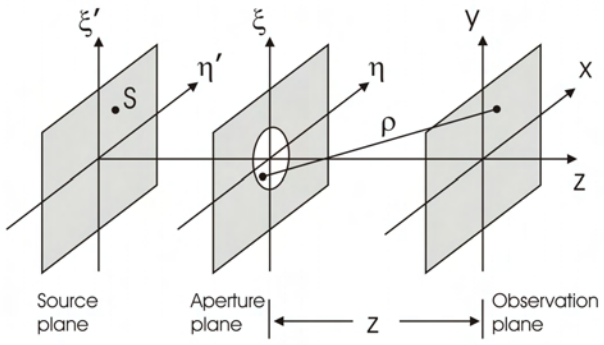

Figure 2.2: Coordinate system for the Fresnel-Kirchhoff integral
A spherical wave emitted by the source lying in the source plane illuminates an aperture. The resulting diffraction pattern is observed in the observation plane. After [41].

Inserted in equation (2.19), this leads to

$$\frac{ah}{2R} < \frac{\lambda}{2}. \tag{2.22}$$

So the relation for the coherence distance a_k is [41]

$$\frac{a_\mathrm{k} h}{2R} < \frac{\lambda}{2}. \tag{2.23}$$

The spatial coherence thus not only depends on the properties of the light source, but is also influenced by the geometry of the interferometer.

2.1.5 Diffraction

Besides interference, light waves show another interesting phenomenon, diffraction. If the dimensions of an obstacle hit by a light wave are in the range of the wavelength, effects differing from geometrical optics occur. For example, a light wave illuminates an opaque screen with a small transparent hole, and the result is examined on a screen on the other side. From geometrical optics, one would expect a uniformly bright spot of the size of the hole surrounded by shadow. A closer look however reveals a pattern of bright and dark regions. This effect is due to diffraction.

A qualitative explanation is given by Huygens' principle, stating that "every point of a wavefront can be considered as a source point for secondary spherical waves. The wavefront at any other place is the coherent superposition of these secondary waves." [41]

A quantitative description is given by the Fresnel-Kirchhoff integral [41]

$$\Gamma(x,y,z) = \frac{i}{\lambda}\int_{-\infty}^{\infty}\int_{-\infty}^{\infty} A(\xi,\eta)\frac{\exp\left\{-i\frac{2\pi}{\lambda}\rho\right\}}{\rho}Qd\xi d\eta \tag{2.24}$$

with

$$\rho = \sqrt{(x-\xi)^2+(y-\eta)^2+z^2}. \tag{2.25}$$

This integral can be derived from the Kirchhoff-Helmholtz integral theorem, as shown in [71]. The underlying coordinate system is depicted in figure 2.2. $A(\xi,\eta)$ is the complex amplitude of the wave in the aperture plane. Since according to Huygens, every point (ξ,η) within the hole in the aperture is a source of a spherical wave, the wavefront Γ at any point (x,y) in the observation plane is the superposition of all those spherical waves. This superposition is expressed by the integral. The amplitude of each spherical wave is proportional to the amplitude $A(\xi,\eta)$ of the original wave at the aperture plane. The inclination factor Q is introduced to exclude the propagation of the secondary spherical waves back in direction towards the source. For most practical situations $Q \approx 1$.

If z is much larger than $|x-\xi|$ and $|y-\eta|$, based on Taylor series expansion [72] ρ can be approximated as [69]

$$\rho \approx z + \frac{(x-\xi)^2+(y-\eta)^2}{2z}. \tag{2.26}$$

Since behind the obstacle the wave is not disturbed, it is

$$\Gamma(x,y,z) = \Gamma_0(x,y,z)\exp\left\{-i\frac{2\pi}{\lambda}z\right\}. \tag{2.27}$$

Furthermore, it can be approximated

$$\frac{A(\xi,\eta)}{\rho} \approx \frac{A(\xi,\eta)}{z}. \tag{2.28}$$

Then equation (2.24) can be written as

$$\begin{aligned}
\Gamma_0(x,y,z) &= \frac{i}{\lambda z}\int_{-\infty}^{\infty}\int_{-\infty}^{\infty} A(\xi,\eta)\exp\left\{-i\frac{\pi}{\lambda z}\left[(x-\xi)^2+(y-\eta)^2\right]\right\}d\xi d\eta \\
&= \frac{i}{\lambda z}\int_{-\infty}^{\infty}\int_{-\infty}^{\infty} A(\xi,\eta)\exp\left\{-i\frac{\pi}{\lambda z}\left[x^2+y^2\right]\right\} \\
&\quad \times \exp\left\{-i\frac{\pi}{\lambda z}\left[\xi^2+\eta^2\right]\right\} \\
&\quad \times \exp\left\{i\frac{2\pi}{\lambda}\left[\xi x/z+\eta y/z\right]\right\}d\xi d\eta.
\end{aligned} \tag{2.29}$$

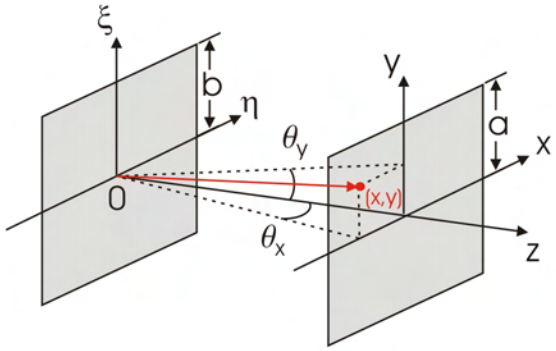

Figure 2.3: Coordinate system for the Fraunhofer integral
When the propagation distance z of the wave is sufficiently long, only one plane wave contributes to the complex amplitude at each point (x, y) in the image plane. This wave travels at angles θ_x, θ_y. After [69].

This equation is known as Fresnel integral [69, 70].

Regarding the wave in the far field, that is for

$$z \gg \frac{b^2}{\lambda} > \frac{\xi^2 + \eta^2}{\lambda}, \tag{2.30}$$

the second exponential factor is close to unity. This condition is known as Fraunhofer condition, the parameter

$$N_F = \frac{b^2}{\lambda z} \tag{2.31}$$

is named Fresnel number [69]. Thus the Fresnel integral can be further simplified to the Fraunhofer integral [40, 70]

$$\begin{aligned}
\Gamma_0(x,y,z) &= \frac{i}{\lambda z} \exp\left\{-i\frac{\pi}{\lambda z}\left[x^2+y^2\right]\right\} \\
&\quad \times \int_{-\infty}^{\infty}\int_{-\infty}^{\infty} A(\xi,\eta) \exp\left\{i2\pi\left[\xi x/(\lambda z) + \eta y/(\lambda z)\right]\right\} d\xi d\eta \qquad (2.32) \\
&= \frac{i}{\lambda z} \exp\left\{-i\frac{\pi}{\lambda z}\left[x^2+y^2\right]\right\} \\
&\quad \times \int_{-\infty}^{\infty}\int_{-\infty}^{\infty} A(\xi,\eta) \exp\left\{i2\pi\left[\xi \nu_x + \eta \nu_y\right]\right\} d\xi d\eta \\
&= \frac{i}{\lambda z} \exp\left\{-i\frac{\pi}{\lambda z}\left[x^2+y^2\right]\right\} \mathcal{A}(\nu_x,\nu_y). \qquad (2.33)
\end{aligned}$$

Here,

$$\begin{aligned} \nu_\mathrm{x} &= \frac{x}{\lambda z} \approx \frac{\theta_\mathrm{x}}{\lambda} \qquad \text{and} \\ \nu_\mathrm{y} &= \frac{y}{\lambda z} \approx \frac{\theta_\mathrm{y}}{\lambda} \end{aligned} \tag{2.34}$$

denote spatial frequencies, and $\mathcal{A}(\nu_\mathrm{x}, \nu_\mathrm{y})$ is the two-dimensional Fourier transform of $A(\xi, \eta)$. This means, that the complex amplitude in the observation plane is a Fourier transform of the complex amplitude in the aperture plane, multiplied by a spherical phase factor.

According to Fourier optics, any arbitrary wave with complex amplitude $A(\xi, \eta)$ in free space can be analyzed as a superposition of plane waves [69]. The Fraunhofer integral can now be interpreted such, that only one of these plane waves in the aperture plane contributes to the complex amplitude at each point (x, y) in the observation plane. As can be identified in equation (2.32), this plane wave has the wavevector components $k_\mathrm{x} \approx 2\pi x/(\lambda z)$ and $k_\mathrm{y} \approx 2\pi y/(\lambda z)$ and travels at angles $\theta_\mathrm{x} \approx x/z$, $\theta_\mathrm{y} \approx y/z$, as sketched in figure 2.3. Due to destructive interference, all other waves cancel out.

Under the condition

$$z \gg \frac{a^2}{\lambda} > \frac{x^2 + y^2}{\lambda}, \tag{2.35}$$

that is for points in the observation plane close to the optical axis, the exponential term in equation (2.33) is also close to unity. With equation (2.27), the Fraunhofer integral for the complex amplitude $\Gamma(x, y, z)$ can be written as [69]

$$\begin{aligned} \Gamma(x, y, z) &= \Gamma_0(x, y, z) \exp\left\{-i\frac{2\pi}{\lambda} z\right\} \\ &= \frac{i}{\lambda z} \exp\left\{-i\frac{2\pi}{\lambda} z\right\} \mathcal{A}(\nu_\mathrm{x}, \nu_\mathrm{y}). \end{aligned} \tag{2.36}$$

Instead of placing the observation plane at infinity, one can introduce a lens with focal length f at a distance L behind the aperture plane [68, 73]. Now, the plane wave arriving at small angles θ_x and θ_y is focused into a point in the focal plane at $(x, y) = (\theta_\mathrm{x} f, \theta_\mathrm{y} f)$ (compare figure 2.4). If furthermore $L = f$, equation (2.36) changes to

$$\Gamma(x, y, z) = \frac{i}{\lambda f} \exp\left\{-\frac{2\pi i}{\lambda} 2f\right\} \mathcal{A}\left(\frac{x}{\lambda f}, \frac{y}{\lambda f}\right). \tag{2.37}$$

This means, that the image in the focal plane of a lens corresponds to the Fourier transform of the complex amplitude in the aperture plane [69].

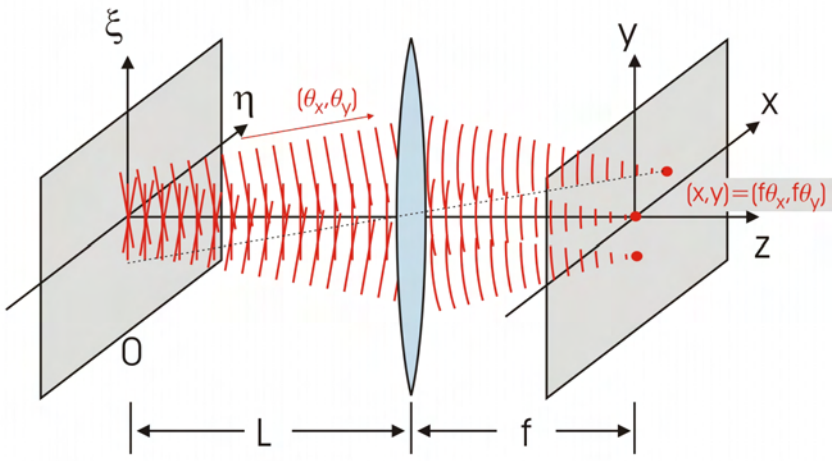

Figure 2.4: Fourier transformation in the focal plane of a lens
The plane wave arriving the lens at small angles θ_x and θ_y is focused into a point in the focal plane at $(x, y) = (\theta_x f, \theta_y f)$. After [69].

2.2 Examples for diffraction pattern

With the formulas derived above, the complex amplitude of a plane wave diffracted from different apertures can be calculated.

2.2.1 Pinhole

The complex amplitude in the plane of an infinitesimal small pinhole at coordinates (a, b) can be expressed as a Dirac delta function

$$A(\xi,\eta) = \delta(\xi - a, \eta - b) \qquad \text{with} \qquad \delta(\tau - t) = \begin{cases} 0 & \text{for} \quad \tau \neq t \\ \infty & \text{for} \quad \tau = t \end{cases} \tag{2.38}$$

According to the Fresnel-Kirchhoff formula [41], equation (2.24), the complex amplitude of the diffracted wave $\Gamma(x, y, z)$ can be calculated as

$$\begin{aligned} \Gamma(x,y,z) &= \frac{i}{\lambda} \int_{-\infty}^{\infty}\int_{-\infty}^{\infty} \delta(\xi - a, \eta - b) \frac{\exp\left\{-i\frac{2\pi}{\lambda}\sqrt{(x-\xi)^2 + (y-\eta)^2 + z^2}\right\}}{\sqrt{(x-\xi)^2 + (y-\eta)^2 + z^2}} d\xi d\eta \\ &= \frac{i}{\lambda} \frac{\exp\left\{-i\frac{2\pi}{\lambda}\sqrt{(x-a)^2 + (y-b)^2 + z^2}\right\}}{\sqrt{(x-a)^2 + (y-b)^2 + z^2}} \\ &= \frac{i}{\lambda r} \exp\left\{-i\frac{2\pi}{\lambda} r\right\} \\ &\text{with} \qquad r = \sqrt{(x-a)^2 + (y-b)^2 + z^2}. \end{aligned} \tag{2.39}$$

This is a spherical wave originating from the pinhole. Hence, a spherical wavefront can be generated by illuminating a pinhole with a plane wave. In this case, the Fresnel-Kirchhoff integral could be solved without approximations, therefore the solution is valid in the near field as well as in the far field. For points in the far field close to the optical axes, both Fraunhofer conditions (equations (2.30) and (2.35)) are satisfied and the approximations equation (2.26) and equation (2.28) are valid. So the spherical wave, equation (2.39), can be written as

$$\Gamma(x,y,z) = \frac{i}{\lambda z} \exp\left\{-i\frac{2\pi}{\lambda}z\right\}. \tag{2.40}$$

The amplitude $i/(\lambda z)$ varies slowly with z, so the wavefronts eventually approach a plane wave [69]. This fact also means that a plane wavefront can be generated by any arbitrary source if the observation plane is sufficiently far away.

2.2.2 Rectangular slit

When a plane wave of unit amplitude illuminates a rectangular slit of width a and height b centered at the origin, the complex amplitude in the aperture plane is

$$A(\xi,\eta) = \begin{cases} 1 & \text{for} \quad -\frac{a}{2} < \xi < \frac{a}{2} \quad \text{and} \quad -\frac{b}{2} < \eta < \frac{b}{2} \\ 0 & \text{else} \end{cases} \tag{2.41}$$

For the complex amplitude in the far field ($z \gg \frac{\xi^2+\eta^2}{\lambda}$, equation (2.30), and $z \gg \frac{x^2+y^2}{\lambda}$, equation (2.35)) follows with the Fraunhofer integral (equation (2.32) and (2.36)) [40, 69, 70]

$$\begin{aligned}
\Gamma_0(x,y,z) &= \frac{i}{\lambda z}\int_{-\infty}^{\infty}\int_{-\infty}^{\infty} A(\xi,\eta)\exp\left\{i2\pi\left[\xi x/(\lambda z)+\eta y/(\lambda z)\right]\right\}d\xi d\eta \\
&= \frac{i}{\lambda z}\int_{-a/2}^{a/2}\int_{-b/2}^{b/2} \exp\left\{i2\pi\xi x/(\lambda z)\right\}\exp\left\{i2\pi\eta y/(\lambda z)\right\}d\xi d\eta \\
&= \frac{i}{\lambda z}\left(i2\pi x/(\lambda z)\right)^{-1}\left[\exp\left\{i\pi a x/(\lambda z)\right\}-\exp\left\{-i\pi a x/(\lambda z)\right\}\right] \\
&\quad \times\left(i2\pi y/(\lambda z)\right)^{-1}\left[\exp\left\{i\pi b y/(\lambda z)\right\}-\exp\left\{-i\pi b y/(\lambda z)\right\}\right] \\
&= \frac{iab}{\lambda z}\left(\pi a x/(\lambda z)\right)^{-1}\sin\left(\pi a x/(\lambda z)\right) \\
&\quad \times\left(\pi b y/(\lambda z)\right)^{-1}\sin\left(\pi b y/(\lambda z)\right) \\
\Gamma_0(x,y,z) &= \frac{iab}{\lambda z}\operatorname{sinc}\left(a/\lambda\,\sin\theta_{\mathrm{x}}\right)\operatorname{sinc}\left(b/\lambda\,\sin\theta_{\mathrm{y}}\right),
\end{aligned} \tag{2.42}$$

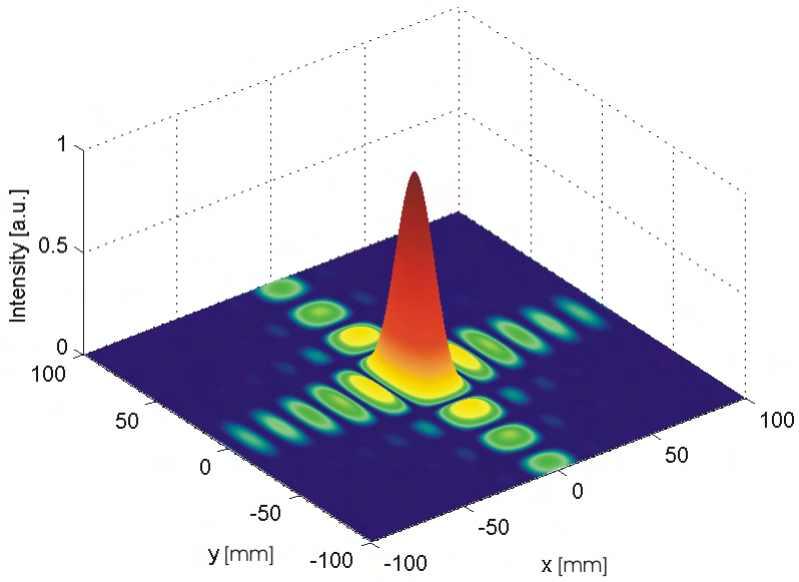

Figure 2.5: Intensity pattern behind a rectangular aperture
A slit with width $a = 500$ nm and height $b = 300$ nm is illuminated with a plane wave of wavelength $\lambda = 5$ nm, the diffraction pattern is viewed in a distance $z = 800$ mm.

with $\theta_x = x/z$, $\theta_y = y/z$, and $\mathrm{sinc}(x) = \sin(\pi x)/(\pi x)$. The intensity distribution in a plane at a distance z is then given by

$$\begin{aligned} I(x,y,z) &= |\Gamma(x,y,z)|^2 \\ &= I_0 \left[\frac{\sin\left(\frac{\pi a}{\lambda}\sin\theta_x\right)}{\left(\frac{\pi a}{\lambda}\sin\theta_x\right)}\right]^2 \left[\frac{\sin\left(\frac{\pi b}{\lambda}\sin\theta_y\right)}{\left(\frac{\pi b}{\lambda}\sin\theta_y\right)}\right]^2 \\ I(x,y,z) &= I_0\,\mathrm{sinc}^2\left(\frac{a}{\lambda}\sin\theta_x\right)\,\mathrm{sinc}^2\left(\frac{b}{\lambda}\sin\theta_y\right), \end{aligned} \tag{2.43}$$

where $I_0 = (ab/(\lambda z))^2$ is the peak intensity [69]. This intensity distribution creates an equidistant grid pattern with rapidly decreasing intensity aside the axes, as displayed in figure 2.5.

2.2.3 Circular aperture

As last example and with relevance for holography with soft X-rays (chapter 4 and chapter 5), a circular aperture of diameter a is considered. Illumination with

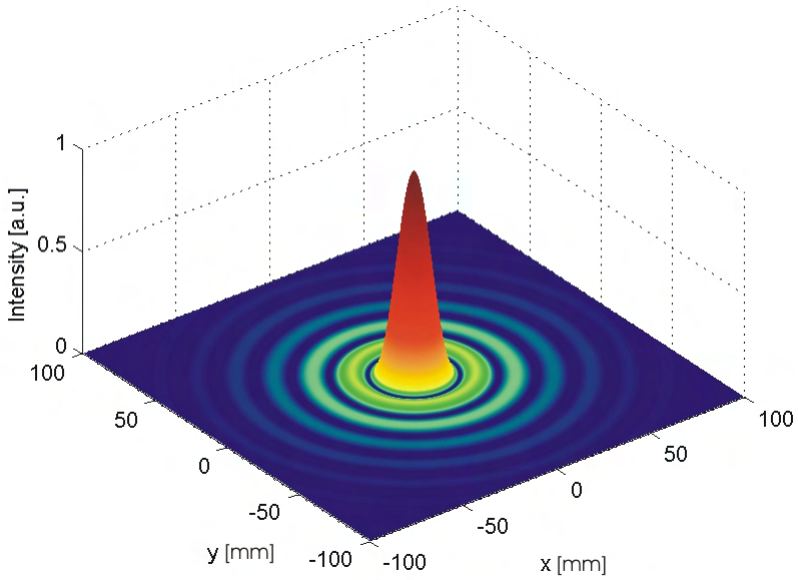

Figure 2.6: Intensity pattern behind a circular aperture
A circular aperture with diameter $a = 500$ nm is illuminated with a plane wave of wavelength $\lambda = 5$ nm, the diffraction pattern is viewed in a distance $z = 800$ mm. The colormap is the same as in figure 2.5.

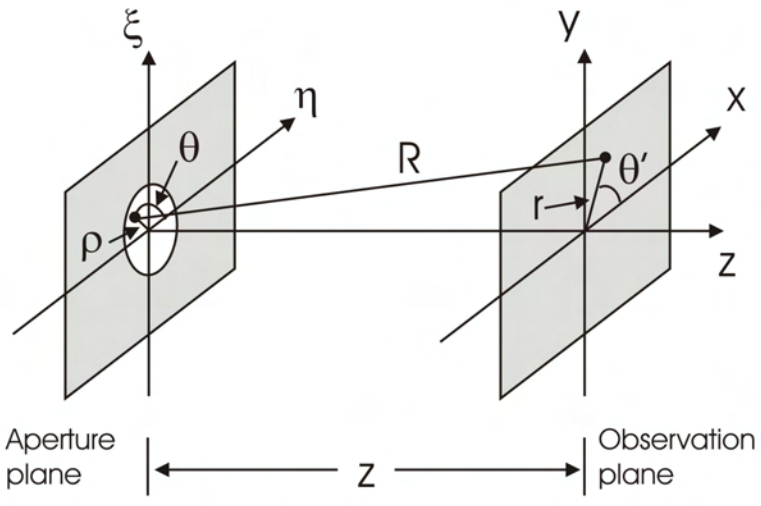

Figure 2.7: Coordinate system for the Fresnel-Kirchhoff integral

a plane wave results in a complex amplitude in the aperture plane as

$$A(\xi,\eta) = \begin{cases} 1 & \text{for} \quad \rho = \sqrt{\xi^2+\eta^2} < \frac{a}{2} \\ 0 & \text{else} \end{cases} \tag{2.44}$$

The underlying coordinate system is depicted in figure 2.7. Again, the resulting intensity pattern is regarded in the far field, so both Fraunhofer conditions ($z \gg \frac{(a/2)^2}{\lambda} > \frac{\xi^2+\eta^2}{\lambda}$, equation (2.30), and $z \gg \frac{x^2+y^2}{\lambda}$, equation (2.35)) are satisfied. Since it is a problem of circular symmetry, polar coordinates are used to simplify the equations. It is

$$\begin{aligned} R &= \sqrt{(x-\xi)^2+(y-\eta)^2+z^2} \\ \rho &= \sqrt{\xi^2+\eta^2} \qquad r = \sqrt{x^2+y^2} \\ \xi &= \rho\cos\theta \qquad x = r\cos\theta' \\ \eta &= \rho\sin\theta \qquad y = r\sin\theta' \end{aligned}$$

The Fraunhofer integral can then be written as

$$\begin{aligned} \Gamma_0(x,y,z) &= \frac{i}{\lambda z}\int_0^{2\pi}\int_0^{\infty} A(\rho,\theta)\exp\left\{\frac{i2\pi}{\lambda z}\rho r\left[\cos\theta\cos\theta' + \sin\theta\sin\theta'\right]\right\}\rho\, d\rho\, d\theta \\ &= \frac{i}{\lambda z}\int_0^{2\pi}\int_0^{a/2} \exp\left\{\frac{i2\pi}{\lambda z}\rho r\left[\cos\theta\cos\theta' + \sin\theta\sin\theta'\right]\right\}\rho\, d\rho\, d\theta \end{aligned} \tag{2.45}$$

With the sum and difference formulas it is [74]

$$\cos\theta\cos\theta' + \sin\theta\sin\theta' = \cos(\theta-\theta'), \tag{2.46}$$

and it follows for equation (2.45)

$$\Gamma_0(x,y,z) = \frac{i}{\lambda z}\int_0^{a/2}\int_0^{2\pi} \exp\left\{\frac{i2\pi}{\lambda z}\rho r\left[\cos(\theta-\theta')\right]\right\} d\theta\,\rho\, d\rho. \tag{2.47}$$

Due to the radial symmetry of the problem, the integral cannot depend on θ', therefore one can set $\theta' = 0$ [66]. The inner integral is of the form [68, 75]

$$\frac{1}{2\pi}\int_0^{2\pi}\exp\left\{i(x\cos\theta - n\theta)\right\} d\theta = J_n(x), \tag{2.48}$$

where $J_n(x)$ is a Bessel function of the first kind of order n. Bessel functions are solution for the differential equation

$$x^2\frac{d^2y}{dx^2} + x\frac{dy}{dx} + (x^2-n^2)y = 0 \tag{2.49}$$

and can be written as

$$J_n(x) = \sum_{\nu=0}^{\infty} \frac{(-1)^\nu}{\nu!\,\Gamma(n+\nu+1)} \left(\frac{x}{2}\right)^{n+2\nu}, \tag{2.50}$$

where $\Gamma(x)$ is the gamma function [74]. It is also [74, 75]

$$x^n J_n(x) = \int x^n J_{n-1}(x)\, dx. \tag{2.51}$$

Hence, equation (2.47) yields

$$\begin{aligned}
\Gamma_0(x,y,z) &= \frac{i}{\lambda z} \int_0^{a/2} 2\pi J_0\left(\frac{2\pi}{\lambda z}\rho r\right) \rho\, d\rho \\
&= \frac{i}{r} \int_0^{a/2} \frac{2\pi r}{\lambda z}\rho\, J_0\left(\frac{2\pi r}{\lambda z}\rho\right)\, d\rho \\
&= \frac{i}{r}\frac{\lambda z}{2\pi r} \int_0^{a/2} \frac{2\pi r}{\lambda z}\rho\, J_0\left(\frac{2\pi r}{\lambda z}\rho\right) \frac{2\pi r}{\lambda z}\, d\rho.
\end{aligned} \tag{2.52}$$

With the substitution $\alpha(\rho) = 2\pi r\rho/(\lambda z)$ and equation (2.51) it follows

$$\begin{aligned}
\Gamma_0(x,y,z) &= \frac{i}{r}\frac{\lambda z}{2\pi r} \int_{\alpha(0)}^{\alpha(a/2)} \alpha\, J_0(\alpha)\, d\alpha \\
&= \frac{i}{r}\frac{\lambda z}{2\pi r} \left[\alpha\, J_1(\alpha)\right]_0^{\pi r a/(\lambda z)}.
\end{aligned} \tag{2.53}$$

It is $J_1(0) = 0$ and $\lim(J_1(x)/x) = 1/2$ for $x \to 0$ [75], therefore

$$\begin{aligned}
\Gamma_0(x,y,z) &= \frac{i}{r}\frac{\lambda z}{2\pi r}\frac{\pi r a}{\lambda z} J_1\left(\frac{\pi r a}{\lambda z}\right) \\
&= i\frac{\lambda z}{\pi r a}\frac{2\pi(a/2)^2}{\lambda z} J_1\left(\frac{\pi r a}{\lambda z}\right) \\
\Gamma_0(x,y,z) &= i\frac{\pi(a/2)^2}{\lambda z}\frac{2\, J_1(\pi r a/(\lambda z))}{(\pi r a/(\lambda z))}.
\end{aligned} \tag{2.54}$$

For the intensity distribution in a plane at a distance z then follows

$$\begin{aligned}
I(x,y,z) &= \left|\Gamma(x,y,z)\right|^2 \\
&= \left|\frac{\pi(a/2)^2}{\lambda z}\frac{2\, J_1(\pi r a/(\lambda z))}{(\pi r a/(\lambda z))}\right|^2 \\
I(x,y,z) &= I_0 \left(\frac{2\, J_1(\pi r a/(\lambda z))}{(\pi r a/(\lambda z))}\right)^2,
\end{aligned} \tag{2.55}$$

with $I_0 = (\pi a^2/(4\lambda z))^2$ being the peak intensity. This pattern is known as Airy pattern, named after the English astronomer George Biddell Airy [66, 68]. It results in a bright central disc surrounded by rings with decreasing intensity, as displayed in figure 2.6. As it will be discussed later, this diffraction pattern limits the resolution of optical systems.

For smaller aperture diameters a, the Airy pattern gets broader, so for sufficiently small diameters, the Airy distribution converges to a spherical wave front.

2.3 Holographic principle

Images, such as photographs and paintings, are widely used to conserve moments. However, they are only two-dimensional projections of the three-dimensional world. Since conventional recording media only respond to the intensity of the light waves, all phase information is lost. But the phase contains information about the optical paths and hence the three-dimensional arrangement of the scene. If it is possible to reproduce the amplitude as well as the phase of a wavefront, the result cannot be distinguished from the original. A perfect illusion is created.

2.3.1 General principle of holography

As described above, it suffices to know the complex amplitude in one plane (formerly called the aperture plane) to determine the complex amplitude in any other plane in space (the observation plane). Considering a transparency, in which the complex amplitude of a wave in a certain plane is recorded, for example $A_0(x, y, 0)$. The transparency then has the complex amplitude transmittance $t(x, y) = A_0(x, y, z)$. Illuminated by a uniform plane wave with unit amplitude, the transmitted wave has a complex amplitude in this aperture plane of $A(x, y, z) = 1 \cdot t(x, y) = A_0(x, y, z)$. It propagates in space just like the original wave and cannot be distinguished from it. But how can such a transparency be created? And how can the phase of the complex amplitude be preserved?

The preservation of the phase can be done by mixing the original wave, that is the object wave A_{obj}, with a reference wave A_{ref}. If the waves are sufficiently coherent, the phase difference between object wave and reference wave is encoded in the intensity distribution of the resulting interference pattern (compare equation (2.13)). This intensity distribution can be recorded with a photographic plate, from which a transparency with an amplitude transmittance proportional to the intensity can be developed. With equation (2.13), the transmittance $t(x, y)$ is

then given by [41, 69, 70]

$$\begin{aligned} t(x,y) &\propto |A_{\mathrm{ref}} + A_{\mathrm{obj}}|^2 \\ &= A^*_{\mathrm{ref}}A_{\mathrm{ref}} + A^*_{\mathrm{obj}}A_{\mathrm{obj}} + A^*_{\mathrm{ref}}A_{\mathrm{obj}} + A^*_{\mathrm{obj}}A_{\mathrm{ref}} \\ &= I_{\mathrm{ref}} + I_{\mathrm{obj}} + 2\sqrt{I_{\mathrm{ref}}I_{\mathrm{obj}}}\cos(\varphi_{\mathrm{ref}} - \varphi_{\mathrm{obj}}). \end{aligned} \tag{2.56}$$

Illuminated by the reference wave A_{ref}, the complex amplitude of the wave behind the transparency is [40, 41, 69, 70]

$$\begin{aligned} A &= A_{\mathrm{ref}} \cdot t(x,y) \\ &\propto A_{\mathrm{ref}}\left(A^*_{\mathrm{ref}}A_{\mathrm{ref}} + A^*_{\mathrm{obj}}A_{\mathrm{obj}} + A^*_{\mathrm{ref}}A_{\mathrm{obj}} + A^*_{\mathrm{obj}}A_{\mathrm{ref}}\right) \\ &= A_{\mathrm{ref}}I_{\mathrm{ref}} + A_{\mathrm{ref}}I_{\mathrm{obj}} + I_{\mathrm{ref}}A_{\mathrm{obj}} + A^2_{\mathrm{ref}}A^*_{\mathrm{obj}}. \end{aligned} \tag{2.57}$$

The first two terms represent the reference wave modulated by the intensities I_{ref} and I_{obj}, and the third term contains the desired information about the object wave, while the last term contains the conjugate complex of the object wave. In this way, a method is found to preserve the whole complex amplitude of a wave in a two-dimensional image.

As already said before, the first person to develop this method was the Hungarian physicist Dennis Gabor [27] in 1947 while trying to improve electron microscopy. In figure 1.1, a schematic drawing of his setup is depicted. A diverging reference wave (primary wavefront) illuminates an object. Part of the wave is scattered by the object. This secondary wave interferes with the reference wave, and the interference pattern is recorded on a photographic plate. He called the transparency containing the interference pattern a hologram (from Greek: *holos = complete, graphein = to write*), and the method "microscopy by reconstructed wavefronts". Throughout the years, the term holography established. It should be emphasized, that holography is a two step process; first the hologram is created by interference of the object wave with a reference wave, then the object wave is reconstructed by diffraction of the reference wave from the interference fringes of the hologram.

Holography is usually performed with either plane reference waves or spherical reference waves. Different setup geometries are possible, too. Gabor himself used the so called in-line geometry. However, other geometries like the off-axis and the Fourier geometry were also developed. These three types will be introduced in the following.

2.3.2 In-line holography

When the object is placed on the optical axis that connects the source of the reference wave with the center of the recording screen, the arrangement is called

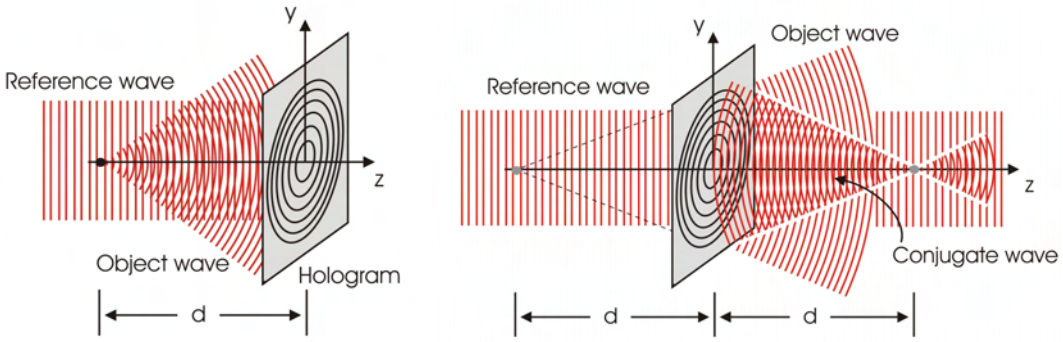

Figure 2.8: In-line holography setup
left: The object is placed on the optical axis that connects the source of the reference wave with the center of the recording screen. It is illuminated with a plane wave. The resulting interference pattern is recorded on a screen.
right: When the developed hologram is illuminated again with the reference wave, a virtual image of the object appears at the original position of the object. In the same distance on the other side of the hologram, a real image occurs, the twin-image. After [69].

in-line geometry. Usually, the screen is perpendicular to the optical axis. A schematic drawing of an in-line setup is depicted in figure 2.8, left. The object placed in a distance d to the screen is illuminated with a plane reference wave propagating in z-direction with complex amplitude

$$A_{\text{ref}}(z) = A_0 \exp\{-ikz\}. \tag{2.58}$$

The amplitude of the plane wave A_0 is a real constant with $I_0 = A_0^2$. The hologram is recorded on the screen. After removing the object, the developed hologram transparency is again illuminated with the same plane reference wave. With equation (2.57), the complex amplitude behind the hologram then is [69]

$$A \quad \propto \quad A_0 I_0 + A_0 I_{\text{obj}} + I_0 A_{\text{obj}} + I_0 A_{\text{obj}}^*. \tag{2.59}$$

The first two terms reflect the reference wave with altered amplitude. For obvious reasons, the first term is called source term. Since it results from interaction of the object wave with itself, the second term is the so called self-interference term. The last two terms contain the original object wave and its conjugate. Therefore, the third term is the hologram term, while the last one is named twin-image term [40, 70]. The reason for this denomination becomes clear in the following.

Looking through the illuminated hologram like looking through a window, the observer sees an illusion of the object as if it were still present at its original location. Perspective and depth of field are preserved. When changing the angle of view (within the dimension of the reference wave), the object can be viewed

from different sides. The observer also has to refocus his eyes when looking at parts of the object in a different distance. Since the image is created behind the hologram, and the object wave seems to diverge from it, it is a virtual image (compare figure 2.8, right) [40, 68, 70].

However, the image is disturbed by the remaining three terms in equation (2.59). Due to the source term, the bright transmission of the reference wave superimposes the image of the object. The self-interference term adds to this transmission. It can be neglected, if the amplitude of the object wave is much smaller than the one of the reference wave, $A_{0,\mathrm{obj}} \ll A_0$. This condition is satisfied, if the object is small and therewith permits a high transmission of the reference beam [40].

The last term, the twin-image term, represents a converging wave, forming a real image of the object at a distance d in front of the hologram. However, the phase is inverted with respect to the original object wave. This fact has the effect, that the parts of the object which were in the back now appear in the front. However, the parts, which were obscured by the parts in the front, still cannot be seen, since no wavefronts from there could reach the screen. When focusing on the virtual image of the object, the unfocused twin-image contributes to the coherent background [40].

An additional property of the hologram should be mentioned here. Every part of the hologram contains the whole information about the object. As the complete landscape can still be viewed when looking through a small opening in the window curtains, the whole object wave can be reconstructed from each part of the hologram, though maybe with limited resolution [66].

There are two ways to achieve a magnifying effect in in-line holography. If the hologram is reconstructed with a wavelength λ_{rec} different from the reference wavelength λ_{ref} used for the recording of the hologram, the image will be magnified by a factor [67]

$$M = \frac{\lambda_{\mathrm{rec}}}{\lambda_{\mathrm{ref}}}. \tag{2.60}$$

The second possibility is to use a spherical reference wave for recording and a plane wave with the same wavelength during the reconstruction of the hologram. If the distance of the point source to the recording screen is L, and the object is placed in a distance $d = L - l$ to the screen, the magnification is [41, 67, 70]

$$M = \frac{L}{L-d} = \frac{L}{l}. \tag{2.61}$$

With this approach, in-line holography can be used as a microscopy technique. The major drawback in in-line holography, however, is the superposition of the unfocused twin-image and the transmitted reference wave on the image. So it was until the 1960s, when E. N. Leith and J. Upatnieks developed a geometry to overcome this problem [42], that holography established as imaging method [40].

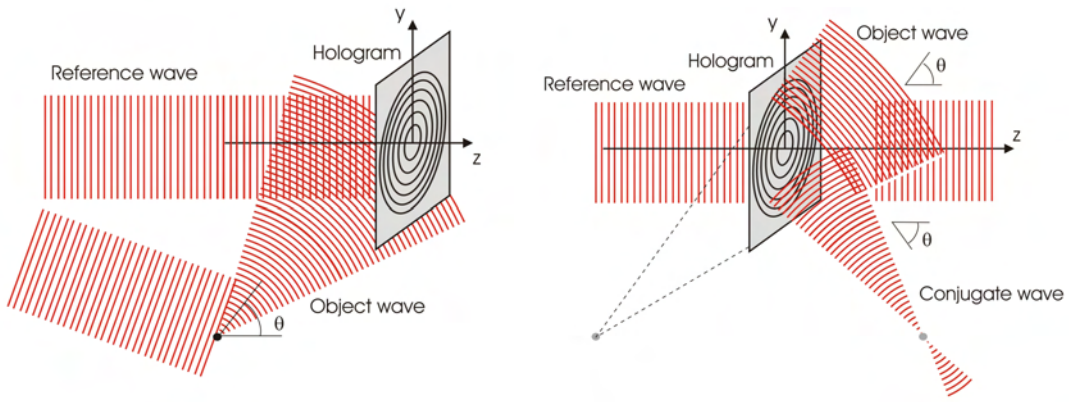

Figure 2.9: Off-axis holography setup
left: The plane reference wave is split, and part of it directly illuminates the recording screen. The other part impinges on the object, and the object wave travels at an angle θ with respect to the z-axis.
right: In the reconstruction, the different parts of the reconstructed wave are spatially separated. The wavefront of the object wave propagates in a direction including an angle θ with the z-axis, while the twin-image propagates in direction $-\theta$. After [69].

2.3.3 Off-axis holography

Leith and Upatnieks succeeded in spatially separating the four terms that occur in the reconstruction. Their idea was to introduce an angle between the direction of travel of the reference wave and of the object wave [42]. The plane reference wave is split, and part of it directly illuminates the recording screen, while the other part impinges on the object. The complex amplitude of the plane wave at the screen is

$$A_{\mathrm{ref}} = A_0, \tag{2.62}$$

with A_0 being a real constant. Assuming the object wave travels in the x-z-plane at an angle θ with respect to the z-axis, its complex amplitude can be written as

$$A_{\mathrm{obj}}(x,y) = a_{\mathrm{obj}}(x,y)\exp\{-ikx\sin\theta\}. \tag{2.63}$$

When the hologram is again illuminated by the reference wave, it follows with equation (2.57) for the complex amplitude at the transparency [69]

$$\begin{aligned} A(x,y) \quad \propto \quad & A_0\, I_0 + A_0\, |a_{\mathrm{obj}}(x,y)|^2 \\ & + I_0\, a_{\mathrm{obj}}(x,y)\exp\{-ikx\sin\theta\} \\ & + I_0\, a^*_{\mathrm{obj}}(x,y)\exp\{+ikx\sin\theta\}. \end{aligned} \tag{2.64}$$

Again, the first term is the source term, a plane wave traveling in z-direction, and the third term is the reproduced object wave. The last term contains the phase-inverted image of the object. This wavefront propagates in a direction including

an angle $-\theta$ with the z-axis. If the angle θ is chosen large enough, these three parts are now well-separated [69].

The second term can be neglected, if the object is small enough. If this is not the case, this term produces a halo surrounding the reference wave with approximately twice the angular spread θ_s of the object. So the angle θ has to be large enough to ensure the separation of the waves, what is satisfied for $\theta > 3\theta_\mathrm{s}$ [69].

With respect to the in-line holography setup, the off-axis geometry imposes higher demands concerning the coherence of the reference wave. But with the invention of the laser, sufficiently coherent light sources were available, and nowadays holographic recordings are routinely taken in the off-axis geometry.

Both methods presented above share the same problem. The spacing of the interference fringes decreases with increasing distance from the center of the screen. This can be best understood in the example of a point scatterer as object. The interference pattern of the spherical object wave with the plane reference wave then results in a pattern of concentric fringes. The radius of the nth bright ring is given by

$$r_\mathrm{n} = \sqrt{nd\lambda}, \tag{2.65}$$

where d denotes the distance of the point scatterer from the screen. This equation also describes the radii of the zones in a Fresnel zone plate [69, 70]. So the hologram of a point scatterer illuminated with a plane reference wave corresponds to a Fresnel zone plate. As obvious in the equation, the distance between two rings is

$$\Delta r(n) = \sqrt{d\lambda}\left(\sqrt{n} - \sqrt{n-1}\right). \tag{2.66}$$

Any recording medium, however, has a lower limit, down to which it can resolve structures. So this size poses an inherent resolution limit. A solution for this problem is Fourier holography, since it records the interference pattern of the respective Fourier transforms and not of the object and reference waves.

2.3.4 Fourier holography

As was introduced in section 2.1.5 in the first part of this chapter, the image of a wave with complex amplitude $A(x, y)$ at the other focal plane of a lens corresponds to its Fourier transform $\mathcal{A}\left(\frac{x}{\lambda f}, \frac{y}{\lambda f}\right)$, where f is the focal length of the lens, and λ is the wavelength. In general, the Fourier transform is a complex-valued function, so it cannot be recorded directly. But it can be recorded holographically [69].

A sufficiently transparent and flat object is placed in the front focal plane of a lens. It is then illuminated with a plane wave, resulting in an object wave $A(x, y)$ with Fourier transform $\mathcal{A}(\eta, \xi)$. A small pinhole in the same plane at a distance $-b$ to the object produces the reference wave. The complex amplitude of this

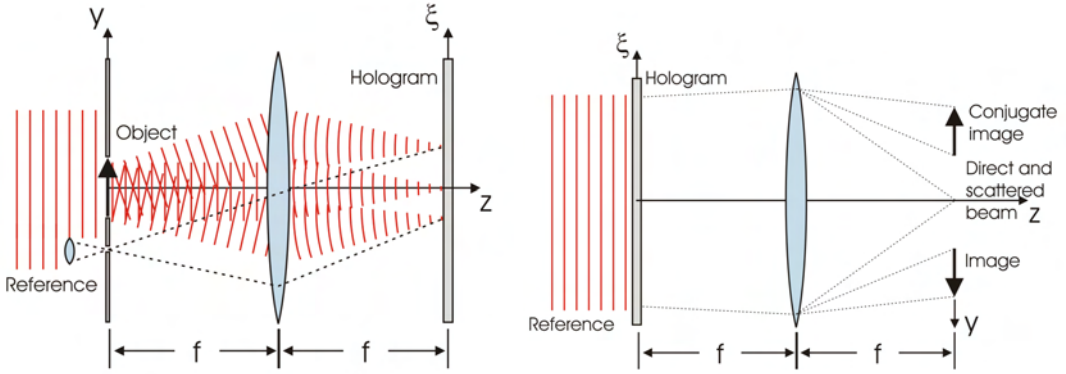

Figure 2.10: Fourier holography setup
left: The Fourier transform of the object wave interferes with the Fourier of a point source at the recording screen forming the hologram.
right: The developed hologram is illuminated by a plane wave. The inverse Fourier transform carried out by the lens reproduces the image and the conjugate image, both in the back focal plane, at a distance b and $-b$,respectively, to the optical axis. After [40].

wave is a delta function $A_{\text{ref}} = \delta(x+b, y)$, the Fourier transform of which can be calculated to be [40]

$$\mathcal{A}_{\text{ref}}(\eta, \xi) = \exp\{-i2\pi\xi b\}\,. \tag{2.67}$$

Hence the intensity pattern at the screen due to the interference of these waves is given by [40]

$$I(\eta, \xi) = 1 + |\mathcal{A}(\eta, \xi)|^2 + \mathcal{A}(\eta, \xi)\exp\{i2\pi\xi b\} + \mathcal{A}^*(\eta, \xi)\exp\{-i2\pi\xi b\}\,. \tag{2.68}$$

The developed hologram is then placed in the front focal plane of the same lens and illuminated by a plane wave of unit amplitude. At the back focal plane the Fourier transform of $I(\xi, \eta)$ is reproduced, that is displaying an intensity distribution [40]

$$\mathcal{I}(x, y) = \delta(x, y) + A(x, y) \star A(x, y) + A(x, y-b) + A^*(-x, -y+b). \tag{2.69}$$

Here, the symbol $\star$ denotes the correlation operation, which is defined as [40]

$$\begin{aligned} c(x, y) &= \int_{-\infty}^{\infty}\int_{-\infty}^{\infty} g^*(u, v)h(x+u, y+v)du\,dv \\ &= g(x, y) \star h(x, y), \end{aligned}$$

and which defines the autocorrelation of a function $g(x, y)$ as

$$c(x, y) = g(x, y) \star g(x, y). \tag{2.70}$$

The first term in equation (2.69) is the focused reference wave, the second term forms a halo around it. The image of the object is produced by the third term, now at a distance $-b$ to the optical axis, and the conjugate image formed at a distance b to the axis. The conjugate image is rotated by 180° with respect to the image. As in the off-axis geometry, both images are spatially separated from each other and from the reference beam. In contrast to the other geometries, both images are virtual images in Fourier holography [40].

A lensless Fourier holography setup is possible, too. In this case, the lens between object and recording screen is removed, the rest of the setup stays unaltered. The difference in the reconstruction is, that instead of a plane wave a spherical wave with the same average curvature as the reference wave is used to illuminate the hologram [40].

In the last 40 years, various applications of holography such as holographic interferometry have been developed [40, 41, 66]. A description of only parts of them would go beyond the scope of this thesis.

2.4 The holographic setup

For all holographic geometries, the basic setup consist of three major components:

- a source of coherent radiation,
- the sample,
- a recording screen.

The arrangement of these parts then determines the geometry. All three geometries presented above are performed in transmission with an adequate sample. This sample has to be sufficiently transparent, in order to permit the major part of the illuminating wave to pass undisturbed and form the reference wave. As a secondary effect, the self-interference term can be neglected, if the amplitude of the object wave is much smaller than the amplitude of the reference wave, $A_{0,\mathrm{obj}} \ll A_0$. On the other hand, $A_{0,\mathrm{obj}}$ must be large enough to assure a sufficient visibility of the interference fringes. According to equation (2.16), the visibility is given by

$$V = \frac{2\sqrt{I_1 I_2}}{I_1 + I_2} = \frac{2\sqrt{A_{0,\mathrm{obj}} A_0}}{A_{0,\mathrm{obj}}^2 + A_0^2}. \tag{2.71}$$

In practice, a ratio $A_{0,\mathrm{obj}} : A_0$ of 1 : 3 to 1 : 5 was found to be a good value. Therefore, small opaque samples on a transparent backing can be holographically recorded, but not vice versa.

In off-axis holography a reflection setup is also possible, where the part of the object wave reflected from the sample can be brought to interference with the

reference wave. In this way, images of the surface of opaque samples can be recorded.

Holography can be performed with any type of coherent radiation. The only requirement is, that the coherence length L (see equation (2.18)) exceeds the largest path differences occurring between object wave and reference wave [47]. Gabor himself did his first experiments with electrons. Today, electron holography is a well-established technique in transmission electron microscopy [70]. With the invention of the laser in 1960, light sources with long coherence lengths were available. This development paved the way for off-axis holography. In this setup the path differences are larger than for in-line holography, so the requirements concerning the coherence of the radiation increase. Today, laser wavelengths ranging from the infrared down to X-rays can be generated [48].

Another source for coherent X-rays is synchrotron radiation [47]. First generated as a byproduct of electron storage rings, this kind of radiation is now widely used—not only in holography—since it is highly brilliant, monochromatic, polarized, and the photon energy can be varied over a wide range. The generation and the properties of synchrotron radiation are described in the following chapter.

As discussed in equation (2.40), any wave will approach a plane wavefront if the propagation distance is sufficiently large. In order to generate a spherical wavefront, two possibilities exist. Firstly, the diffraction of a plane wave from a pinhole results in a spherical wave, as derived in equation (2.39). For finite pinhole diameters, the emission cone decreases and the intensity distribution is described by the Airy distribution (equation (2.55)), but the wavefront is still a good approximation of a spherical wave if the pinhole is small enough. However, for decreasing wavelength it gets more and more difficult to provide pinholes of appropriate diameter. The second alternative is to use a lens with a short focal length to focus a wavefront. Behind the focus, the wavefront diverges and forms a quasi-spherical wavefront. The shorter the focal length, the larger is the divergence. But also in this method, with decreasing wavelength, it becomes increasingly difficult to fabricate appropriate lenses. For X-rays, diffractive optics like Fresnel zone plates have to be used, since refractive effects are too small.

Concerning the recording screen, the material has to fulfill two major requirements. First, it has to respond linearly to the intensity of the radiation, and second, its spatial resolution has to be high enough to resolve the interference fringes. Photographic films, photoresist, and photopolymers are among the widely used materials [40]. With the rise of the computer, digital recording devices like CCD cameras have established. To satisfy the prerequisites for holography, the dynamic range of the CCD must be sufficient to ensure the linear intensity dependence, and the pixel size has to be small enough to resolve the interference fringes. Digital holography has the advantage, that the wavefronts do not have to be reconstructed optically, but the backpropagation of the object wave can

be calculated numerically from the digital hologram using the Fresnel-Kirchhoff formula, equation (2.24).

2.5 Numerical reconstruction of digital holograms

As derived previously, to optically reconstruct the image from a hologram, the hologram transparency with transmittance $t(\xi,\eta)$ (equation (2.56)) is illuminated with the reference wave A_{ref}. The complex amplitude behind the hologram is then given by $A(\xi,\eta) = A_{\mathrm{ref}}(\xi,\eta)\cdot t(\xi,\eta)$ (equation (2.57)), and the wavefront propagates as described by the Fresnel-Kirchhoff formula (equation (2.24)).

In digital holography, the complex amplitude of the wave is calculated from the digital hologram, and the propagation of the wave is computed numerically. The derivation of the wavefront in a specific plane is therefore called numerical reconstruction [76]. Each of this reconstructed planes corresponds to one in-focus image in conventional compound microscopy. A combination of various two-dimensional planes results in a three dimensional image of the object.

Numerical reconstruction has two major advantages compared to the optical method. Firstly, since it is the complex amplitude $\Gamma(x,y,z)$ which is computed, not only the intensity $I(x,y,z) = |\Gamma(x,y,z)|^2$ of the wave can be calculated, but also the phase $\varphi(x,y,z) = \arctan(\Im\{\Gamma(x,y,z)\}/\Re\{\Gamma(x,y,z)\})$ [41]. And secondly, it is possible to remove the reference wave from the reconstruction by subtracting its contribution I_{ref} from the hologram $t(\xi,\eta)$ [28]. The resulting intensity pattern $I(\xi,\eta)$ is then given by

$$I(\xi,\eta) = \frac{t(\xi,\eta) - I_{\mathrm{ref}}}{\sqrt{I_{\mathrm{ref}}}} = \frac{A^*_{\mathrm{obj}}A_{\mathrm{obj}} + A^*_{\mathrm{ref}}A_{\mathrm{obj}} + A^*_{\mathrm{obj}}A_{\mathrm{ref}}}{\sqrt{I_{\mathrm{ref}}}}. \tag{2.72}$$

In the following, this normalized intensity distribution shall be referred to as difference hologram.

The Fresnel-Kirchhoff integral can be solved in the Fresnel approximation (equations (2.26) and (2.28)) [41]. Then, the Fresnel integral (equation (2.29))

$$\begin{aligned}\Gamma_0(x,y,z) &= \frac{i}{\lambda z}\exp\left\{-i\frac{\pi}{\lambda z}\left[x^2+y^2\right]\right\} \\ &\quad\times\int_{-\infty}^{\infty}\int_{-\infty}^{\infty} A(\xi,\eta)\exp\left\{-i\frac{\pi}{\lambda z}\left[\xi^2+\eta^2\right]\right\} \\ &\quad\times\exp\left\{i2\pi\left[\xi x/(\lambda z)+\eta y/(\lambda z)\right]\right\}d\xi\,d\eta\end{aligned} \tag{2.73}$$

can be understood as an inverse Fourier transformation of the function

$$F(\xi,\eta) = A(\xi,\eta)\exp\left\{-i\frac{\pi}{\lambda z}\left[\xi^2+\eta^2\right]\right\}. \tag{2.74}$$

Fourier transformations can be efficiently computed with a Fast Fourier Transform (FFT) algorithm. But the approximation in the argument of the exponential function (equation (2.26)) might lead to artifacts [29]. The full implementation of the Fresnel-Kirchhoff integral however requires long computation time, due to the non-linearity in the phase factor. Therefore, Kreuzer developed an algorithm which removes this non-linearity, yielding a fast and accurate evaluation of the Fresnel-Kirchhoff integral without approximations [76]. Since the images presented in this thesis are reconstructed with an algorithm using the Kreuzer Implementation, its design will be described in the following.

For a spherical reference wave emerging from the origin, the Fresnel-Kirchhoff integral can then be written as [28, 77]

$$\Gamma(x,y,z) = \iint_S I(\vec{\xi}) \exp\left\{-\frac{i2\pi}{\lambda}\frac{\vec{\xi}\vec{r}}{\xi}\right\} d\vec{\xi}, \tag{2.75}$$

where $\vec{\xi} = (\xi, \eta, L)$ denotes the coordinates on the screen at distance L to the point source, $\vec{r} = (x, y, z)$ is the position vector to a point in the observation plane, λ is the wavelength, and $I(\vec{\xi})$ is the intensity pattern of the difference hologram (equation (2.72)). The integral extends over the surface S of the screen. Since it is derived from the integral theorem of Helmholtz and Kirchhoff, it is referred to as Kirchhoff-Helmholtz integral. In the derivation of the formula it is assumed, that the sample of dimension a is sufficiently far from the point source, such that the Fraunhofer condition $a^2 \ll l\lambda$ (equation (2.35)) is satisfied, and that the distance l from the point source to the sample is much smaller than the distance L to the screen. The phase factor in front of the integral can be neglected, since it only results in a constant factor when calculating the intensity.

Unlike a photographic plate, a CCD chip is not continuous but consists of discrete pixels. So the coordinates in the equation have to be expressed as a discrete grid. Usually [41, 76] this is done using

$$\begin{array}{rcccl} \xi & = & \xi_k & = & k\Delta\xi \\ \eta & = & \eta_l & = & l\Delta\eta \\ x & = & x_m & = & m\Delta x = m\frac{\lambda L}{N\Delta\xi} \\ y & = & y_n & = & n\Delta y = n\frac{\lambda L}{N\Delta\eta} \\ \multicolumn{5}{c}{\text{with} \quad k,l,m,n = 0,1,\ldots,N-1} \end{array} \tag{2.76}$$

where N is the number of pixels in one direction on the CCD chip. In order to remove the non-linearity in the phase factor, the coordinate system is transformed

as [76]

$$\begin{aligned} \xi' &= \xi\frac{L}{R} \\ \eta' &= \eta\frac{L}{R} \qquad (2.77) \\ R &= \sqrt{L^2+\xi^2+\eta^2} \end{aligned}$$

(2.78)

This transformation corresponds to a projection of the intensity pattern from a flat screen onto the surface of a sphere and gives a non-equidistant barrel shaped coordinate system. That means, the intensity values are now located at non-integer positions on a plane. Fast Fourier Transforms however work on equidistant grids, so the intensity values have to be interpolated onto an equidistant coordinate system. To avoid boundary effects which occur in Fourier transforms when sharp edges are present, a cosine filter is subsequently used to smooth the edges of the hologram. Up to now, no alterations to the Kichhoff-Helmholtz formula itself have been made, only the coordinate system has been changed [76]. In a last step, the integral (or sum, in the discretized notation) is rewritten as a convolution, which has the general form [69]

$$h(x,y) = (f * g)(x,y) = \int_{-\infty}^{\infty}\int_{-\infty}^{\infty} f(u,v)g(x-u,y-v)\,du\,dv. \qquad (2.79)$$

According to the convolution theorem, the Fourier transform of the convolution of two functions is equal to the product of the Fourier transform of the individual functions [41]

$$\begin{aligned} H(u,v) &= \mathcal{F}\{h(x,y)\} = \mathcal{F}\{(f*g)(x,y)\} \\ &= \mathcal{F}\{f(x,y)\}\cdot\mathcal{F}\{g(x,y)\} = F(u,v)G(u,v). \qquad (2.80) \end{aligned}$$

Since the Fourier integral theorem says, that any function can be written as the inverse Fourier transform of its Fourier transform, that is [41]

$$\mathcal{F}\mathcal{F}^{-1}\{h(x,y)\} = \mathcal{F}^{-1}\mathcal{F}\{h(x,y)\} = h(x,y), \qquad (2.81)$$

the complex amplitude can be expressed as [41]

$$\begin{aligned} \Gamma(x,y,z) &= \mathcal{F}^{-1}\mathcal{F}\{(\mathcal{I}*\mathcal{K})(x,y)\} \\ &= \mathcal{F}^{-1}\{\mathcal{F}\{\mathcal{I}\}\,\mathcal{F}\{\mathcal{K}\}\}. \qquad (2.82) \end{aligned}$$

Here, $\mathcal{I}$ is the intensity distribution of the hologram and $\mathcal{K}$ the convolution kernel, both expressed in the transformed coordinate system. Thus, the computation of the Kirchhoff-Helmholtz integral is broken down to three Fourier transforms.

The Fourier transform of the hologram has to be carried out only once per image since it does not depend on the coordinates of the reconstruction plane. With this implementation, a fast reconstruction of the wavefront at various distances from the detector is possible [76].

3 BESSY

Digital in-line holography experiments with synchrotron radiation have been carried out at the 3rd generation synchrotron source BESSY II in Berlin, Germany. In the course of this thesis, measurements have been performed on three beamtimes, each lasting one week, and the results have been analyzed. The generation of synchrotron radiation and the digital in-line X-ray holography setup at BESSY are introduced in this chapter.

3.1 Generation of synchrotron radiation

In nature, synchrotron radiation occurs when charged particles spiral around magnetic field lines in space, as the light coming from the Crab Nebula, for example. However, the generation of this kind of radiation in the laboratory is only 60 years old. From the discovery of X-rays in 1895 by Röntgen, it has taken half a century until the first synchrotron light could be observed at the General Electric Research Laboratory in Schenectady, New York, on April 24th, 1947. More details of the historical development of synchrotron radiation can be found in [78].

The generation of X-rays in classical X-ray tubes as depicted in figure 3.1 is based on the interaction of high energy electrons with the material of the anode[1]. Two different processes contribute. One process is the ionization of the anode atoms in inner shells. These holes are filled by electrons from higher shells, while the excess energy is emitted leading to the characteristic line spectrum [80]. The second process is the Coulomb interaction of the electrons with the nuclei of the anode material, by which the electrons are decelerated. Those decelerated electrons emit a continuous spectrum, the bremsstrahlung [80]. The emission is isotropic and the efficiency of the X-ray tube $\eta \approx 10^{-9} cZU$ is less than 1%, where c is a factor of dimension V^{-1}, Z is the atomic number, and U is the voltage accelerating the electrons. Most of the power is lost as heat[80, 81].

An important quantity for sources of radiation is their spectral brightness or brilliance B [70, 78]

$$B = \frac{N/t}{d\Omega dF(d\lambda/\lambda)}. \tag{3.1}$$

[1]Depending on the literature, the anode is sometimes called anticathode.

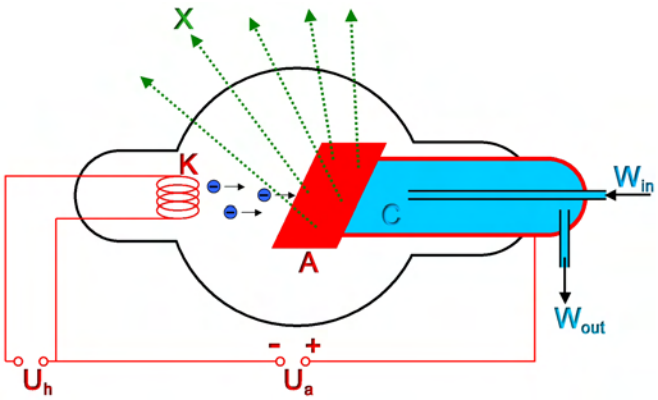

Figure 3.1: Schematic drawing a classical X-ray tube
A hot cathode K with a heating voltage U_h produces electrons which are accelerated onto the anode A by the voltage U_a. When decelerated by the anode material, they emit X-ray radiation X perpendicular to the direction of deceleration. To avoid heating of the material, the anode is water cooled (water inlet W_{in}, outlet W_{out}, cooling water volume C). From [79].

It is the number of photons N per time interval t and per source area dF emitted into the solid angle $d\Omega$ and related to the relative bandwidth $d\lambda/\lambda$.

While in a timespan of 70 years the peak brilliance of X-ray tubes could be improved from about 10^7 to 10^{12} (compare figure 3.2), which is more than the brilliance of a candle $(5 \cdot 10^4)$ or a light bulb $(5 \cdot 10^7)$, it is still less than that of the sun (10^{11}) [83] .

X-ray sources with a brilliance orders of magnitude higher than classical X-ray tubes are synchrotron sources. Similar to X-ray tubes, where the electrons emit X-rays during deceleration, they exploit the fact that any accelerated charged particle emits radiation. In order to maintain the acceleration a of the charge q the energy radiated per unit time dE/dt has to be compensated for. With ϵ_0 being the vacuum permittivity and c the speed of light, it is given by [84]

$$\frac{dE}{dt} = \frac{q^2 a^2}{6\pi\epsilon_0 c^3}. \tag{3.2}$$

For a particle with mass m, velocity v, and momentum p on a circular orbit with radius r, the centripetal acceleration is $a = v^2/r = p^2/m^2 r$ and therefore equation (3.2) can be written as [84]

$$\frac{dE}{dt} = \frac{q^2}{6\pi\epsilon_0 c^3 r^2}\left(\frac{p}{m}\right)^4. \tag{3.3}$$

That equation implies that the radiation increases with decreasing radius and increasing momentum, and a light particle emits more radiation than a heavy

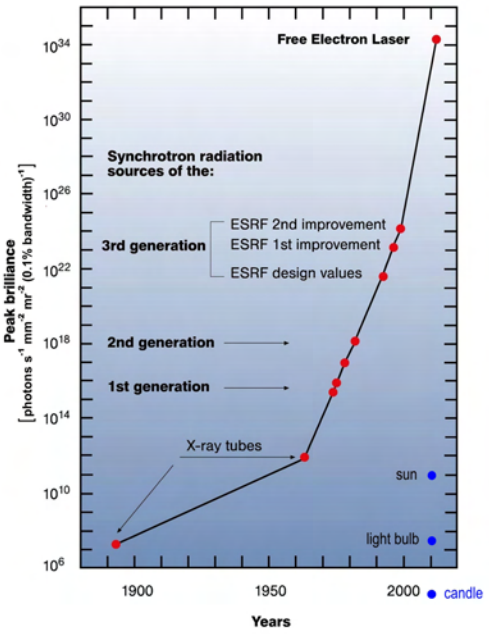

Figure 3.2: Brilliance of X-ray sources
The peak brilliance is approximately three orders of magnitude higher than the average brilliance.
From: [82]. Copyright: DESY, Hamburg

one. Therefore, electrons or positrons at high energies are used in storage rings to produce synchrotron radiation.

At the Berliner Elektronenspeicherring für Synchrotronstrahlung (BESSY II), electrons are extracted from a hot cathode and accelerated by a voltage of 100 kV, as sketched in figure 3.3. In a microtron, which the electrons pass ten times with rising orbit radius, a high frequency linear accelerator brings them to an energy of 50 MeV. Afterward, the electrons pass the synchrotron, where the magnetic field increases synchronously with the energy of the particles, until they reach their final energy of 1.7 GeV and are injected into the storage ring. The whole cycle—from electron extraction to injection—lasts 50 ms, and is repeated 10 times per second. Each of the 400 electron bunches in the ring contains about 10^{10} electrons and circulates with a frequency of 1.25 MHz. In the end, the total ring current amounts to 800 mA. The beam pipes themselves are evacuated to a pressure of $< 10^{-10}$ mbar to prevent the electrons from colliding with air molecules, leading to a lifetime[2] of the electron bunches of 8 to 10 hours.

The storage ring itself is not a perfect circle but consists of 16 units, each comprising of bending magnets to keep the bunches in orbit, quadrupole magnets for focusing, sextupole magnets as correcting elements, and a linear part, as depicted in figure 3.3, left. One of the sixteen linear parts contains the injection system. A second part houses the cavities needed for the compensation of the

[2]The lifetime is defined as the time interval, after which the number of particles has dropped to $1/e$ of the initial number, e being Euler's number [75].

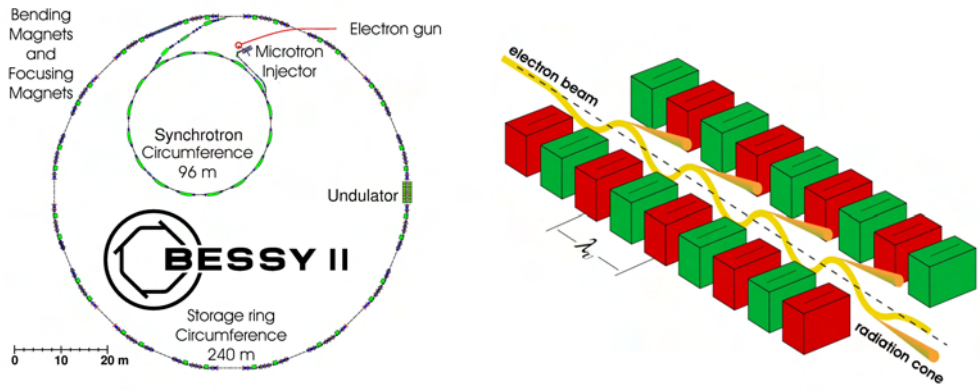

Figure 3.3: Schematic drawing of BESSY II and an undulator
left: Electrons are extracted from a hot cathode and are accelerated in several stages until they are injected in the storage ring. From [85].
right: Undulator principle. The electrons undergo sinusodial oscillation in the magnetic field and emit radiation. From [86].

energy loss, which is lost in the bending magnets due to synchrotron radiation. The radiated spectrum is continuous ranging from the long wave terahertz region ($\lambda = 100$ µm) to hard X-rays ($\lambda = 10$ pm), linearly polarized in the plane of the electron orbit, and circularly polarized below and above. Since the electrons are arranged in bunches, the radiation is pulsed with a pulse length of 18 ps and a pulse spacing of 2 ns [70, 85]. In addition, because of the high velocity of the electrons, the produced electromagnetic field reminds less of a point dipole field, but the radiation is concentrated in the general direction of motion [70, 80]. The divergence is $\Theta = m_0c^2/E = 0.3$ mrad for electrons ($m_0c^2 = 0.511$ MeV) at an energy of $E = 1.7$ GeV. The source area, which is the diameter of the electron bunches, is $dF \leq 0.1$ mm^2. With equation (3.1) this leads to a spectral brightness of $B \geq 10^{14}$ photons/(s mm^2 10^{-7} sr) at $d\lambda/\lambda = 0.1\%$ for photons in the keV range [70].

In equation (3.3), the radiated power dE/dt depends inversely on the square of the radius r of the electron orbit. A decrease in r thus leads to stronger synchrotron radiation. However, this power loss has to be compensated. As a consequence, the maximum energy of the electrons is limited and scales inversely to the square of the radius of the synchrotron ring. So smaller synchrotrons are not desirable. In order to create electron orbits with small curvature, magnetic devices are added in the remaining fourteen linear parts of the storage ring. In these structures, dipole magnets are linearly arranged with periodically alternating magnetic fields (see figure 3.3, right). When traveling through the magnetic field, the electrons are forced to undergo sinusoidal oscillations with small r. Hence they are accelerated and emit radiation.

The magnetic devices are called insertion device magnets, because they are placed

in the straight section of the storage ring between the bending magnets. Depending on the strength of their magnetic field, they are named wiggler or undulator. The dimensionless deflection parameter K characterizes the electron motion and determines whether the device is a wiggler ($K \gg 1$) or an undulator ($K \leq 1$). K depends on the electron charge e, the peak magnetic field B, the period length of the magnetic structure λ_U, the electron mass m_e, and the speed of light c [70, 86, 87]:

$$K = \alpha\gamma = \frac{eB\lambda_U}{2\pi m_e c} = 0.934\lambda_\mathrm{U}[\mathrm{cm}]B[\mathrm{T}]. \tag{3.4}$$

Here, α is the maximum deflection angle, and $\gamma = E/m_0c^2$.

Wigglers have stronger magnetic fields and deflect the electrons stronger from their straight paths than undulators. A wiggler consisting of n magnetic periods has a length $L = n\lambda_\mathrm{U}$, and imposes $2n$ turns on the electrons. The radiation from those turns adds incoherently, and the intensity of the generated synchrotron radiation is $2n$ times larger than that of a bending magnet. The radiated spectrum is broad, but shorter wavelengths are reached than in the bending magnets.

The magnetic field of undulators is weaker compared to that of wigglers ($K \leq 1$), thus the deflection of electrons is less and the different radiation lobes interfere coherently. As consequence, the spectrum becomes discrete, consisting of harmonics of the wavelength [70]

$$\lambda_\mathrm{i} = \frac{\lambda_U}{2i\gamma^2}\left(1 + \frac{K^2}{2} + \gamma^2\theta^2\right). \tag{3.5}$$

Here, i is the order of the harmonic (odd natural number), and θ is the angle to the forward direction in the plane of the electrons. For the first harmonic ($i = 1$) on the axis ($\theta = 0$), the wavelength generated by electrons with energy E is [87]

$$\lambda_1[\text{Å}] = \frac{13.056\lambda_U[\mathrm{cm}]}{E^2[\mathrm{GeV}]}\left(1 + \frac{K^2}{2}\right). \tag{3.6}$$

According to Planck's law, wavelength λ and energy E_photon of photons are related via

$$E_\mathrm{photon} = h\nu = h\frac{c}{\lambda}, \tag{3.7}$$

with h being Planck's constant and c the speed of light. Inserting the numbers leads to a conversion from a wavelength λ in nm to a photon energy E_photon in eV of

$$E_\mathrm{photon}[\mathrm{eV}] = \frac{1240}{\lambda\,[\mathrm{nm}]}. \tag{3.8}$$

Hence the photon energy corresponding to the wavelength λ_i is given by [87]

$$E_{\mathrm{photon},1}[\mathrm{keV}] = 0.950\frac{E^2[\mathrm{GeV}]}{\left(1 + \frac{K^2}{2}\right)\lambda_U[\mathrm{cm}]}. \tag{3.9}$$

The relative bandwidth at the ith harmonic is [87]

$$\frac{\Delta\lambda_\mathrm{i}}{\lambda_\mathrm{i}} \cong \frac{1}{i\,n}, \tag{3.10}$$

so the longitudinal coherence length L follows (compare equation (2.18)) [87]

$$L = \frac{\lambda_\mathrm{i}^2}{\Delta\lambda_\mathrm{i}} = i\,n\lambda_\mathrm{i}. \tag{3.11}$$

The photon intensity now scales with a factor n^2, since the emission angle is simultaneously reduced by $1/n$. Additionally, the spectral brilliance is three to four orders of magnitude higher than for bending magnets. The synchrotron radiation is linearly polarized in the plane of the orbit and circularly polarized above and below. By using permanent magnets in addition to the periodic magnetic structures in the undulators, the trajectories of the electrons can be altered to a helix, and the polarization in the plane of the orbit can be changed to circular or elliptical.

The synchrotron radiation originating from the bending magnets, wigglers, and undulators is guided in 46 beamlines to the different experimental stations. Our experiments were carried out at the beamline UE52-SGM, a schematic drawing of this beamline is shown in figure 3.4 [88]. Synchrotron radiation with the chosen energy and polarization generated in the undulator passes the cylindrical mirror M1, which deflects the beam horizontally and vertically demagnifies the source on the entrance slit. The plane mirror M2 deflects the beam onto the spherical deflection grating G, where it is monochromatized. The following cylindrical mirror M3 demagnifies vertically and images the exit slit on the focus spot, while the plane elliptical mirror M4 gives a horizontal demagnification of the source. By varying the width of the entrance slit, one can trim the synchrotron beam in its horizontal extent, and enhance the spatial coherence [87]. Full width at half maximum (FWHM) of the horizontal dimension of the focal spot is 17.4 µm, while the size of the exit slit determines the vertical size of the focal spot (compare figure 3.5). The divergence at the focus position is 6 mrad in horizontal direction and 1 mrad vertically.

Since the undulator consists of $n = 77$ poles [85], equation (3.11) gives a longitudinal coherence length of $L = 77\,i\lambda_\mathrm{i} = 77 \cdot 12.4\mathrm{nm} = 0.95$ µm for a photon energy $E = 100$ eV generated in the first harmonic. This value is not sufficient for holography since it is in the range of the occurring path differences . Behind the monochromator, the resolving power is $E/\Delta E = \lambda/\Delta\lambda = 30000$ at a photon energy $E = 100$ eV [88]. Thus it follows for the longitudinal coherence length

$$L = \frac{\lambda^2}{\lambda} = 30000 \cdot \frac{1240}{100}\mathrm{nm} = 372\,\mu\mathrm{m}. \tag{3.12}$$

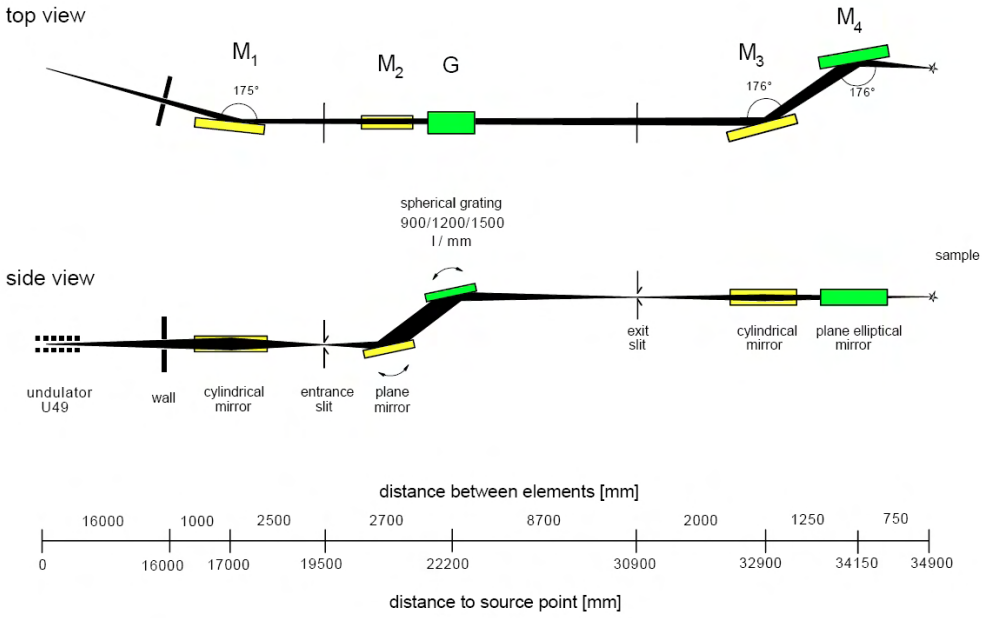

Figure 3.4: Schematic lay-out of the beamline UE52-SGM at BESSY II
Synchrotron radiation generated in the undulator is monochromatized by a spherical deflection grating and horizontally and vertically focused by mirrors. From [88].

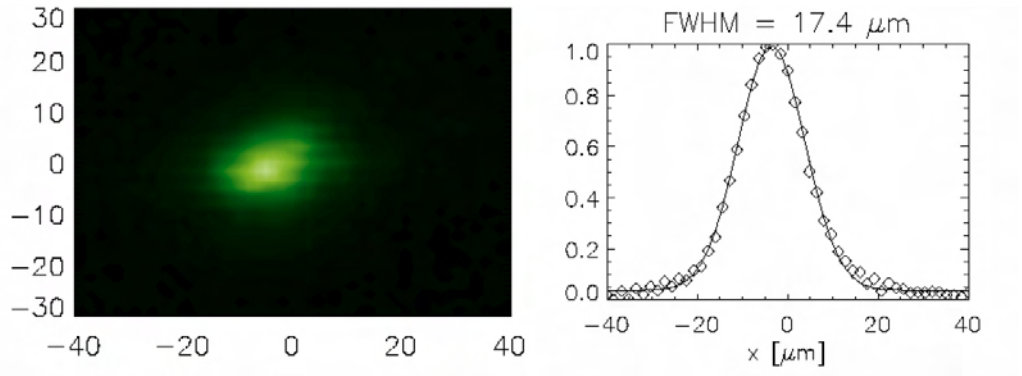

Figure 3.5: Focus spot of the beamline UE52-SGM at BESSY II
The spot size at the experiment is 17.4 µm x exit slit size (horizontally x vertically). From [88].

As discussed in chapter 2, equation (2.23), the spatial coherence distance a_k also depends on the size h of the source. At the synchrotron, the source size is given by the size of the electron bunches, which is 100 µm.

3.2 The digital in-line X-ray holography setup

The DIXH setup consists of a pinhole, the sample and a CCD camera as detector. Figure 3.6 is a photo of the setup taken by Florian Staier during the beamtime in February 2006. For our holography experiments, the ALICE scattering chamber of the group of Prof. Zabel, Ruhr-Universität Bochum, Germany, was used. The beamline coming from the storage ring is situated on the left. The pinhole is placed in the focus of the synchrotron beam so that as little intensity as possible is discarded by the small aperture. Nonetheless only about $2 \cdot 10^{-3}$ of the total flux passes the pinhole (400 nm diameter) [37]. To adjust the position of the pinhole, it is mounted on translation stages which enable movement in three directions with sub-micrometer precision. For the first experiments, the samples were glued onto the pinhole in a distance of approximately 10 mm. In later experiments, the samples were attached to separate manipulators which allow independent movement of pinhole and sample. Also, the sample can be retracted completely from the optical path, so that the diffraction pattern of the pinhole alone can be recorded. Recording of the scattering patterns is done by a CCD camera (Roper Scientific PI-SX-2048, back-illuminated Marconi CCD42-40 chip, 2048×2048 pixels, pixel size: 13.5×13.5 µm^2). For the given photon energy (90eV), the quantum efficiency of the CCD chip is about 45% [89]. A mechanical shutter prevents the CCD chip from damage by the direct beam and from saturation during readout.

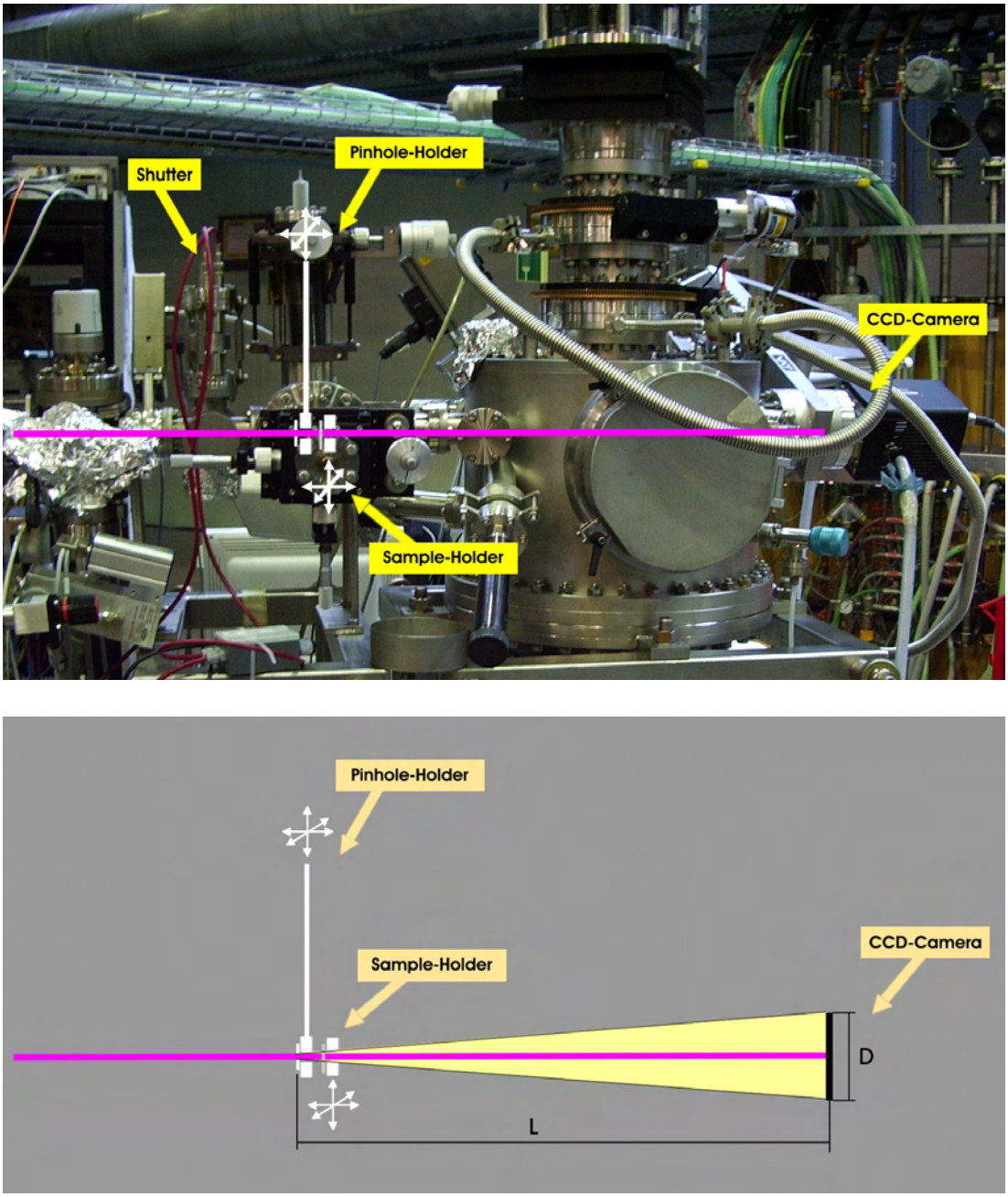

Figure 3.6: The digital in-line holography setup at BESSY II
top: Photograph of the setup. The essential parts are indicated.
bottom: Schematic drawing of the setup.
The synchrotron beam indicated by the violet line comes from the left and impinges on the pinhole which generates the Airy disc (yellow cone). The sample is mounted on a manipulator between pinhole and CCD camera. A mechanical shutter prevents the CCD chip from damage by the direct beam.

4 Resolution limit of digital in-line holography

An important parameter for imaging systems is their limit of resolution, which is given by the minimal distance two point objects may have so that they are still resolved as separate points. Sir John William Strutt, third Baron Rayleigh, was the first to develop a criterion for the resolving power of spectroscopes and telescopes [90, 91]. How this criterion leads to the commonly used Rayleigh limit of resolution and some other definitions for the resolution limit shall be introduced in the first section of this chapter. In the second section, a criterion for the resolving power of digital in-line holography will be derived and the parameters that influence this value will be discussed.

4.1 Resolving power and resolution limits

Due to the diffraction-limited nature of imaging systems, a point source is imaged as a broadened intensity distribution even in the perfect case without aberrations. The exact form of the intensity distribution depends on the geometry of the aperture, and which is also denoted as impulse response function or point spread function (PSF) [69, 70]. The formation of this distribution is described using wave optics.

In the Fraunhofer diffraction theory, the transmission of light through an aperture is calculated by multiplying the incident wave with the aperture function. The propagation beyond the aperture is then determined by the Fraunhofer integral, as discussed in chapter 2.1.5. So the parameter b in the Fraunhofer condition (equation (2.30)) is given by the largest radial distance within the aperture.

As shown in chapter 2.2, the transmission of a plane wave of wavelength λ through a single slit with width A results in an intensity distribution in the observation plane (compare equation (2.43)) which is given by [69, 73, 80]

$$I(x) = I_0 \left[\frac{\sin\left(\frac{\pi A}{\lambda}\sin\theta\right)}{\left(\frac{\pi A}{\lambda}\sin\theta\right)} \right]^2 = I_0 \,\mathrm{sinc}^2\left(\frac{A}{\lambda}\sin\theta\right). \tag{4.1}$$

Here, I_0 is the peak intensity, and θ is the angular radius. Minima occur when the argument of the sine is an integer multiple of π, so the angular radius of the

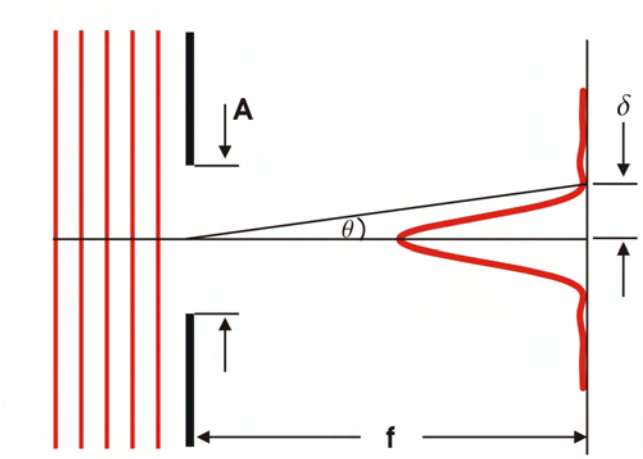

Figure 4.1: Fraunhofer diffraction from a circular aperture
The intensity in the far field is given by the Airy distribution, with the angular radius of the central maximum $\sin\theta = 1.22\frac{\lambda}{A}$.

central maximum is given by [90, 91, 92, 93]

$$\frac{\pi A}{\lambda}\sin\theta = \pi \qquad \Leftrightarrow \qquad \sin\theta = \frac{\lambda}{A}. \tag{4.2}$$

In the case of a circular aperture of diameter A, the intensity distribution changes to the Airy distribution, as introduced in chapter 2.2 (compare equation (2.55))

$$I(\theta) = I_0 \left[\frac{2\,J_1\left(\frac{\pi A}{\lambda}\sin\theta\right)}{\frac{\pi A}{\lambda}\sin\theta}\right]^2, \tag{4.3}$$

where $J_1(z)$ is the Bessel function of order 1 [69, 94]. Here, the minima occur at the roots of the Bessel function, at which the argument takes the values $\{3.832, 7.016, 10.173, 13.323, 16.470\ldots\}$ [74]. This leads to an angular radius of the central maximum of [90, 92]

$$\frac{\pi A}{\lambda}\sin\theta = 3.832 \qquad \Leftrightarrow \qquad \sin\theta = 1.22\frac{\lambda}{A}. \tag{4.4}$$

This central maximum is commonly referred to as Airy disc.

4.1.1 The Rayleigh resolution limit

Rayleigh proposed, that two equally bright points can be distinguished, if their angular distance is at least such, that the maximum of the intensity distribution of one coincides with the first minimum of the other [90, 94]. In the case, where

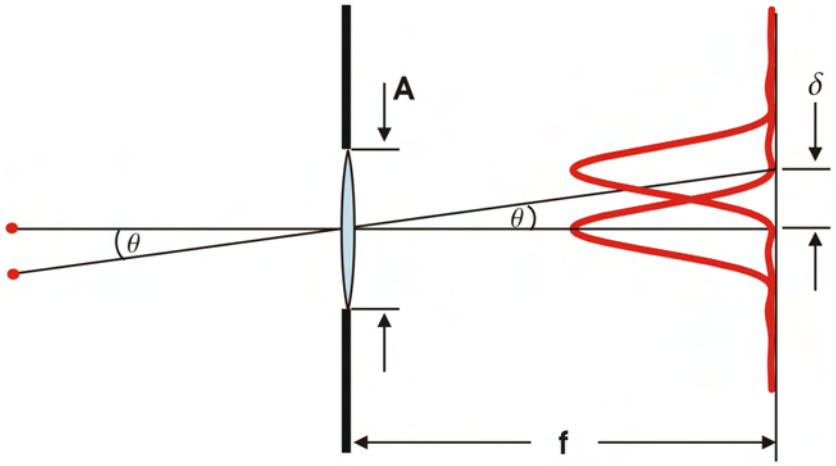

Figure 4.2: Rayleigh criterion for the resolution of two points
Two equally bright points can be distinguished, if the maximum of the intensity distribution of one coincides with the first minimum of the other.

the point objects are imaged with a lens, the aperture diameter A equals the diameter of the lens. For small angles θ, the sine can be approximated [72]:

$$\sin\theta \approx \theta \approx \tan\theta. \tag{4.5}$$

If the image is produced in the focal plane of the lens, it follows with equation (4.4) for the minimum distance δ, where the point sources can be resolved

$$\frac{\delta}{f} = \tan\theta = 1.22\frac{\lambda}{A} \qquad \Leftrightarrow \qquad \delta = 1.22\frac{\lambda f}{A}. \tag{4.6}$$

To determine the resolving power of an optical instrument like a microscope, one considers two points in the object plane, a distance δ apart, as depicted in figure 4.3. According to Rayleigh (equation (4.6)), they are resolved as distinct points, if their distance in the image is at least

$$\delta = 1.22\frac{\lambda S}{A}. \tag{4.7}$$

Typically, the objective has a high magnification, so the distance S from object to objective will be much smaller than the distance S' from objective to the image, $S \ll S'$, and even though the opening angle of the objective α might be large, α' can be considered small [67]. Therefore, the approximation

$$\alpha' \approx \frac{A/2}{S'} \tag{4.8}$$

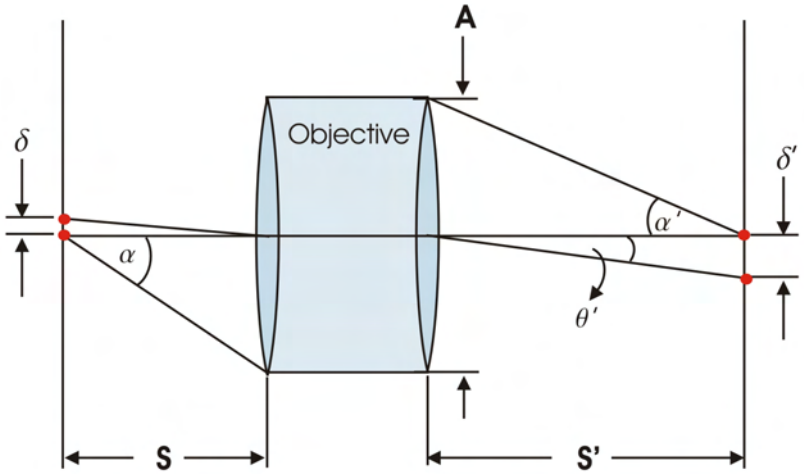

Figure 4.3: Schematic drawing of an objective
The paths of the rays needed to determine the resolving power of a microscope are depicted schematically. The size of the limiting aperture is given by the diameter A of the lens. After [67].

is valid and with equation (4.7) follows

$$\delta' = 0.61\frac{\lambda}{\alpha'}. \tag{4.9}$$

In order to get a relation between the dimension α' and δ' and α and δ on the objective side, one needs the Abbe sine condition. An optical system must fulfill this condition, if the magnitude of the spherical aberrations should not increase linearly with the distance to the optical axis [67]. It is fulfilled, if

$$\delta n \sin\alpha = \delta' n' \sin\alpha', \tag{4.10}$$

where n' and n are the refractive indices of the media on the respective side of the system [67, 73]. If medium with $n' \neq 1$ is present, λ has to be replaced by λ/n' in equation (4.9), and (4.10) can be written as

$$\delta n \sin\alpha \approx \delta' n' \alpha' = 0.61\lambda. \tag{4.11}$$

The minimal resolvable distance of two points can be now expressed as

$$\delta = 0.61\frac{\lambda}{n\sin\alpha} = 0.61\frac{\lambda}{\mathrm{NA}}, \tag{4.12}$$

where $\mathrm{NA} = n\sin\alpha$ is called the numerical aperture of a system. This Rayleigh limit was first developed by H. v. Helmholtz [70], and is valid for incoherent,

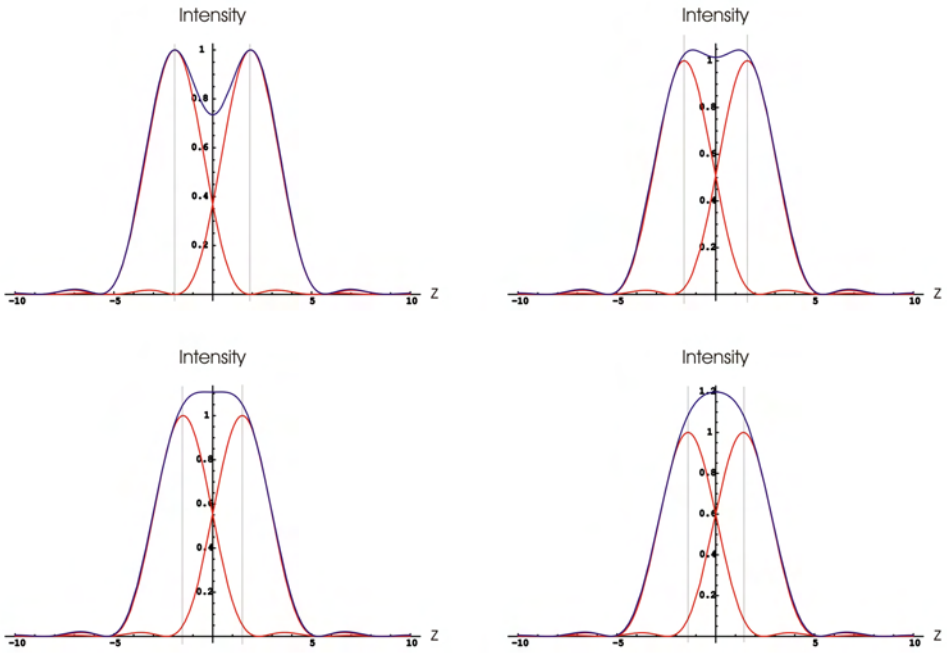

Figure 4.4: Sum of two Airy intensities

Two Airy distributions $I(z) = I_0[J_1(z)/z]^2$ (red), whose centers are a distance Δz apart, and their sum (blue).
a: $\Delta z = 3.832$. The first minimum of one distribution coincides with the maximum of the other, which corresponds to the Rayleigh resolution criterion.
b: $\Delta z = 3.20$. The maxima of the total intensity move closer together, the dip in the intensity is shallower but still recognizable.
c: $\Delta z = 3.00$. The dip in the total intensity just flattens out.
d: $\Delta z = 2.80$. The dip has vanished, only one maximum is visible.

equally bright points. Due to its simplicity, it is widely used in optics to determine the limit of resolution of optical systems, although Rayleigh himself realized, that this criterion is quite arbitrary. However, he wrote: "This rule is convenient on account of its simplicity; and it is sufficiently accurate in view of the necessary uncertainty as to what exactly is meant by resolution. Perhaps in practice somewhat more favourable conditions are necessary to secure a resolution that would be thought satisfactory." [66, 90, 94]

The Rayleigh criterion can also be formulated such that it determines whether two points are being resolved or not. Looking at figure 4.4 (a), where two Airy distributions just fulfilling the Rayleigh criterion (red curve) and their sum (blue curve) are depicted, a clear dip is visible in the total intensity curve. The intensity in the middle is 73.5% of the maximum intensity. So two points can be considered resolved, if the intensity in a linecut shows a modulation of at least 26.5% of the maximum intensity [95, 96]. In this formulation, the Rayleigh criterion can be

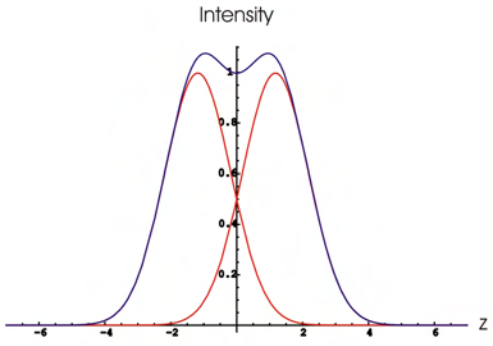

Figure 4.5: Sum of two Gaussian intensities
Two Gaussian distributions $I(z) = I_0 \exp(-z^2/(2\sigma^2))$ (red), whose centers are a distance $z = \sqrt{8 \ln 2}\sigma$ apart, and their sum (blue).

extended to partially and fully coherent illumination [95].

4.1.2 The Sparrow resolution limit

However, C. M. Sparrow was not content with Rayleigh's criterion [97]. He observed the intensity distribution created by two slits at various distances and stated that the slits can be resolved even if they are closer than given by the Rayleigh criterion. When the distance between the slits decreases, the central minimum in the intensity distribution becomes shallower (compare figure 4.4), until it disappears. The distance a of the slits is then given by his "undulator condition"

$$\left.\frac{d^2 I}{dx^2}\right|_{x=0} = 0. \tag{4.13}$$

If the distance decreases further, a single intensity maximum develops and the slits are no longer resolved. This condition leads to a resolving power which is about 26% greater than obtained by the Rayleigh criterion [97]. The Rayleigh limit, equation (4.12), can then be adapted to

$$\delta \approx 0.5 \frac{\lambda}{n \sin \alpha} = \frac{\lambda}{2\mathrm{NA}}. \tag{4.14}$$

The Sparrow resolution criterion can also be employed in the case of unequally bright points and can be generalized for coherent or partially coherent illumination [95, 98].

4.1.3 Generalization of the resolution limit

Using the above formulation of the resolution criterion considering the intensity variation, a resolution limit can be derived for point spread functions that have

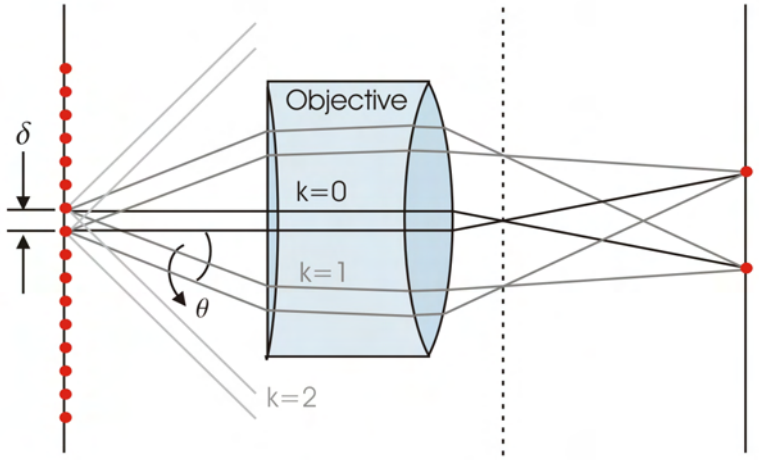

Figure 4.6: Image formation according to Abbe

no zero in the neighborhood of their central maximum as for example a Gaussian [99]

$$I(x) = \frac{1}{\sqrt{2\pi}\sigma} \exp\left\{-\frac{x^2}{2\sigma^2}\right\}. \tag{4.15}$$

Two Gaussian functions with variance σ with a distance δ of their centers equal to their full width at half maximum, $\delta = \sqrt{8\ln 2}\,\sigma$, are plotted in figure 4.5. The resulting intensity distribution exhibits a dip in the middle, the value of which is about 93% of the maximum total intensity. So this distance fulfills the Sparrow resolution criterion, and in analogy to the above, the resolution limit of a system with a Gaussian point spread function can the be determined as [99]

$$\delta = \sqrt{8\ln 2}\,\sigma. \tag{4.16}$$

4.1.4 The Abbe resolution limit

A slightly different argumentation concerning the resolution limit of microscopes than the one presented above was carried out by Ernst Abbe. As a coworker of Carl Zeiss, he occupied himself with the theoretical and experimental development of microscopy [68]. In contrast to Helmholtz, where the objects were assumed to be incoherent sources of light, he considered the case of a coherently illuminated object as for example a slit grating. If the distance between the slits is δ, this grating produces a diffraction pattern with main maxima occurring at angles [70]

$$\sin\theta_k = \frac{k\lambda}{\delta}, \tag{4.17}$$

where k is an integer. The maximum of zeroth order only contains information about the light source and not about the object. Therefore, to obtain information about the object, at least the first diffraction order has to contribute to the image formation. (In order to get a perfect image of the object, all diffraction orders are required.) Considering figure 4.6, this means that the aperture angle α of the objective must be equal to or greater than the diffraction angle θ_k, since in a microscope, the object is placed nearly in the focus of the objective. If the object is immersed in a medium with a refraction index n different from 1, λ changes to λ/n in equation (4.17) and it follows [68, 70, 75]

$$\sin\alpha \geq \sin\theta_1 = \frac{\lambda}{n\delta} \qquad \Leftrightarrow \qquad \delta \geq \frac{\lambda}{n\sin\alpha} = \frac{\lambda}{\mathrm{NA}}. \tag{4.18}$$

This value is a factor 2 greater than the Rayleigh resolution limit, equation (4.12) (if calculated for a slit instead of a circular aperture, the coefficient 0.61 is replaced by 1/2).

It has to be kept in mind, that the resolution limit as introduced by Rayleigh does not pose an ultimate limit, but was rather intended to be a means to enable a comparison between different imaging systems. Rayleigh himself emphasized "the necessary uncertainty as to what exactly is meant by resolution." [90] Furthermore, the Abbe resolution limit was derived for coherent illumination and periodic objects, while the others hold for incoherent illumination, hence it is difficult to directly compare the results [69]. And lastly, it is possible to lower the Abbe resolution limit by a factor of 2 on the cost of contrast. If the light source is not centered on the optical axis, but is placed such that it is aligned with the edge of the objective, the negative diffraction orders are discarded (compare figure 4.6), but the acceptance angle for the positive diffraction orders is doubled, leading to [67]

$$\delta \geq \frac{\lambda}{2n\sin\alpha} = \frac{\lambda}{2\mathrm{NA}}. \tag{4.19}$$

However, the loss of the negative diffraction orders conveys a decrease in contrast and might also cause other unwanted effects [67].

Altogether, the theoretical resolution limits present a guideline and lower limit for the achievable resolution since they are under the assumption of perfect conditions, which are not met in most experiments.

4.2 Resolution in digital in-line X-ray holography

From the findings above, a resolution limit for DIXH shall be derived, which is expressed in terms of the experimental parameters like pinhole diameter A, pinhole-detector distance L, wavelength λ and the like.

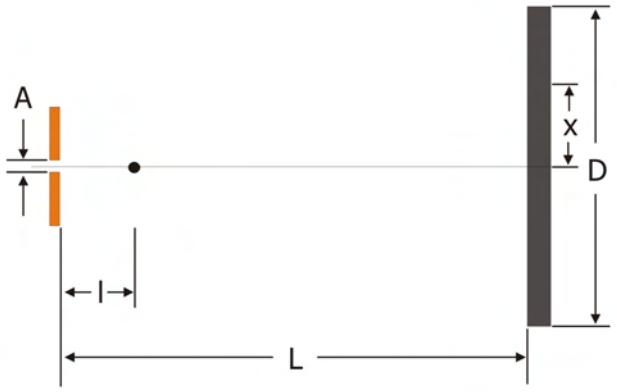

Figure 4.7: Schematic drawing of the in-line holography geometry
The sample is positioned in a distance l from the pinhole with diameter A. The pinhole-detector distance is L, and the detector has the size D. x denotes the linear distance from the center of the CCD chip.

4.2.1 Resolution in analogy to the Rayleigh limit

In analogy to the resolution limit of conventional microscopy, the resolution limit in digital in-line holography can be defined as

$$\delta = 0.61 \frac{\lambda}{\mathrm{NA}}. \tag{4.20}$$

Then, the question arises, how the numerical aperture is determined. This can be done regarding different parameters like the size of the CCD chip, the radius of the Airy disc on the detector, and the spacing of the interference fringes in relation to the pixel size. These criteria and the resulting total numerical aperture as well as the corresponding resolution limit will be discussed in the following.

Geometrical approach

As can be seen in figure 4.7, from the position of the sample, the CCD chip is seen under the half opening angle

$$\alpha = \arcsin \frac{D/2}{\sqrt{(D/2)^2 + (L-l)^2}}. \tag{4.21}$$

As the synchrotron experiments are carried out under ultra high vacuum conditions, the refractive index of the surrounding medium $n = 1$, and the geometrical numerical aperture can be written as [100, 31]

$$\mathrm{NA}_{\mathrm{geom}} = n \sin\alpha = \frac{D/2}{\sqrt{(D/2)^2 + (L-l)^2}} \approx \frac{D/2}{(L-l)}. \tag{4.22}$$

The approximation is valid, if the pinhole-sample distance l is small and the pinhole-detector distance L is much larger than the detector size D. These conditions are given in the synchrotron setup. So with equations (4.20) and (4.22) the obtainable resolution is given by

$$\delta_{\text{geom}} = 0.61\frac{\lambda(L-l)}{D/2}. \tag{4.23}$$

An upper limit for the resolution limit independent from the pinhole-sample distance l is given by

$$\delta_{\text{geom, approx}} = 0.61\frac{\lambda L}{D/2}. \tag{4.24}$$

According to this relation, a small pinhole-detector distance and a large detector size are desirable in order to achieve a small resolution limit.

Effective detector size

In the above definition for the numerical aperture, it is with the tacit understanding, that the detector is completely illuminated by the reference wave. However, since the divergent wavefront is formed by a pinhole of finite size $A > \lambda$, the opening angle of the central intensity maximum is given by equation (4.4), and the radius q of the Airy disc at the detector at distance L can be calculated as

$$\sin\theta = \frac{q}{\sqrt{q^2+L^2}} \approx \frac{q}{L} \qquad \Leftrightarrow \qquad q = L\sin\theta = 1.22\frac{L\lambda}{A}. \tag{4.25}$$

The farther the detector is positioned from the pinhole, and the smaller the pinhole diameter, the larger is the Airy disc. So the above equation implies, that large pinhole-detector distances are favorable, in contrast to the findings of equations (4.22) and (4.24). But if the Airy is larger than the detector size, it cannot be recorded completely, and the excess photon intensity is lost. So in the ideal case, the radius q just matches half the detector size D, $q = D/2$. Regarding a two dimensional quadratic detector, one could also argue that the Airy radius should match half the diagonal of the detector in order to fully illuminate it. But then the outermost interference fringes would not fit completely on the CCD chip and therefore would not contribute to the reconstruction. An optimal relation between the pinhole diameter and the pinhole-detector distance in dependence of the wavelength can be derived from equation (4.25) to be

$$\left.\frac{A}{L}\right|_{\text{opt}} = 2.44\frac{\lambda}{D}. \tag{4.26}$$

In the experiments carried out at BESSY, however, the pinhole-detector distance L was dictated by the geometry of the scattering chamber and therefore fixed.

Furthermore, although up to five different pinholes can be mounted on the pinhole holder, a change of the pinhole always leads to a slight change in the field of view, since the pinhole position cannot be reproduced with a sub-micrometer accuracy. So, when a sample is to be recorded at various wavelengths, one chooses a pinhole with a diameter that is an average of the optimum diameters and therefore might lead to an over-illumination of the detector at shorter wavelengths and an under-illumination at higher wavelengths.

In the first case, the numerical aperture is given by the geometrical one, equation (4.22). In the latter case, the effective usable detector size is limited by the position of the first minimum in the intensity distribution on the CCD chip. Therefore, if the Airy radius q (equation (4.25)) is smaller than half the detector size, the term for the numerical aperture in equation (4.22) has to be altered to

$$\mathrm{NA}_{\mathrm{eff}} = \frac{q}{\sqrt{q^2 + (L-l)^2}} \approx \frac{q}{(L-l)} = 1.22\frac{\lambda}{A}\frac{L}{L-l}, \tag{4.27}$$

and for the resolution follows

$$\delta_{\mathrm{eff}} = 0.61\frac{\lambda(L-l)}{q} = \frac{A}{2}\frac{L-l}{L} = \frac{A}{2}\left(1 - \frac{l}{L}\right). \tag{4.28}$$

Again, the approximation $\sqrt{q^2 + (L-l)^2} \approx L - l$ is valid for the synchrotron setup. The pinhole-object distance l will always be much smaller than the pinhole-detector distance L, not only, because of the experimental setup, but also because the magnification M is determined by the ratio $M = L/l$ [67], which should be high in a microscope. As a consequence, the effective resolution limit depends in first order on the pinhole diameter, and—quite surprisingly—not on the wavelength.

Fringe spacing

Up to now, the finite pixel size p of the CCD chip was not taken into account, but the recording media was assumed to be continuous. However, the effects of a quantized detector cannot always be neglected.

As introduced in chapter 2, equation (2.13), the intensity distribution of the interference pattern on the detector is given by

$$I(\vec{r}) = A_{\mathrm{ref}}^2(\vec{r}) + A_{\mathrm{obj}}^2(\vec{r}) + 2A_{\mathrm{ref}}(\vec{r})A_{\mathrm{obj}}(\vec{r})\cos\left(\varphi_{\mathrm{ref}} - \varphi_{\mathrm{obj}}\right). \tag{4.29}$$

For an ideal point source emitting a spherical wave (compare equation (2.10)) with wavevector $k = 2\pi/\lambda$ and complex amplitude

$$A_{\mathrm{ref}}(\vec{r}) = \frac{A_0}{r}\exp\{-ikr\}, \tag{4.30}$$

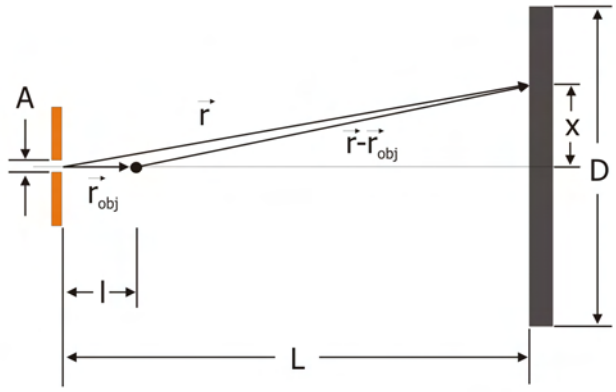

Figure 4.8: Schematic drawing of the in-line holography geometry
The sample is positioned in a distance l from the pinhole with diameter A. The pinhole-detector distance is L, and the detector has the size D. x denotes the linear distance from the center of the CCD chip.

and a point object at position $\vec{r}_{\mathrm{obj}}$ creating a scattered spherical wave

$$A_{\mathrm{obj}}(\vec{r}) = \frac{A_1}{|\vec{r} - \vec{r}_{\mathrm{obj}}|} \exp\left\{-ik\,|\vec{r} - \vec{r}_{\mathrm{obj}}|\right\}, \tag{4.31}$$

equation (4.29) rewrites as

$$I(\vec{r}) = \frac{A_0^2}{r^2} + \frac{A_1^2}{|\vec{r} - \vec{r}_{\mathrm{obj}}|^2} + 2\frac{A_0 A_1}{r\,|\vec{r} - \vec{r}_{\mathrm{obj}}|} \cos\left\{k\,(r - |\vec{r} - \vec{r}_{\mathrm{obj}}|)\right\}. \tag{4.32}$$

The first two terms result in a smoothly varying background intensity, while the last term, the hologram term, describes the interference pattern. If the object is positioned on the optical axis at a distance l from the point source as illustrated in figure 4.8, the pattern consists of concentric circular fringes symmetric to the optical axis with decreasing spacing toward periphery as plotted in figure 4.9. The fringe spacing s is the distance on the detector on which the argument of the cosine experiences a phase difference of 2π. Since the pattern exhibits radial symmetry, it suffices to calculate the fringe spacing for one dimension on the detector. With x being the radial distance from the center of the CCD chip, the absolute values in equation (4.32) can be expressed as

$$r = \sqrt{L^2 + x^2} \qquad \text{and} \tag{4.33}$$

$$|\vec{r} - \vec{r}_{\mathrm{obj}}| = \sqrt{(L - l)^2 + x^2}, \tag{4.34}$$

so the argument of the cosine in equation (4.32) is a function of x of the form

$$\varphi(x) = k\,(r - |\vec{r} - \vec{r}_{\mathrm{obj}}|) = k\left(\sqrt{L^2 + x^2} - \sqrt{(L - l)^2 + x^2}\right). \tag{4.35}$$

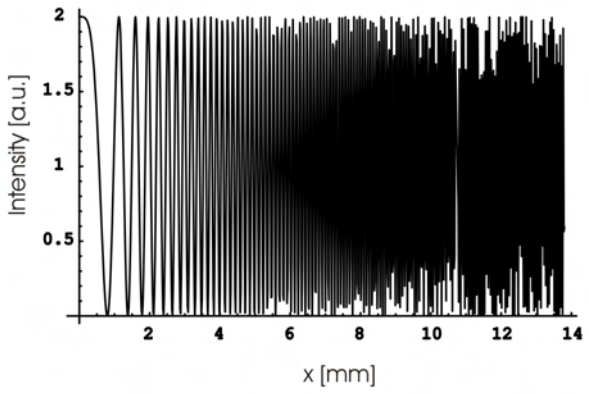

Figure 4.9: Fringe pattern of a single point scatterer
The sample is positioned in a distance $l = 5$ mm from the pinhole. The pinhole-detector distance is $L = 800$ mm, the detector has the size $D = 27.6$ mm, and the wavelength is $\lambda = 5$ nm. x denotes the linear distance from the center of the CCD chip. The interference pattern consists of concentric circular fringes with decreasing spacing for larger x.

The fringe spacing condition is

$$|\varphi(x+s) - \varphi(x)| = 2\pi. \tag{4.36}$$

Since for the fringes farther from the center the assumption $s \ll x$ is valid, the difference can be approximated with a derivative [100]

$$\varphi(x+s) - \varphi(x) = s\,\frac{\varphi(x+s) - \varphi(x)}{s} \approx s\,\varphi'(x). \tag{4.37}$$

It is

$$\varphi'(x) = k\left(\frac{x}{\sqrt{L^2+x^2}} - \frac{x}{\sqrt{(L-l)^2+x^2}}\right) \tag{4.38}$$

and thus equations (4.36) and (4.37) give for the fringe spacing [32]

$$\begin{aligned} s &= \frac{\lambda}{x}\frac{\sqrt{L^2+x^2}\,\sqrt{(L-l)^2+x^2}}{\sqrt{L^2+x^2} - \sqrt{(L-l)^2+x^2}} \\ &= \lambda\frac{\sqrt{1+(L/x)^2}\,\sqrt{1+((L-l)/x)^2}}{\sqrt{1+(L/x)^2} - \sqrt{1+((L-l)/x)^2}}. \end{aligned} \tag{4.39}$$

According to the Nyquist-Shannon sampling theorem [101], which says, that a function which contains frequencies up to $f_{\max}$ "is completely determined by

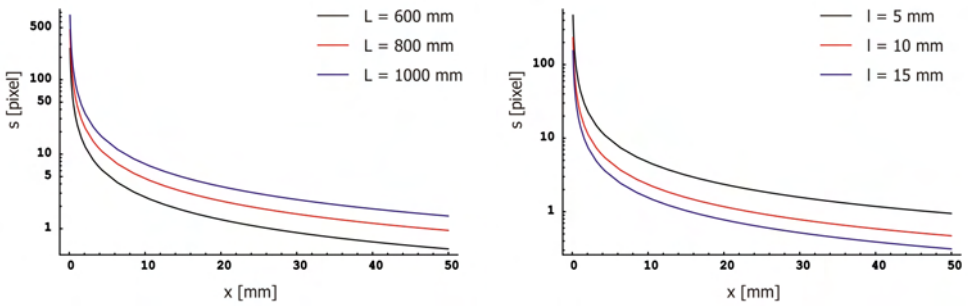

Figure 4.10: Fringe spacing s in dependence on L and l
In this example, the detector size $A = 27.6$ mm, the pixel size $p = 13.5$ µm, the pinhole diameter $A = 500$ nm, and the wavelength $\lambda = 5$ nm.
left: The pinhole-sample distance is $l = 5$ mm. With increasing pinhole-detector distance L the fringe spacing s increases.
right: For a fixed detector distance $L = 800$ mm the fringe spacing s decreases with increasing sample distance l.

giving its ordinates at a series of points spaced $[\ldots][2f_{\max}]$ apart" [102], the fringe spacing s must be at least twice the pixel size p in order to be resolved by the CCD chip [103]. By setting $s = 2p$ and solving equation (4.39) for x, one gets the maximum radius within which the fringes can be resolved. Outside this circle, the fringes are too narrow, the signal is not sampled sufficiently, and the intensity on the detector contains no information about the hologram. So this radius limits the numerical aperture to

$$\mathrm{NA}_{\mathrm{fringe}} = \frac{x}{\sqrt{x^2 + (L-l)^2}} \approx \frac{x}{(L-l)}. \tag{4.40}$$

However, equation (4.39) cannot be solved analytically. But if $x \ll L$ and $x \ll (L-l)$—what is again valid in the synchrotron experiments—it can be approximated as [100]

$$s = \frac{\lambda}{x}\frac{L(L-l)}{l}, \tag{4.41}$$

the maximum radius is

$$x = \frac{\lambda}{2p}\frac{L(L-l)}{l}, \tag{4.42}$$

and equation (4.40) has the form

$$\mathrm{NA}_{\mathrm{fringe}} = \frac{\lambda}{2p}\frac{L}{l}. \tag{4.43}$$

The resolution limit is then

$$\delta_{\mathrm{fringe}} = 0.61\frac{\lambda}{\mathrm{NA}_{\mathrm{fringe}}} = 1.22\frac{pl}{L}. \tag{4.44}$$

Again quite surprisingly, this resolution limit also does not depend on the wavelength, but only on the pixel size p and the magnification $M = L/l$. It however confirms the Nyquist-Shannon sampling theorem, that structures can be resolved only if their size δ is—after magnification by the factor $M = L/l$—larger than the pixel pitch p.

Total numerical aperture and total resolution limit

In total, the resulting actual numerical aperture is given by the minimum of equation (4.22), equation (4.27), and equation (4.43)

$$\begin{aligned} \mathrm{NA}_{\mathrm{total}} &= \min\left\{\mathrm{NA}_{\mathrm{geom}}, \mathrm{NA}_{\mathrm{eff}}, \mathrm{NA}_{\mathrm{fringe}}\right\} \\ &= \min\left\{\frac{D/2}{(L-l)}, 1.22\frac{\lambda}{A}\frac{L}{L-l}, \frac{\lambda}{2p}\frac{L}{l}\right\}, \end{aligned} \tag{4.45}$$

while the total resolution limit is the maximum of equation (4.23), equation (4.28), and equation (4.44)

$$\begin{aligned} \delta_{\mathrm{total}} &= \max\left\{\delta_{\mathrm{geom}}, \delta_{\mathrm{eff}}, \delta_{\mathrm{fringe}}\right\} \\ &= \max\left\{0.61\frac{\lambda(L-l)}{D/2}, \frac{A}{2}\frac{L-l}{L}, 1.22\frac{pl}{L}\right\}. \end{aligned} \tag{4.46}$$

In figure 4.11 a comparison of the different numerical apertures for fixed object distance l and varying detector distance L is illustrated. The fixed parameters are the detector size $D = 27.6$ mm, the pixel size $p = 13.5$ µm, the pinhole diameter $A = 500$ nm, the pinhole-sample distance $l = 5$ mm, and the wavelength $\lambda = 5$ nm. These values are typical for our synchrotron experiments. The actual numerical aperture at a certain distance L is given by the minimum of $\mathrm{NA}_{\mathrm{geom}}$ (black), $\mathrm{NA}_{\mathrm{eff}}$ (red), and $\mathrm{NA}_{\mathrm{fringe}}$ (blue). For small pinhole-detector distances L and constant pinhole-sample distance l the magnification $M = L/l$ is small, and according to equation (4.43) the numerical aperture with respect to the fringe spacing is small, since the interference fringes cannot spread properly and thus are resolved only very close to the optical axis. At longer detector distances, the fringes can be resolved within the first minimum of the Airy intensity distribution, but the radius of the Airy disc is smaller than half the detector size D, since it scales with the detector distance L (equation (4.25)). Only at distances $L > (AD)/(2.44\lambda)$ the size of the CCD chip limits the numerical aperture and the total numerical aperture is limited by the geometrical one.

Since the total resolution limit δ_{total} depends inversely on the numerical aperture NA, it is given by the maximum of δ_{geom} (black curve in figure 4.12), δ_{eff} (red curve), and δ_{fringe} (blue curve), depending on which numerical aperture is the smallest at the respective detector distance.

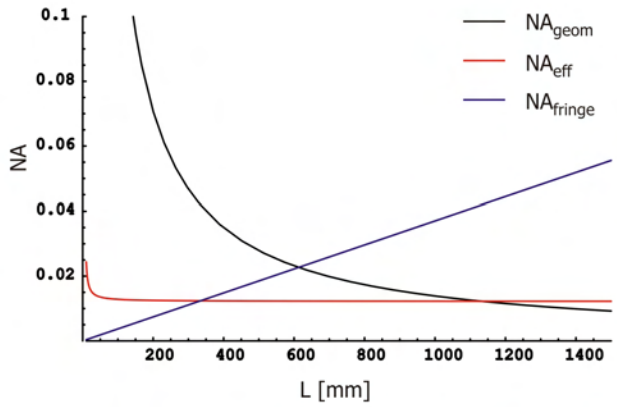

Figure 4.11: Comparison of the different NA for fixed l and varying L
The actual numerical aperture is given by the minimum of $\mathrm{NA}_{\mathrm{geom}}$ (black), $\mathrm{NA}_{\mathrm{eff}}$ (red), and $\mathrm{NA}_{\mathrm{fringe}}$ (blue). In this example, the detector size $D = 27.6$ mm, the pixel size $p = 13.5$ µm, the pinhole diameter $A = 500$ nm, the pinhole-sample distance $l = 5$ mm, and the wavelength $\lambda = 5$ nm. For small pinhole-detector distances L the interference fringes cannot spread properly and thus are resolved only very close to the optical axis. This radius x limits the numerical aperture. At longer detector distances, the fringes can be resolved within the first minimum of the Airy intensity distribution, but the radius of the Airy disc is smaller than half the detector size D. Only at distances $L > (AD)/(2.44\lambda)$ the size of the CCD chip limits the numerical aperture.

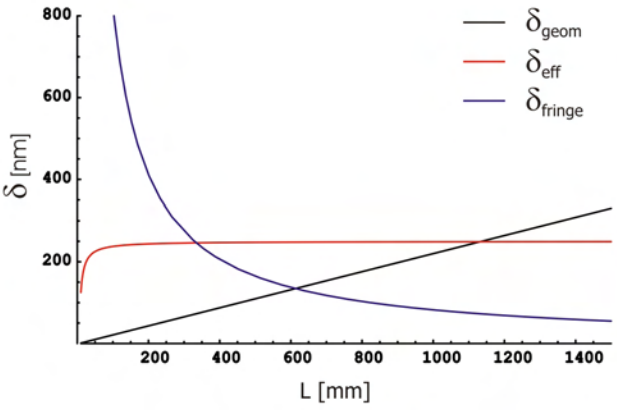

Figure 4.12: Comparison of the different δ for fixed l and varying L
The actual resolution limit is given by the maximum of δ_{geom} (black), δ_{eff} (red), and δ_{fringe} (blue). At low pinhole-detector distances, the fringe-spacing criterion limits the resolution. With increasing distance, the fringe spacing increases and the resolution is limited by the size of the Airy disc on the detector. When $L > (AD)/(2.44\lambda)$, the limiting factor is the size of the CCD chip.

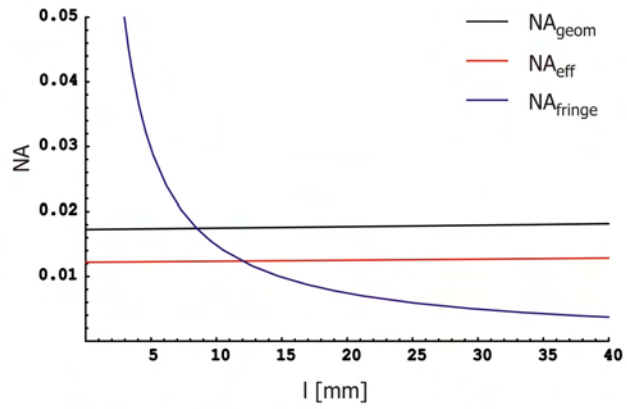

Figure 4.13: Comparison of the different NA for fixed L and varying l
The actual numerical aperture is given by the minimum of NA_{geom} (black), NA_{eff} (red), and NA_{fringe} (blue). Here, the parameters are the same as in figure 4.11, with the difference that the pinhole-detector distance is fixed to $L = 800$ mm and the pinhole-sample distance l varies. For small distances, the magnification $M = L/l$ is high and the limiting radius x, where the fringe spacing is smaller than two pixels, is large. The numerical aperture is limited by the geometrical or the effective one, depending on the pinhole-detector distance being larger or smaller than the optimum $L = (AD)/(2.44\lambda)$. For larger sample distances l, the fringe spacing decreases, and the usable detector size is limited by the radius x.

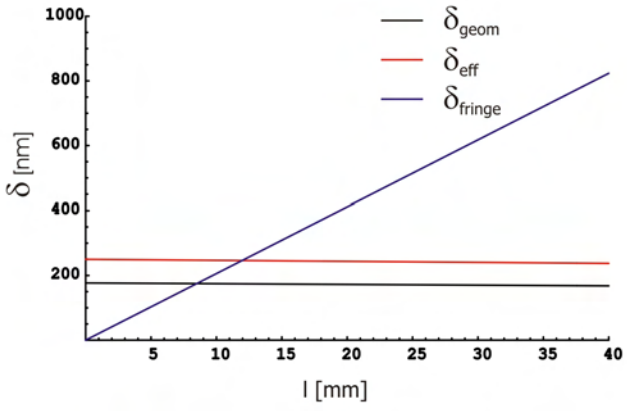

Figure 4.14: Comparison of the different δ for fixed L and varying l
The actual resolution limit is given by the maximum of δ_{geom} (black), δ_{eff} (red), and δ_{fringe} (blue). At low pinhole-sample distances, the resolution is limited by either the geometrical or the effective numerical aperture, depending on the pinhole-detector distance being larger or smaller than the optimum $L = (AD)/(2.44\lambda)$. For larger sample distances l, the fringe spacing decreases, and the usable detector size is limited by the radius x.

For a constant pinhole-detector distance L and varying pinhole-sample distance l two cases can occur; either $L > (AD)/(2.44\lambda)$ and the geometrical numerical aperture is smaller than the effective one or $L < (AD)/(2.44\lambda)$ and $\mathrm{NA}_{\mathrm{eff}} < \mathrm{NA}_{\mathrm{geom}}$. In either case, the smaller of the two limits the total numerical aperture at small sample distances l, while at larger sample distances the minimal numerical aperture is given by the fringe resolution criterion $\mathrm{NA}_{\mathrm{fringe}}$. In figure 4.13 the pinhole-detector distance $L = 800$ mm, which is smaller than the optimal distance $L_{\mathrm{opt}} = (AD)/(2.44\lambda) = 1131.1$ mm. As in figure 4.11, it is the detector size $D = 27.6$ mm, the pixel size $p = 13.5$ µm, the pinhole diameter $A = 500$ nm, and the wavelength $\lambda = 5$ nm. So the effective numerical aperture (red curve) poses the limit up to a sample distance $l = 12.0$ mm, where $\mathrm{NA}_{\mathrm{eff}} = \mathrm{NA}_{\mathrm{fringe}}$. At larger sample distances, the fringe spacing decreases and becomes to small to be resolved throughout the whole Airy disc. In this range, the total numerical aperture is determined by $\mathrm{NA}_{\mathrm{fringe}}$ (blue curve).

The corresponding resolution limits are depicted in figure 4.14. Although not discernible in the drawing but what becomes clear looking at equations (4.23) and (4.28), both resolution limits δ_{geom} as well as δ_{eff} have a negative slope. So the minimal total resolution is reached at a pinhole-sample distance, where the larger of those two resolution limits intersects the resolution limit δ_{fringe}. By equating $\delta_{\mathrm{geom}} = \delta_{\mathrm{fringe}}$ (equations (4.23) and (4.44)) and $\delta_{\mathrm{eff}} = \delta_{\mathrm{fringe}}$ (equations (4.23) and (4.44)) respectively, an optimal pinhole-sample distance can be found:

$$l_{\mathrm{geom,opt}} = \frac{L}{\frac{pd}{L\lambda} + 1} \approx \frac{L^2\lambda}{pD} \quad \text{and} \tag{4.47}$$

$$l_{\mathrm{eff,opt}} = \frac{L}{\frac{2.44p}{A} + 1} \approx \frac{LA}{2.44p}. \tag{4.48}$$

Both approximations are valid in the synchrotron setup.

A global resolution minimum is reached, when the experimental parameters match in a way, that all three curves in figure 4.14 intersect in a single point. At this point, the pinhole-detector distance L_{opt} is (compare equation (4.26))

$$L_{\mathrm{opt}} = \frac{AD}{2.44\lambda}, \tag{4.49}$$

the optimal pinhole-sample distance is [100]

$$l_{\mathrm{opt}} = \frac{L}{\frac{pD}{L\lambda} + 1} = \frac{L}{\frac{2.44p}{A} + 1}, \tag{4.50}$$

and for the resolution limit follows [100]

$$\delta_{\mathrm{opt}} = \frac{A}{2}\frac{L-l}{L} = \frac{A}{2}\frac{1}{1 + \frac{A}{2.44p}} \approx \frac{A}{2} \quad \text{and} \tag{4.51}$$

$$\delta_{\mathrm{opt}} = 1.22\frac{pl}{L} = \frac{1}{\frac{2}{A} + \frac{1}{1.22p}} \approx \frac{A}{2}, \tag{4.52}$$

respectively. That means, the best achievable resolution equals the pinhole radius! In the experiments presented in this thesis, however, the pinhole-detector distance was dictated by the geometry of the scattering chamber, and pinholes in certain sizes only were available. So by choosing the pinhole diameter, the achievable resolution and the accessible wavelength range are predefined.

According to Kreuzer [29, 43, 44], the sample has to be positioned at a distance l to the pinhole such that the Fraunhofer condition $\delta^2 \ll l\lambda$ (compare equation (2.30)) is fulfilled, in order to achieve a resolution of δ. This condition is easily met in the synchrotron experiments for l_{opt}, where the resolution δ is in the sub-micrometer range and the wavelength is between 2 nm and 14 nm. From equation (4.20) Kreuzer also derives a maximal allowed detector distance: Since

$$\delta = 0.61\frac{\lambda}{\mathrm{NA}} = 0.61\frac{\lambda}{\sin\alpha} \tag{4.53}$$

and

$$\frac{D/2}{L} = \tan\alpha = \frac{1}{\sqrt{\frac{1}{\sin^2\alpha} - 1}} \tag{4.54}$$

it follows for the maximal detector distance

$$L_{\max} = \frac{D}{2}\sqrt{\left(\frac{\delta}{0.61\lambda}\right)^2 - 1} \approx \frac{D\delta}{1.22\lambda}. \tag{4.55}$$

These considerations are based on perfectly spherical waves, which always provide a homogeneous illumination of the detector. But taking into account the finite size of the pinhole and the resulting finite size of the Airy disc, this distance $L_{\max}$ should not be smaller than the detector distance, where the Airy disc fully illuminates the CCD chip, equation (4.26) and equation (4.49). Thus it follows for the resolution limit

$$\frac{D}{2}\sqrt{\left(\frac{\delta}{0.61\lambda}\right)^2 - 1} = \frac{DA}{2.44\lambda} \qquad \Leftrightarrow \tag{4.56}$$

$$\delta = \sqrt{\left(\frac{A}{2}\right)^2 - (0.61\lambda)^2} \approx \frac{A}{2}. \tag{4.57}$$

This result confirms the total resolution limit expressed in equation (4.52). All the above considerations were carried out for point scatterers on the optical axis. For points off the axis, the interference fringes will be cut off asymmetrically by the finite detector, which will lead to a higher resolution limit [100].

4.2.2 Resolution in analogy to the Abbe limit

In analogy to the consideration leading to the Abbe resolution limit (equation (4.18)), one can also observe the interference pattern produced by two objects. In

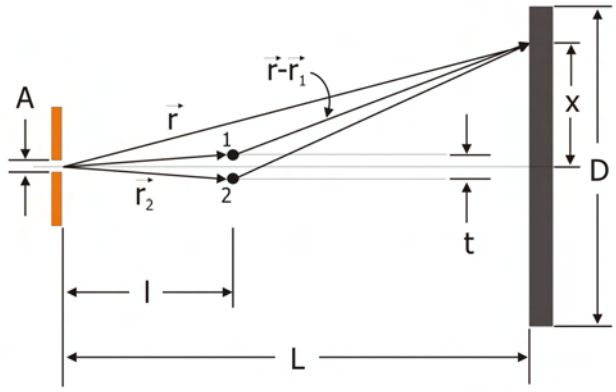

Figure 4.15: Schematic drawing of the in-line holography geometry
Two samples are positioned separated by a distance t symmetrically to the optical axis in a distance l from the pinhole. The pinhole diameter is A, the pinhole-detector distance is L, and the detector has the size D. x denotes the linear distance from the center of the CCD chip.

figure 4.15, two samples are positioned separated by a distance t symmetrically to the optical axis in a distance l from the pinhole. To describe the intensity distribution on the detector for two point scatterers, equation (4.32) has to be extended to [31, 32]

$$\begin{aligned} I(\vec{r}) \;=\; & \frac{{A_0}^2}{r^2} + \frac{{A_1}^2}{|\vec{r}-\vec{r}_1|^2} + \frac{{A_2}^2}{|\vec{r}-\vec{r}_2|^2} \\ & + \left[2\frac{A_0 A_1}{r\,|\vec{r}-\vec{r}_1|} \cos\left\{k\left(r - |\vec{r}-\vec{r}_1|\right)\right\} \right. \\ & \left. + 2\frac{A_0 A_2}{r\,|\vec{r}-\vec{r}_2|} \cos\left\{k\left(r - |\vec{r}-\vec{r}_2|\right)\right\} \right] \\ & + 2\frac{A_1 A_2}{|\vec{r}_1-\vec{r}_2|^2} \cos\left\{k\left(|\vec{r}-\vec{r}_1| - |\vec{r}-\vec{r}_2|\right)\right\}. \end{aligned} \tag{4.58}$$

The first three terms result in a smoothly varying background intensity, while the last term describes the interference pattern of the two objects. Since for holography the amplitudes A_1 and A_2 must be smaller than the amplitude of the reference wave A_0, this interference term can be neglected. So the term in the squared brackets remains as hologram term.

Since the separation t between the two identical point scatterers is small, it is $|\vec{r}-\vec{r}_1| \approx |\vec{r}-\vec{r}_2|$ [31, 32]. Furthermore holds $A_1 = A_2$ and $|\vec{r}_1| = |\vec{r}_2|$. With the sum formula for the cosine [74]

$$\cos u + \cos v = 2\cos\frac{u+v}{2}\cos\frac{u-v}{2} \tag{4.59}$$

the hologram term can then be rewritten as [31, 32]

$$\begin{aligned} I_{\mathrm{H}}(\vec{r}) &= 4\frac{A_0 A_1}{r\,|\vec{r}-\vec{r}_1|}\cos\left\{k\frac{2r-|\vec{r}-\vec{r}_1|-|\vec{r}-\vec{r}_2|}{2}\right\} \\ &\quad\times\cos\left\{k\frac{|\vec{r}-\vec{r}_1|-|\vec{r}-\vec{r}_2|}{2}\right\}. \end{aligned} \tag{4.60}$$

Similar expressions appear in acoustics, when two harmonic waves with slightly different frequencies f_1 and f_2 add. The result is a harmonic wave with frequency $f_{\mathrm{sum}} = (f_1 + f_2)/2$ with a harmonic modulation of the amplitude. This so called beating has a frequency of $f_{\mathrm{beat}} = (f_1 - f_2)/2$ and can be heard as the sound periodically growing louder and softening. The same effect applies in equation (4.60); the first cosine term describes the fringe pattern, while the second cosine term imposes the modulation.

Using the experimental parameters, the absolute values of the vectors in equation (4.60) can be expressed as

$$r = \sqrt{L^2+x^2} \qquad \text{and} \tag{4.61}$$

$$|\vec{r}-\vec{r}_1| = \sqrt{(L-l)^2+(x-t/2)^2}, \tag{4.62}$$

$$|\vec{r}-\vec{r}_2| = \sqrt{(L-l)^2+(x+t/2)^2}, \tag{4.63}$$

and the hologram term is [31, 32]

$$\begin{aligned} I_{\mathrm{H}}(x) &= 4\frac{A_0 A_1}{\sqrt{L^2+x^2}\sqrt{(L-l)^2+(x-t/2)^2}} \\ &\quad\times\cos\left\{k\frac{2\sqrt{L^2+x^2}-\sqrt{(L-l)^2+(x-t/2)^2}-\sqrt{(L-l)^2+(x+t/2)^2}}{2}\right\} \\ &\quad\times\cos\left\{k\frac{\sqrt{(L-l)^2+(x-t/2)^2}-\sqrt{(L-l)^2+(x+t/2)^2}}{2}\right\}. \end{aligned} \tag{4.64}$$

In figure 4.16, the one-dimensional fringe pattern resulting from the two cosine terms is plotted for various separations t. The amplitudes are not taken into account since they vary only slowly over the whole detector range. The point scatterers are positioned at a distance $l = 5$ mm from the pinhole. The pinhole-detector distance is $L = 800$ mm, the detector has the size $D = 27.6$ mm, and the wavelength is $\lambda = 5$ nm. All those values are typical for the synchrotron experiments. For $t = 0$, what is equivalent to a single object, the interference pattern consists of concentric fringes with equal intensity. When the separation t increases, the fringe spacing does not change significantly. However, the modulation frequency increases and more and more maxima of the beat pattern appear on the detector. So obviously, the information about the separation distance t is contained in the modulation of the fringe pattern [32]. In order to capture information on the separation of the point scatterers, it is—in analogy to the Abbe

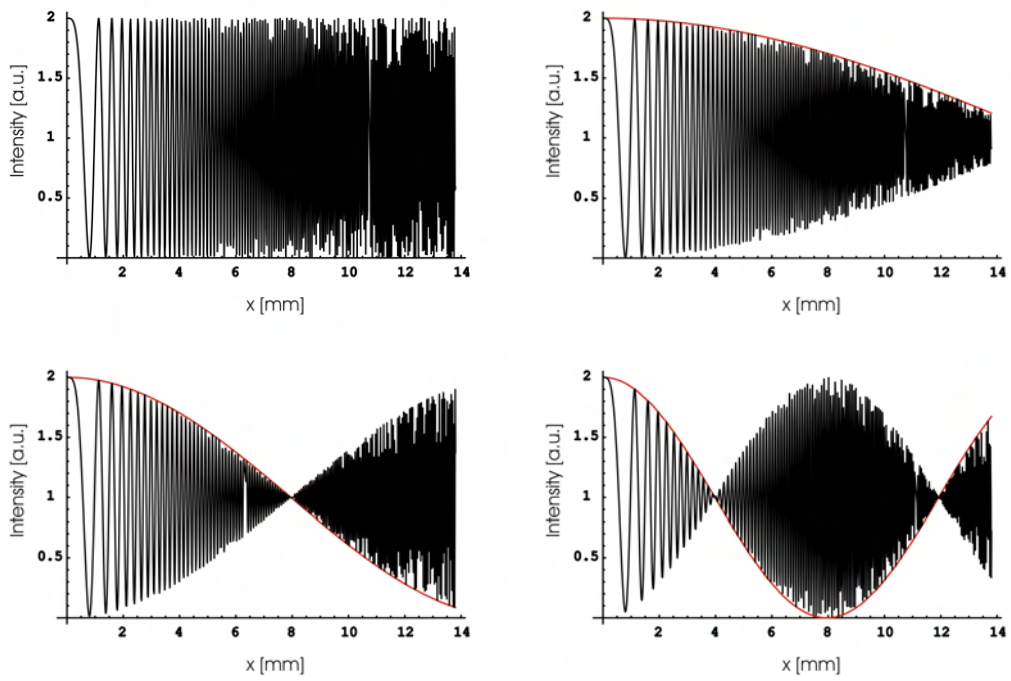

Figure 4.16: Fringe modulation for two point scatterers
Two samples are positioned separated by a distance t symmetrically to the optical axis in a distance $l = 5$ mm from the pinhole. The pinhole-detector distance is $L = 800$ mm, the detector has the size $D = 27.6$ mm, and the wavelength is $\lambda = 5$ nm. x denotes the linear distance from the center of the CCD chip.
top left: $t = 0$. Fringe pattern produced by a single point scatterer. The fringe spacing itself does not change significantly for small $t \neq 0$.
For increasing separation t the modulation frequency increases and more and more maxima of the beat pattern appear on the detector.
top right: $t = 0.125$ µm.
bottom left: $t = 0.250$ µm.
bottom right: $t = 0.500$ µm.

criterion discussed in section 4.1.4—therefore necessary to have the first modulation maximum on the detector. Nodes in the modulation occur, when the cosine equals zero, that is when the argument is an odd multiple of $\pi/2$. Modulation maxima occur in between, when

$$k\frac{\sqrt{(L-l)^2+(x-t/2)^2}-\sqrt{(L-l)^2+(x+t/2)^2}}{2}=n\pi, \tag{4.65}$$

where n is an integer. If the first maximum is just at the edge of the CCD chip, then $n=1$ and $x=D/2$. Hence it follows for the resolvable distance [31, 32]

$$\delta_{\text{Kreuzer}}=t=\lambda\frac{\sqrt{(L-l)^2+(D/2)^2}}{D/2}=\frac{\lambda}{\text{NA}_{\text{geom}}}, \tag{4.66}$$

where the numerical aperture NA is defined as in (4.22). In the derivation of this expression it was assumed that the separation t is small compared to the object-screen distance $L-l$. This result is the same as the Abbe resolution limit, equation (4.18), although the derivation was quite different.

Again, the considerations above were under the assumption of a perfect spherical reference wave. In the case of a pinhole with finite size A, the effective detector size might be limited by the radius of the Airy disc $q<D/2$. Then the geometrical numerical aperture NA_{geom} in equation (4.66) has to be replaced by the effective one, NA_{eff} (equation (4.27)).

Due to the lacking definition of resolution itself [90] it cannot be said with certainty, which of the two approaches for the resolution limit, equation (4.46) or equation (4.66), presents the ultimate limit. To enable a comparison with optical light microscopy, the first equation has to be applied. However, since the Abbe limit was derived for coherent illumination, what is certainly the case in holography, the second equation should not be neglected. So in the following part of this thesis, both numbers will be given as a guideline and to allow a comparison of the different predictions with each other and with the experimental results.

4.2.3 Depth resolution

For most imaging systems only a small range along the optical axis exists, over which two points can be simultaneously imaged in focus. This range is denoted as depth resolution δ_{depth}. How it depends on the parameters of the imaging system will be derived in the following.

As illustrated in figure 4.17, a displacement of the object of Δg along the optical axis leads to a displacement of the object plane of Δb. Hence the point object is imaged as a spot with diameter Δx in the original object plane.

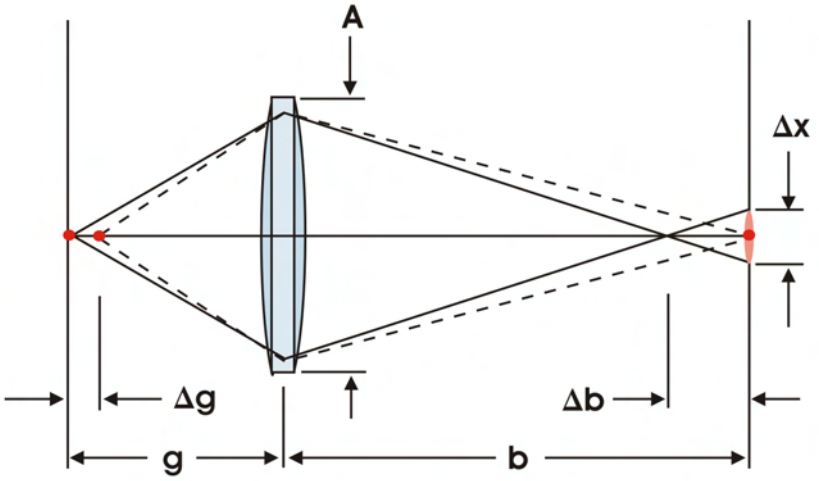

Figure 4.17: Geometry of depth resolution
A displacement of the object of Δg along the optical axis leads to a displacement of the object plane of Δb. Hence the point object is imaged as a spot with diameter Δx in the original object plane. The size of the limiting aperture is given by the diameter A of the lens. After [68].

If the displacement Δg is small compared to the object distance g, it is [68]

$$\frac{\Delta b}{b} = -\frac{\Delta g}{g}. \tag{4.67}$$

And the theorem of intersecting lines gives for the diameter of the spot

$$\Delta x = \left|\frac{A\Delta b}{b}\right| = \left|\frac{A\Delta g}{g}\right| \approx \left|\frac{A\Delta g}{f}\right|. \tag{4.68}$$

The image is unchanged if the spot size Δx is smaller than the diameter of the diffraction limited Airy disc of the point object. The radius of the Airy disc was introduced in equation (4.6). Hence it follows for the allowed displacement [68]

$$\delta_{\text{depth}} = \Delta g = \Delta x \frac{f}{A} < 2 \cdot 1.22 \frac{\lambda f}{A} \frac{f}{A} = 0.61\lambda \left(\frac{f}{A/2}\right)^2 = 0.61 \frac{\lambda}{\text{NA}^2}. \tag{4.69}$$

So the depth resolution limit depends quadratically on the numerical aperture of the system. It should be noted that in literature, instead of the factor 0.61 also the values 0.5 [31, 32] and 1 [68] can be found, corresponding to the respective value in the definition of the lateral resolution limit. Since for the numerical aperture holds $\text{NA} = \sin\alpha \leq 1$, the depth resolution is always larger than the lateral resolution, equation (4.12).

By inserting the expression for the numerical apertures developed in section 4.2.1, equations (4.22),(4.27), and (4.43), it leads to an expression for the depth resolution limit in terms of the experimental parameters. The same considerations as were carried out above result in a total depth resolution of

$$\delta_{\text{depth}} = \frac{A^2}{2.44\lambda}. \tag{4.70}$$

So for an improved depth resolution, the size of the pinhole is even more crucial than for the lateral resolution limit. As an example, to achieve a depth resolution better than 1 µm at a wavelength of $\lambda = 2$ nm, a pinhole diameter smaller than $A = 70$ nm is necessary.

In the synchrotron experiments, the largest numerical aperture obtained is NA $= D/(2L) = 0.017$ ($L = 800$ mm, $D = 27.6$ mm). With the shortest used wavelength of $\lambda = 2.48$ nm ($E = 500$ eV), equation (4.69) leads to a depth resolution of at least $\delta_{\text{depth}} = 5.2$ µm. The smallest pinhole, $A = 250$ nm, used at wavelengths up to $\lambda = 5.6$ nm gives with equation (4.70) a total depth resolution of $\delta_{\text{depth}} = 4.5$ µm. Since these values are larger than the thickness of most of the examined samples, no three dimensional information was obtained in the experiments. Thus, in the following chapters, the depth resolution will not be taken into account.

5 Pinholes

As discussed in chapter 4, the achievable lateral and depth resolution depends on the pinhole diameter. Therefore, for given experimental parameters—that is pinhole-detector distance, detector size, and wavelength—an ideal pinhole size exists. Additionally, when working with X-rays, the pinhole material has to be of a certain thickness in order to block the part of the synchrotron beam that impinges on the aperture and does not pass the pinhole. In the following chapter, these specifications will be discussed and it will be explained, how the pinholes used in this thesis were produced by Focused Ion Beam (FIB) milling. The different pinhole types used in this thesis are introduced in the last part of this chapter.

5.1 Pinhole requirements

Holographic microscopy in the Gabor geometry requires a divergent wavefront, which is in the perfect case a spherical wave. One way to produce a spherical wavefront is to use a pinhole with a diameter in the order of the wavelength of the light used. For laser based holography diameters of about 500 nm are ideal. Apertures of those sizes can be produced by laser drilling in nickel substrates of about 2.5 µm to 5.0 µm thickness and are commercially available [104, 105]. For experiments with synchrotron radiation in the Vacuum-Ultraviolet (VUV) or soft X-ray regime[1] pinhole sizes of few nanometers are required to generate spherical wavefronts. As will be explained below, it is not absolutely necessary to have such small pinholes, and larger pinhole diameters are sometimes even advantageous.

When a wave is diffracted from an aperture which is larger than the wavelength, the intensity distribution in the far field is described by the Airy distribution, equation (2.55), as introduced in chapter 2.2. So the pinhole diameter A determines the opening angle α of the divergent beam for a given wavelength λ (compare equation (4.4))

$$\sin\alpha = 1.22\lambda/A. \tag{5.1}$$

But it also influences the photon current through the pinhole n_{pinhole}, that is the number of photons N that pass the clear aperture in a certain time interval

[1] The VUV region is defined having wavelengths from 200 nm down to 10 nm, followed by the soft X-ray region from 10 nm down to 0.1 nm [69, 80, 106].

Δt. At the beamline UE52-SGM at BESSY, where the experiments were carried out, the synchrotron beam can be focused only to a spot size of about 20 µm [88] (compare figure 3.5), which is much larger than the pinhole opening. So the major part of the photons impinges on the pinhole material and is lost.

The photon beam has a Gaussian profile (compare figure 3.5). But since the synchrotron beam is large compared to the pinhole diameter, the photon flux ρ_{beam}, which is the number of photons N per area F and time interval[2] Δt, can be assumed constant over the area of the pinhole:

$$\rho_{\text{beam}} = \frac{N}{F\Delta t} = \text{const.} \tag{5.2}$$

So, the photon current n_{pinhole} passing the pinhole per unit time is proportional to the aperture area F_{pinhole}

$$n_{\text{pinhole}} = \frac{N}{\Delta t} = \rho_{\text{beam}} \cdot F_{\text{pinhole}} \propto A^2, \tag{5.3}$$

where $F_{\text{pinhole}} = \pi(A/2)^2$ is the area of the pinhole. Therefore, on the one hand, the diameter should be large, to accept as many photons as possible. On the other hand, it should be as small as possible, to provide a large opening angle (see equation (5.1)) and thereby a large effective numerical aperture NA_{eff} (compare equation (4.27)). The ideal pinhole diameter represents a compromise between these contradictory requests.

In the experiments carried out in the course of this thesis, the pinhole-detector distance L was dictated by the size of the UHV chamber. So the geometrical numerical aperture $\text{NA}_{\text{geom}} = \frac{D/2}{L}$ (equation (4.22)) was fixed. The radius q of the Airy disc at a given pinhole-detector distance L as a function of the pinhole diameter A and the wavelength of the photons λ is (equation (4.25))

$$q = 1.22\frac{L \cdot \lambda}{A}. \tag{5.4}$$

If the Airy disc is larger than the detector, $2q \geq D$, then the effective numerical aperture $\text{NA}_{\text{eff}} = q/L$, equation (4.27), is larger than the geometrical one. A part of the photons is not recorded and intensity is lost. If the Airy disc is smaller than the detector, the effective numerical aperture $\text{NA}_{\text{eff}} \leq \text{NA}_{\text{geom}}$ limits the resolution, as explained in chapter 4. In an ideal case, the effective NA matches the geometrical one. Consequently, it is only necessary to expand the synchrotron beam such that it illuminates the whole detector. Then the Airy radius ideally equals half the detector width $q = D/2$, which leads to the following relation for the ideal aperture size A_{ideal} (compare equation (4.26)):

$$A_{\text{ideal}} = 2.44\frac{L \cdot \lambda}{D}. \tag{5.5}$$

[2]This time interval Δt is much larger than the synchrotron pulse length in the picosecond regime, therefore the photon current can be considered constant.

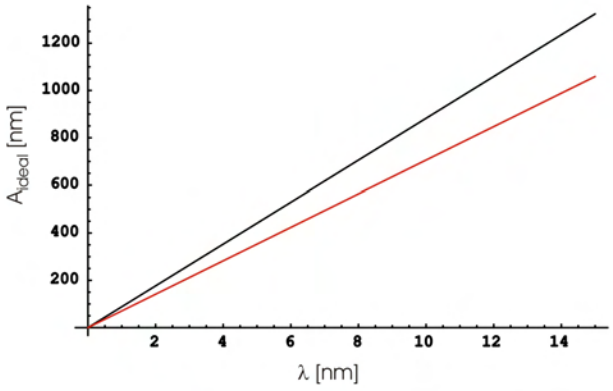

Figure 5.1: Ideal pinhole diameter versus wavelength
The ideal pinhole diameter A_{ideal} according to equation (5.5) is plotted as a function of the wavelength λ for a given pinhole-detector distance L and detector size $D = 27.6$ mm. black: $L = 1000$ mm red: $L = 800$ mm

In figure 5.1, the ideal pinhole diameter A_{ideal} is plotted as a function of the wavelength for two different pinhole-detector distances L.

In the paragraphs above, we stated, that the pinhole diameter limits the number of photons that pass the clear aperture per unit time. Another reason, why the pinhole diameter should be as large as possible, is an area argument. For a constant pinhole-detector distance L, larger opening angles of the divergent beam result in a lower photon flux on the detector[3]. The photons passing the pinhole are spread over the area of the Airy disc F_{Airy}, leading on the detector to a flux per unit area of

$$\rho_{\text{Airy}} = \frac{n_{\text{pinhole}}}{F_{\text{Airy}}}. \tag{5.6}$$

F_{Airy} is proportional to the square of the radius of the Airy disc. With equation (5.4) follows

$$\rho_{\text{Airy}} \propto \frac{n_{\text{pinhole}}}{q^2} \propto n_{\text{pinhole}} A^2. \tag{5.7}$$

Inserting equation (5.3) gives the dependence of the flux on the detector on the pinhole diameter

$$\rho_{\text{Airy}} \propto A^4. \tag{5.8}$$

This proportion emphasizes the influence of the pinhole size on the flux on the detector for a given pinhole-detector distance L and constant wavelength λ, and by that on the necessary exposure times. So the ideal pinhole is large enough to permit a photon flux as high as possible through the aperture but small enough

[3]The number of photons per detector area N/F is related to the flux ρ_{Airy} and the exposure time T via $N/F = \rho_{\text{Airy}} T$.

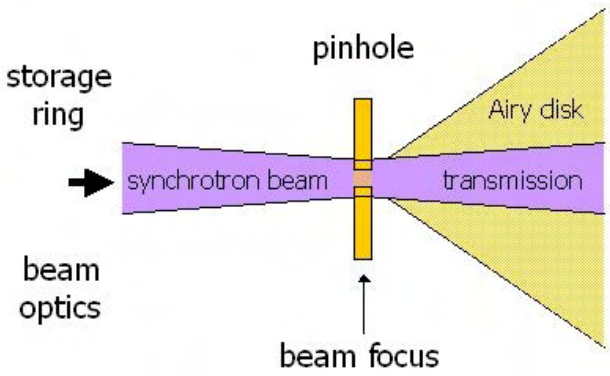

Figure 5.2: Transmission of the direct synchrotron beam
A schematic drawing of how the beam is influenced by the pinhole (not to scale)

to fully illuminate the detector in a certain pinhole-detector distance. For the wavelength range used in the presented experiments, that is from $\lambda = 2$ nm up to $\lambda = 14$ nm, and a pinhole-detector distance L of about 800 mm equation (5.5) leads to ideal pinhole diameters A of 140 nm to 1000 nm, what is also illustrated in figure 5.1.

The second important parameter regarding pinhole design is the thickness of the pinhole material. A perfect pinhole must be thick enough to block the direct synchrotron beam, that means absorb the part of the beam that impinges on the material and does not form the Airy disc. In figure 5.2, a schematic drawing illustrates how the synchrotron beam is influenced by the pinhole. The part of the beam that passes the clear aperture forms the Airy disc, while the rest penetrates the material and gets attenuated. If the pinhole material is too thin to completely absorb the X-rays, this direct transmission is visible as a bright spot on the detector. Figure 5.3, left, shows an image of an Airy disc recorded at 220 eV photon energy. A pinhole of 400 nm diameter in a 700 nm thick gold membrane was used. The transmitted beam is visible as a bright spot in the center of the image. This spot not only overlays the hologram pattern and disturbs the reconstruction but also limits the exposure time since its intensity might be orders of magnitude larger than the intensity of the Airy disc. Below the bright spot, a dark line can be seen, which appears to leak toward the lower border of the CCD chip. This effect is due to an area of destroyed pixel, where the unattenuated synchrotron beam once hit the chip, hence it will appear in all holograms recorded with that CCD camera. In figure 5.3, right, a linecut through the Airy disc is displayed. The transmitted spot can be easily identified due to it intensity that exceeds the maximum intensity of the Airy disc by a factor of 5. Consequently, the pinhole membrane has to be of a certain thickness—depending on the membrane material and the photon energy—in order to absorb the direct transmitted radiation sufficiently (compare figure 5.4).

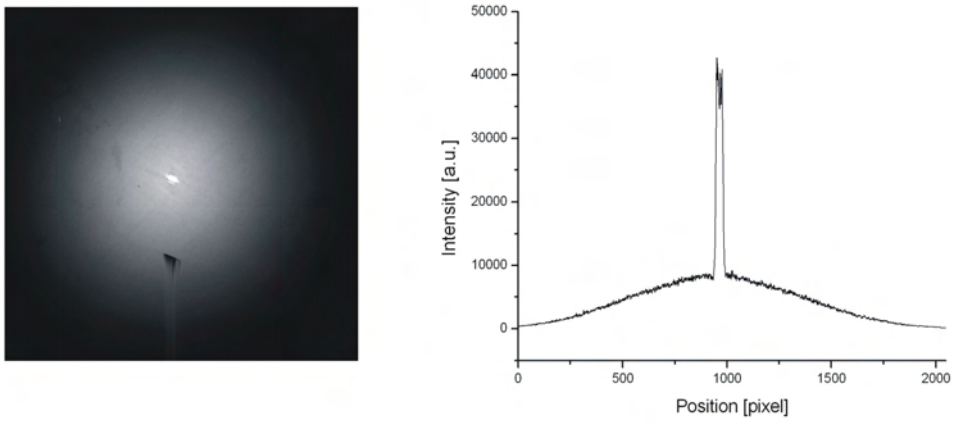

Figure 5.3: Transmission of the direct synchrotron beam
left: Image of an Airy disc with transmitted beam visible as bright spot, recorded at 220 eV, 400 nm pinhole in 700 nm thick gold foil. The size of the CCD chip is $D = 27.6$ mm.
right: Linecut through the Airy disc. The intensity of the transmitted beam is a factor 5 higher than the intensity of the Airy disc.

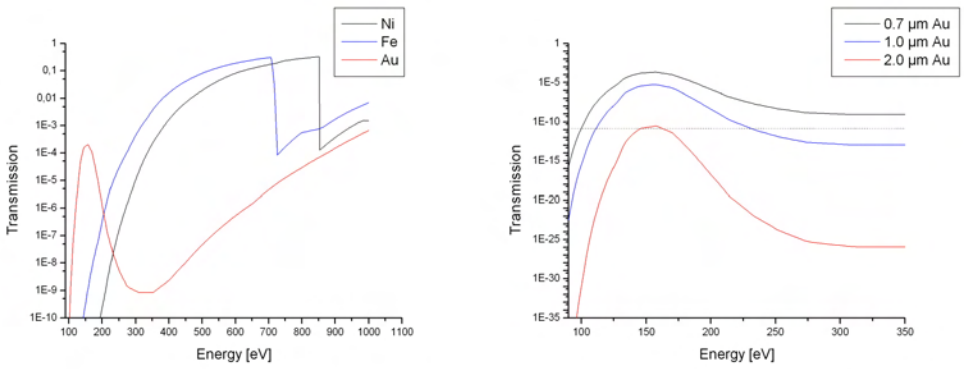

Figure 5.4: Transmission as a function of the photon energy
left: Transmission for different materials (thickness 0.7 µm)
right: Transmission through gold as a function of energy for different membrane thicknesses

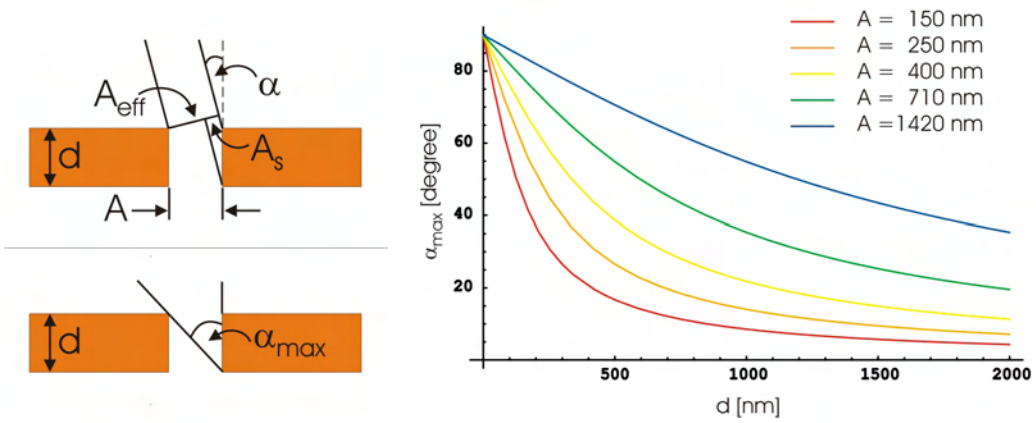

Figure 5.5: Acceptance angle of a pinhole
The maximum acceptance angle depends on the pinhole diameter A and the thickness of the membrane d.

As our experiments have shown, a gold layer of 700 nm sufficiently blocks the synchrotron beam only for energies up to 100 eV. In order to measure at higher energies, thicker membranes are needed. As figure 5.4, right, indicates, a thickness of 2 µm should suffice so that even at the maximum transmissivity of gold between 145 eV and 165 eV measurements without direct transmission are possible. For pinhole diameters of 400 nm down to 100 nm, that thickness corresponds to an aspect ratio of 1:5 to 1:20, which is a challenge concerning the fabrication.

Besides the high aspect ratio and the decreasing photon current through the pinhole, a decreasing pinhole diameter poses another experimental difficulty, namely a decrease in the maximum acceptance angle of the pinhole. If the pinhole is tilted by an angle α with respect to the optical axis given by the direction of the synchrotron beam, the effective pinhole diameter decreases. If the membrane was infinitely thin, the effective diameter would be the projected area

$$A_{\mathrm{proj}} = A \cos \alpha. \tag{5.9}$$

However, since the membrane is of finite thickness, part of the beam through this projected area impinges on the wall of the pinhole and is shadowed (compare figure 5.5). This area can be expressed as

$$A_{\mathrm{s}} = d \sin \alpha. \tag{5.10}$$

So the effective pinhole diameter is given by

$$A_{\mathrm{eff}} = A_{\mathrm{proj}} - A_{\mathrm{s}} = A \cos \alpha - d \sin \alpha. \tag{5.11}$$

The maximum permissible tilt angle α_{max} is reached, when the pinhole wall completely shadows the beam and the effective diameter is zero. α_{max} can the be

calculated as

$$\begin{aligned} & A_{\text{proj}} &=& A_{\text{s}} \\ \Leftrightarrow\quad & A\cos\alpha &=& d\sin\alpha \\ \Leftrightarrow\quad & \frac{A}{d} &=& \frac{\sin\alpha}{\cos\alpha} = \tan\alpha \\ \Leftrightarrow\quad & \alpha &=& \arctan\frac{A}{d}. \end{aligned}$$

In figure 5.5, right, the acceptance angle α_{max} is plotted as a function of the membrane thickness d for various pinhole diameters A.

5.2 Pinhole fabrication by Focused Ion Beam Milling

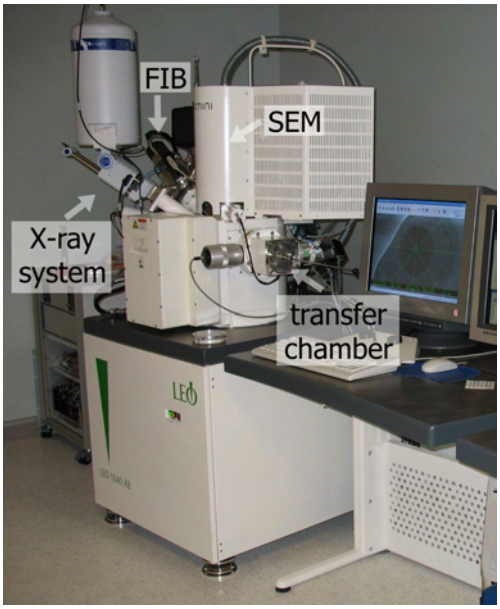

Figure 5.6: LEO 1540 CrossBeam®

Pinholes with the specifications mentioned above can be produced by Focused Ion Beam (FIB) milling. Alternative techniques to fabricate structures in the nanometer range with a high aspect ratio are Reactive Ion Etching (RIE) [70, 107], and LIGA (German acronym for "Lithographie, Galvanoformung und Abformung" = (X-ray) lithography, electroplating, and molding) [108], for example.

The LEO 1540XB CrossBeam® system from Carl Zeiss STM AG as it is available at the Nanofabrication Laboratory at the University of Western Ontario, Canada, can be used for removing, modifying, and depositing material on the nanometer scale. Positively charged gallium ions from a liquid gallium source are accelerated and focused onto the workpiece. When hitting the sample surface, material is sputtered away. This process can be accelerated with the help of etch gases like iodine or chlorine [109], which can be injected close to the surface by a multichannel gas-injection system. It is also possible to add organometallic precursors, which contain platinum or tungsten, for example. The ion beam then dissociates the precursor, and the metal is deposited on the substrate [109, 110]. Both, sputtering and deposition can be done with nanometer precision. The Ga^+-ions and secondary electrons which are produced in the sputtering process can be used for imaging. The major advantage of the

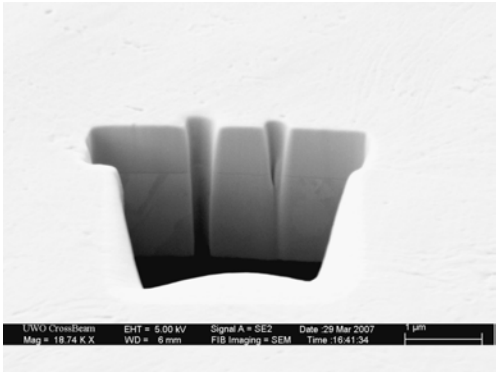

Figure 5.7: Cross section of two holes
The left hole is milled all through the membrane, while the right hole does not punch through. The tapering walls are visible in the cross section.

CrossBeam® system over other dual beam instruments is, that the milling process can be monitored in real time with a LEO GEMINI® field emission scanning electron microscope (SEM). Additionally, an Oxford Instruments X-ray system allows for elemental mapping and analysis of the milled sections. Rapid sample changes without disrupting the vacuum of the main chamber are possible because of a sample transfer airlock system.

For FIB milling, the sample has to be positioned at the coincidence point of the electron and the ion beam to make sure, that the machined spot can be live imaged with the SEM. When milling a hole, the ion beam is not just pointed statically to one spot until it has punched through. This procedure only leads to success if the membrane is sufficiently thin. For thicker membranes it results in a V-shaped crater with an aspect ratio of about 1:3 (see figure 5.7), since from a certain milling depth on, the sputtered material cannot escape from the hole but is redeposited on the walls, therefore a steady state is reached. To avoid this effect, a finite entrance hole size has to be chosen. Also, sputtering is fastest under grazing incidence due to forward scattering.

When milling holes, first, the punchthrough dose has to be determined. For this purpose, a test array is designed and drawn in the NPGS (Nanometer Pattern Generation System) lithography software. Here, the nominal hole diameter increases from left to right, while the dose increases from top to bottom (see figure 5.8, left). In order to keep one parameter fixed to facilitate the comparison of the milling results, the area dose for each hole is assigned such that the total dose is kept constant within each line. In this example, the area dose for the 200 nm hole is 10000 µC/cm^2, while for the 140 nm hole it is 20408 µC/cm^2, giving a total dose of 3 pC for each hole in the first line. A milling current of 50 pA provides a good focused beam with reasonable milling rate. Lower currents give a better focus but longer milling times. Here, the milling time for the first line was 18 s. From line to line the dose is increased by the exposure scale factor, by which the exposure time and therewith the total dose is multiplied. Once the milling is finished, the sample is flipped and SEM imaged to determine the size of the exit holes. As can be seen in figure 5.8, right, the holes in the first line,

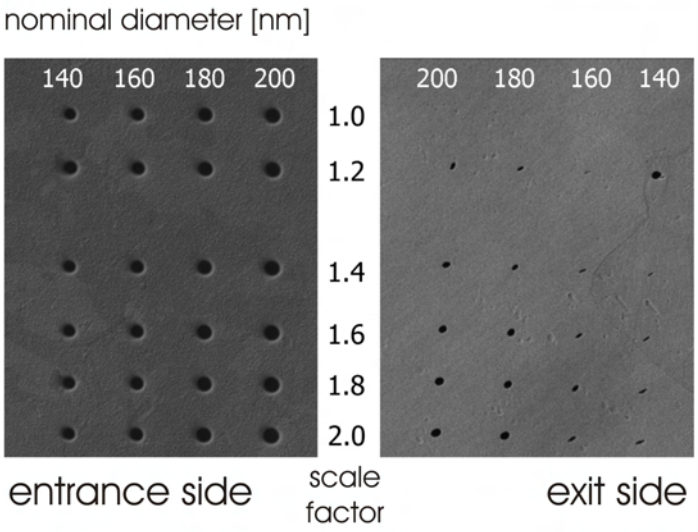

Figure 5.8: Test array to determine the punchthrough dose
left: Entrance side of gold membrane
right: Exit side of the membrane
The nominal hole diameter increases from left to right (white numbers, sizes in nm), while the total dose increases from top to bottom (scale factor in black numbers). The horizontal distance between two holes is 2 µm.

that is with the lowest dose, do not go through at all, while in the second line the holes start to open up. Also quite obvious is, that the 140 nm hole in the second line differs strongly from the rest. The reason for that is, that this hole was accidentally milled twice. The ideal diameter and dose values are such, that the hole just punches through so that the sputtered material can escape from the exit hole, but the hole is not yet widened.

Once the punchthrough values are found, the generally tapered holes are reamed open to the desired size. This procedure also leads to parallel walls. In this step, the hole is opened from inside to outside by milling circles with increasing radius (see figure 5.9, left). The last circle is written repeatedly in order to get smooth walls. Parameters that are to be varied are the radius of the first, innermost circle, which should be smaller than the initial exit hole, the radius of the outermost circle, which determines the final hole size, the step size by which the radius is increased from circle to circle (which is connected to the number of reaming circles), and the line dose. Looking at figure 5.9, right, where the line dose increases from left to right while the other parameters are kept the same, the influence of the reaming dose becomes evident. Without reaming the beam punches through the membrane as expected, but if the line dose is chosen to small, material is redeposited and the hole is filled up as in the second hole from the left. Therefore, a higher line dose is needed. It is also useful to keep in

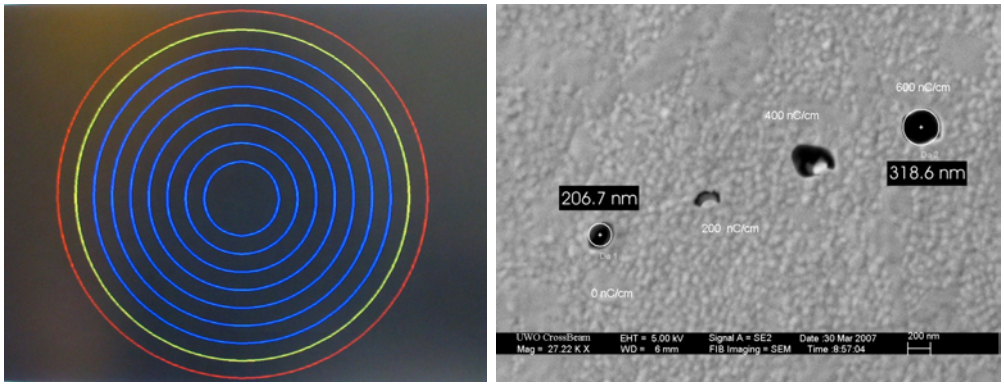

Figure 5.9: Testing the reaming parameters
left: Reaming pattern
First, the beam has to punch through the membrane (red circle), then the hole is opened up from inside to outside (blue circles) to the final diameter. The last reaming radius (yellow circle) is written repeatedly for polishing.
right: Exit side of reaming test array
This image was taken by Dr. Todd Simpson. The white numbers give the assigned line dose. The diameter of the first and the last exit hole are measured.

mind, that gravity has no influence on such tiny structures. A piece of material attached to the wall as in the third hole would not 'fall to the ground' when cut loose but would still stick to the membrane due to van-der-Waals forces acting on those length scales.

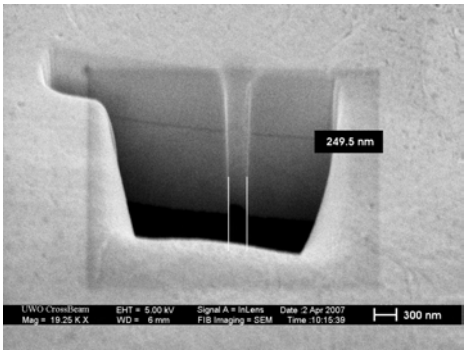

Figure 5.10: Cross section of a milled hole
The diameter is measured to be $A = 250$ nm.

The holes can be analyzed either by turning the sample over and measuring the size of the exit holes as done in figure 5.8, or by cutting open a rectangular section of the membrane, so that the cross section of the milled hole becomes visible (compare figure 5.10). This also allows to examine whether the walls are parallel or tapered.

When the milling parameters are found, the hole sizes reproduce, and pinholes with diameters of 450 nm, 320 nm and 250 nm in 2 µm thick gold have been produced. Smaller hole diameters are not feasible in such thick membranes because of the high aspect ratio. In order to be able to access shorter wavelengths on the cost of transmitted intensity, a pinhole of 150 nm in size has been milled in a 700 nm membrane. This pinhole fully illuminates the detector in a distance $L = 800$ mm for wavelengths down to $\lambda = 2.1$ nm, what corresponds to photon energies of $E = 583.6$ eV.

5.3 Pinhole generations

One major aim of this thesis was the adaptation of the pinhole design to meet the requirements mentioned above for the use in digital X-ray holography. In this process, three different types of pinholes were tested and used for the measurements presented in this thesis. These different types are introduced in the following.

5.3.1 Commercial pinholes

The first generation of pinholes were commercially available pinholes purchased from National Apertures, Inc. These apertures consist of a stainless steel backing of 127 µm thickness on which a 2.5 µm thick nickel foil is attached. Into this foil the final pinhole is laser drilled. Pinholes with two different nominal diameters were used: $A = 1$ µm and $A = 0.5$ µm. Scanning Electron Microscopy (SEM) images as shown in figures 5.11 and 5.12 reveal the actual diameter being $A = 1.22 \pm 0.06$ µm and $A = 0.74 \pm 0.07$ µm.

Although those pinholes are large compared to the wavelength of soft X-ray photons of few nanometers, they produce reasonably divergent beams and sufficiently illuminate the detector for photon energies of 90 eV and up to 140 eV respectively. Also, they are a good compromise between spatial resolution and photon intensity.

The diameter A of the aperture can also be determined via the radius of the Airy disc q on the detector (see figure 5.11 and 5.12) at pinhole-detector distance L for a given wavelength λ (compare equation (2.55) and (4.25)):

$$A = 1.22 \frac{L \cdot \lambda}{q}. \tag{5.12}$$

In that way, after measuring the Airy disk on the detector (see figure 5.11 and 5.12) the actual pinhole size was calculated to be $A = 1.42 \pm 0.04$ µm, which is only slightly larger than the value above, and $A = 0.71 \pm 0.06$ µm. This small difference is due to the fact that scanning electron microscopy is a surface sensitive method, so the information about the cross section of the pinhole within the membrane is limited. Thus, the value determined via the diameter of the Airy disc on the detector is the relevant one for the experiments, since it expresses the effective diameter for the X-ray beam.

As can be seen in figure 5.11 and 5.12, the nickel foil does not block the direct synchrotron beam completely, as a bright spot is visible in the images, which were recorded at $E = 90$ eV and $E = 140$ eV, respectively. This spot limits the exposure times and must be numerically suppressed in order not to disturb the

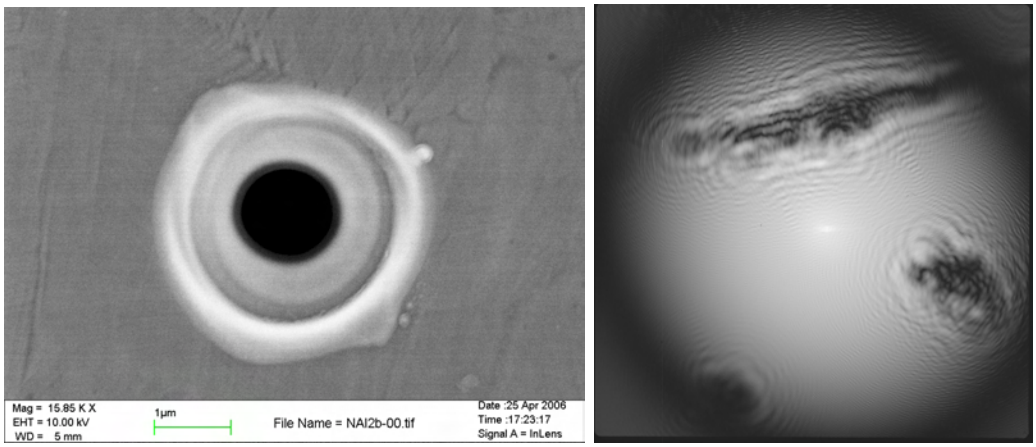

Figure 5.11: Commercial pinhole with 1.0 µm diameter
left: SEM image of a commercial pinhole showing an actual diameter of $A = 1.22 \pm 0.06$ µm.
right: Hologram of a cell sample recorded at $E = 90$ eV in a pinhole-detector distance of $L = 100$ cm with a CCD chip $D = 2.76$ cm in size. The intensity is in a logarithmic scale. The radius of the underlying Airy disc gives a pinhole diameter of $A = 1.42 \pm 0.04$ µm.

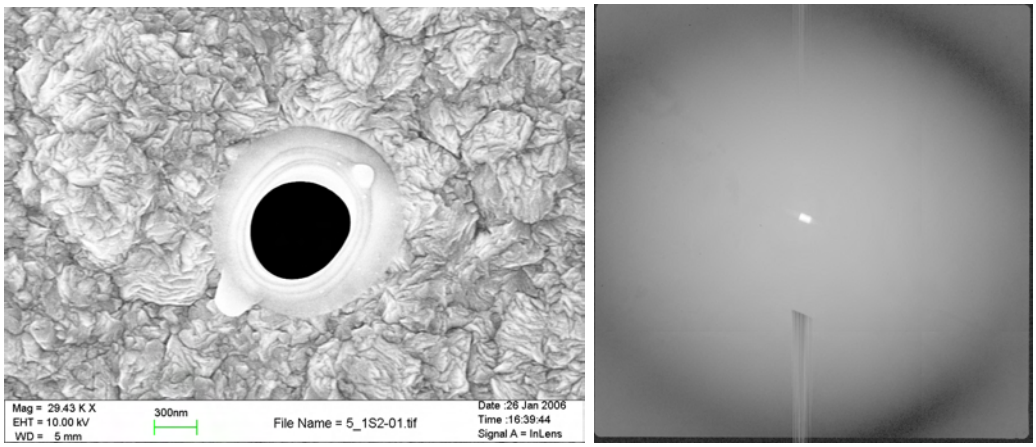

Figure 5.12: Commercial pinhole with 0.5 µm diameter
left: SEM image of a commercial pinhole showing an actual diameter of $A = 0.74 \pm 0.07$ µm.
right: Airy disc recorded at $E = 140$ eV in a pinhole-detector distance of $L = 80$ cm with a CCD chip $D = 2.76$ cm in size. The intensity is in a logarithmic scale. The radius of the Airy disc gives a pinhole diameter of $A = 0.71 \pm 0.06$ µm.

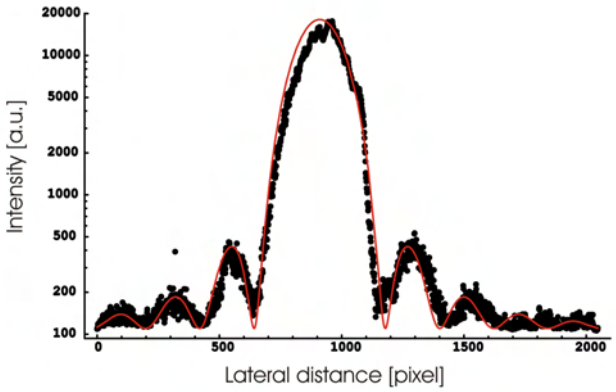

Figure 5.13: Determination of pinhole diameter via Airy pattern
A linecut across the intensity distribution on the detector (black dots) is fitted with an Airy distribution (red curve), and the pinhole diameter A is determined through the fit parameter k. In this case, the photon energy was $E = 287$ eV, and $k = 1/70$ pixel. With a pinhole-detector distance $L = 1000$ mm this leads to $A = 1.45$ µm.

reconstruction. In figure 5.12, the effect of the destroyed pixels is visible. It does not appear in figure 5.11, since this image was recorded earlier.

Instead of considering only the radius of the Airy disc, a linecut across the whole detector can be fitted with the theoretical Airy intensity distribution (compare equation 2.55 and figure 5.13)

$$I(x) = I_0 \left[\frac{J_1\left(\frac{\pi A}{\lambda L} x\right)}{\frac{\pi A}{\lambda L} x} \right]^2 = I_0 \left[\frac{J_1(kx)}{kx} \right]^2 . \tag{5.13}$$

From the fit parameter k the pinhole diameter A can be calculated for known wavelength λ and pinhole-detector distance L. The results gained via this method confirmed the values found via the determination of the Airy radius on the detector.

5.3.2 Pinholes in thin gold membranes

In order to access higher photon energies, especially the carbon K-edge at 284.2 eV [111], and improve the spatial resolution, smaller pinholes were designed. The principal concept was maintained: The backing consists of a stainless steel disc of 50 µm thickness and 10 mm diameter with a hole of 1.5 mm, manufactured at the mechanical workshop of the Department for Physical Chemistry at the University of Heidelberg. A metal foil is glued onto this backing. In this case, gold leaf was chosen, since the final pinhole is fabricated by FIB milling, and gold shows very

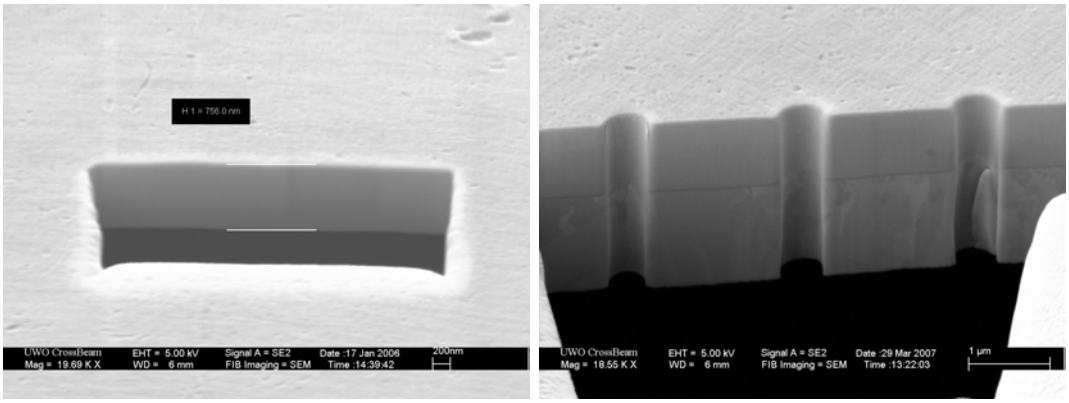

Figure 5.14: Thickness of the gold foil

A rectangle was cut into the gold foil by FIB milling to get a cross section of the membrane. Now the thickness of the membrane can be determined. In this way, the thickness of the membrane was determined to be $d = 0.804 \pm 0.036$ µm (thin gold membrane, left) and $d = 2.01 \pm 0.08$ µm (thick gold membrane, right). The images were taken by Dr. Todd Simpson from the Nanofabrication Laboratory at the University of Western Ontario, Canada.

good sputtering behavior. Additionally, the attenuation length of gold in the envisaged energy range is satisfying. The gold foil was purchased from Friedrich Busse Blattgoldfabrik GmbH+Co. KG, Schwabach, Germany, and has a purity of 24 carat (99.9%).

The thickness of the foil was determined via the weight of the sheets to $d = 0.677 \pm 0.048$ µm, direct measurement with a SEM resulted in $d = 0.804 \pm 0.036$ µm (compare figure 5.14, left). Into this membrane a pinhole of diameter $A = 400$ nm was FIB milled by Dr. Todd Simpson from the Nanofabrication Laboratory, University of Western Ontario, Canada. The size of the Airy disc confirms an aperture of $A = 410 \pm 30$ nm. With this pinhole reconstructable holograms were recorded in an energy range from 90 eV up to 330 eV. However, a direct transmission was present at energies higher than 100 eV, as can be seen in figure 5.15.

5.3.3 Pinholes in thick gold membranes

As our experiments have shown, a gold layer of 700 nm sufficiently blocks the synchrotron beam only for energies up to 100 eV. In order to measure at higher energies without direct transmission, thicker membranes are needed. As figure 5.4, right, indicates, a thickness of 2 µm should suffice so that even at the maximum transmissivity of gold between 145 eV and 165 eV the intensity of the direct beam is attenuated to the level of the Airy disc and measurements without a transmitted spot are possible. For pinhole diameters of 400 down to 100 nm,

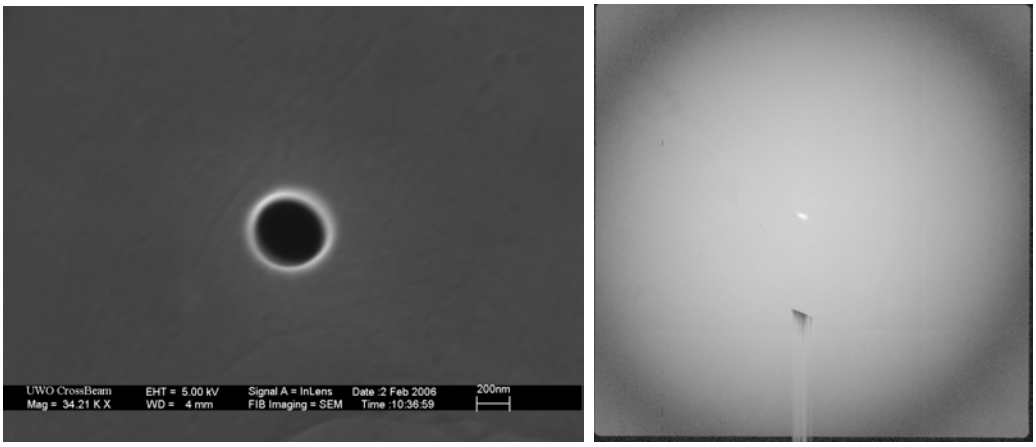

Figure 5.15: Pinhole in thin gold membrane with 0.4 µm diameter
left: SEM image of a FIB milled pinhole showing an actual diameter of $A = 0.39 \pm 0.01$ µm.
right: Airy disc recorded at $E = 220$ eV in a pinhole-detector distance of $L = 80$ cm with a CCD chip $D = 2.76$ cm in size. The intensity is in a logarithmic scale. The radius of the Airy disc gives a pinhole diameter of $A = 0.41 \pm 0.03$ µm.

that thickness means an aspect ratio of 1:5 to 1:20. The fabrication of these pinholes was described in chapter 5.2. Such pinholes were produced during a three weeks stay at the Nanofabrication Laboratory at the University of Western Ontario, Canada.

Like the pinholes mentioned above, the membrane of the third generation pinholes consists of a 700 nm thick foil of gold leaf which is glued onto the stainless steel backing material with Crystalbond™. This time, after cleaning the gold surface under UV light for one hour, an additional layer of approximately 1.3 µm gold is vapor-deposited on the foil, leading to a total thickness of 2 µm. By milling open a rectangle and taking an image with the SEM as depicted in figure 5.14, right, the structure of the membrane becomes visible—the transition between the gold layers is imaged as a dark line—and the thickness of the gold can be determined. In this way, the total membrane thickness of $d = 2.01 \pm 0.08$ µm could be confirmed.

In this gold layer, a pinhole with diameter $A = 250$ nm was milled by Focused Ion Beam. As figure 5.16 shows, the diameter could be confirmed with SEM measurements, which give $A = 254 \pm 20$ nm. The determination of the pinhole diameter via the size of the Airy disc on the detector gives a maximum value of $A = 220 \pm 4$ nm. This value might not be very reliable, because finding the position of the Airy minimum was not straightforward, since the intensity minimum was not well-pronounced. The Airy disc in figure 5.16 is elliptical, a fact that suggests, that the pinhole is tilted with respect to the beam, leading

Type	*commercial*		*FIB milled*	
Name	NAI1.0	NAI0.5	TB3L	T2
Size				
nominal	1.0 µm	0.5 µm	0.4 µm	0.25 µm
SEM	1.22 ± 0.06 µm	0.74 ± 0.07 µm	0.39 ± 0.01 µm	0.25 ± 0.02 µm
Airy	1.42 ± 0.04 µm	0.71 ± 0.06 µm	0.41 ± 0.03 µm	0.220 ± 0.004 µm
Membrane	*Ni*		*Au*	
Thickness	2.5 µm	2.5 µm	0.7 µm	2.0 µm
Energy range	90 eV	90 to 140 eV	90 to 330 eV	220 to 500 eV
theoretical Resolution				
δ_{eff}	0.70 µm	0.37 µm	0.20 µm	0.11 µm
δ_{Kreuzer}	1.15 µm	0.61 µm	0.33 µm	0.18 µm

Table 5.1: Overview over pinhole types
The nominal and experimental sizes, the accessible energy range as well as the theoretical resolution as discussed in chapter 4 are listed.

to an effective pinhole diameter smaller than the actual one. Despite of that, measurements with photon energies up to $E = 500$ eV were possible. As can be seen in figure 5.17, the membrane is thick enough to attenuate the transmitted synchrotron beam such that its intensity is in the order of the intensity of the Airy disc.

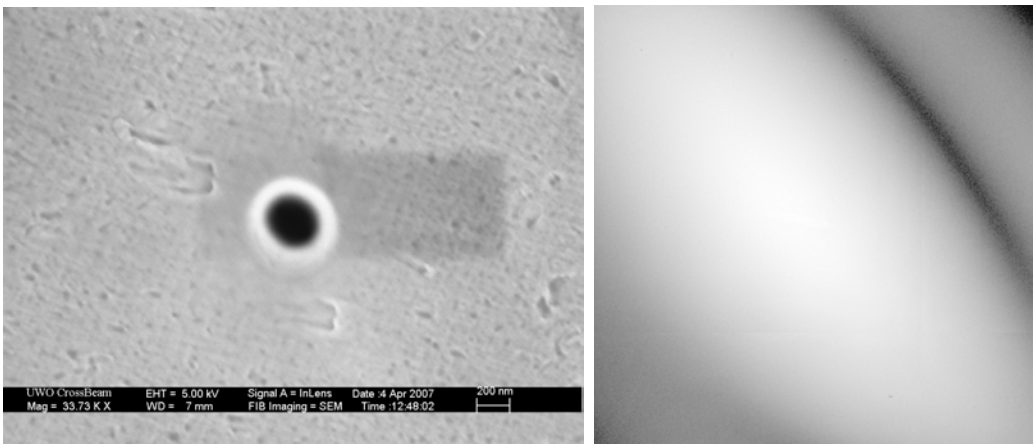

Figure 5.16: Pinhole in thick gold membrane with 0.25 µm diameter
left: SEM image of a FIB milled pinhole showing an actual diameter of $A = 0.25 \pm 0.02$ µm.
right: Airy disc recorded at $E = 500$ eV in a pinhole-detector distance of $L = 82$ cm with a CCD chip $D = 2.76$ cm in size. The intensity is in a logarithmic scale. The smallest radius of the Airy disc gives a maximum pinhole diameter of $A = 0.220 \pm 0.004$ µm.

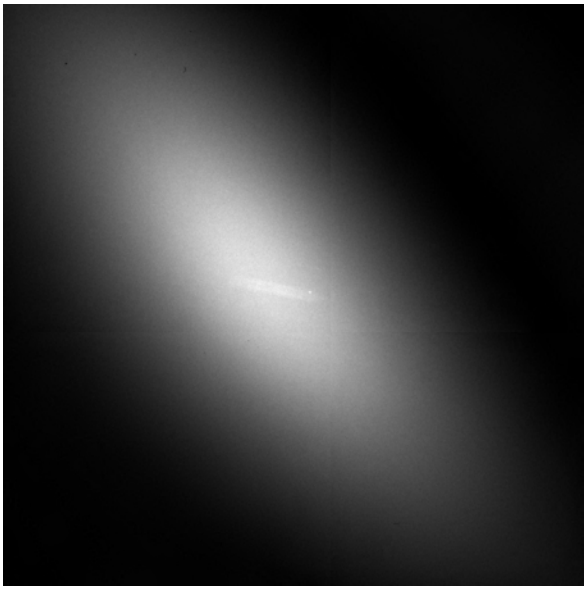

Figure 5.17: Airy disc of a pinhole in thick gold membrane with 0.25µm diameter
Airy disc recorded at $E = 500$ eV in a pinhole-detector distance of $L = 82$ cm with a CCD chip $D = 2.76$ cm in size. The intensity is in a linear scale. The intensity of the transmitted beam is attenuated to the level of the Airy disc.

6 Samples

To evaluate the contrast and resolution properties of digital in-line X-ray holographic microscopy (DIXH), different sample types were used. Lithographic structures, particle mixtures, and biological cells consist of different materials and contain structures with sizes ranging from several micrometers down to a few nanometers. All samples are prepared on 100 nm thin Si_3N_4 membrane windows with a window size of 1 mm^2 purchased from Silson Ltd., Northampton.

6.1 Lithography structures

For electron beam lithography, SU-8 2025 negative tone photo resist by Micro Chem was spin coated on a Si_3N_4 window in a Spin Coater (TT200-8, LP-Thermtech, Volkertshausen) at 4000 rpm to achieve a film thickness of 700 nm. In order to evaporate the solvent and compact the film, the substrate was first soft baked on a level hot plate at 65°C and 95°C for 1 min at each temperature. Structures with different line widths were written with a scanning electron microscope (SEM, LEO 1530 with a Raith Elphy Quantum lithography unit) at an area dose of 25 µC/cm^2. The structures consisted of dots and lines (compare figure 6.1). An irregular pattern was chosen, since periodic structures might cause strong artifacts during the Fourier transformation in the reconstruction algorithm. The maximal width of the lines was 1.5 µm, with some of the lines tapered toward one end to check the sensitivity of the technique toward structural sizes below the resolution limit. Subsequently, the sample was post exposure baked on a hot plate to selectively cross-link the exposed film at 65°C and 95°C for 2 min each before developing it by immersion in SU-8 developer by Micro Chem for 1.5 min. The structures were produced by Martina Schürmann (Angewandte Physikalische Chemie, Universität Heidelberg). A detailed description of the process can be found in her PhD thesis [112].

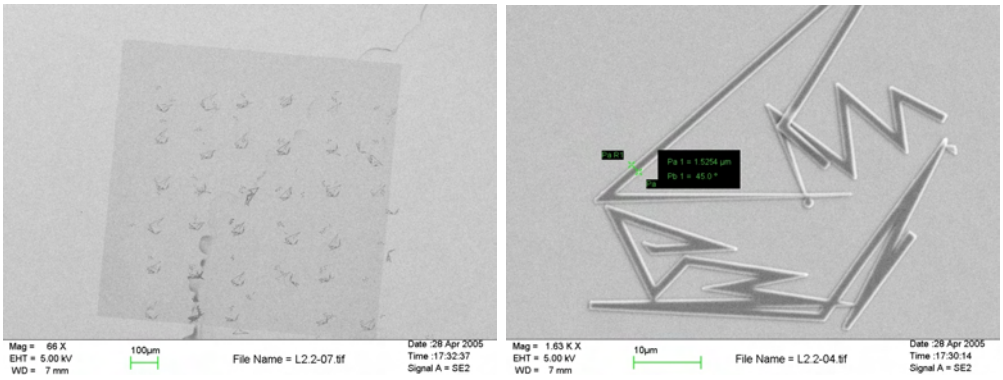

Figure 6.1: Lithography structures in SU-8
left: Array of random structures imaged with the SEM (Leo 1530). The Si_3N_4 membrane appears as a darker square.
right: Close-up view of a structure. The line width is 1.5 µm, some lines are tapered toward the end.

6.2 Mixtures of polystyrene beads and magnetic pigment

For the preparation of particle mixtures on the Si_3N_4-surface, first a droplet of magnetic pigment (Magnetpigment 025 BASF, average particle size: 4-6 µm) was suspended in distilled water and dispersed onto the membrane. After evaporation of the water, a second droplet with polystyrene beads (Polystyrene micro spheres, Polysciences) was added and the sample subsequently air-dried. The concentration of both particle types was chosen such that a sub-monolayer coverage was obtained.

For the polystyrene particles, two different sizes were employed. Since the diameter of the magnetic pigment was stated to be 4-6 µm, polystyrene particles of size 6 µm (10% variance) were chosen for the mixture to match the size of these iron oxide particles. However, optical microscopy as well as SEM images showed that the iron oxide pigment exhibits a rather broad size and shape distribution with the largest particles having a diameter of only about 2 µm (compare figure 6.2, left). Therefore, for the second set of bead samples polystyrene beads with diameter of 2.2 µm ± 0.1 µm were chosen (compare figure 6.2, right).

6.3 Biological cells

Apart from the obvious biological interest in imaging cells—preferably in situ or cryo-fixed—the capability of DIXH to image biological samples and the sensitivity of the technique to resolve small structures inside these extended objects was

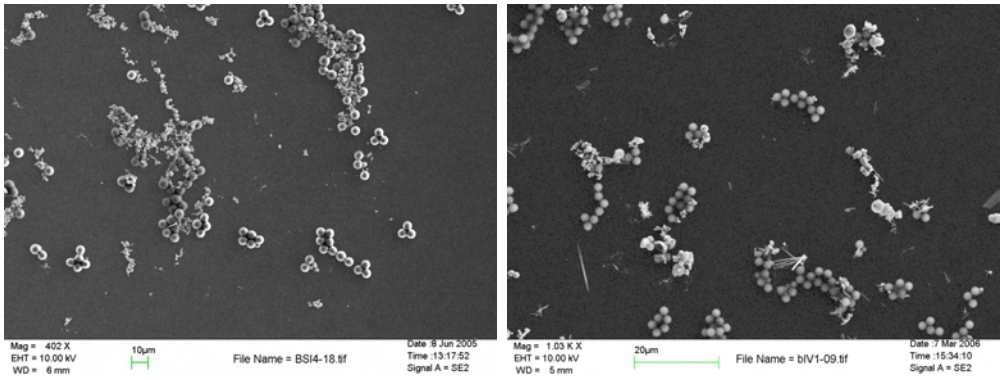

Figure 6.2: Mixture of polystyrene beads and magnetic pigment
The uniform round objects are polystyrene particles, while the iron oxide pigments show a broad distribution in size and shape. (SEM Leo 1530)
left: The polystyrene beads in the particle mixture have a diameter of 6 µm.
right: To match the size of the largest iron oxide particles, polystyrene beads of 2.2 µm in size were used in the second bead sample.

tested. Another goal was to better understand the wavelength dependent material contrast properties, which differ for X-rays compared to light microscopy. The following biological samples were used.

6.3.1 Rat embryonic fibroblasts

Rat embryonic fibroblast (REF 52WT) cells are cultivated on fibronectin coated Si_3N_4 membranes for 24 h in Dulbecco's Modified Eagle's Medium (DMEM) supplemented with 10% Fetal Bovine Serum (FBS), all purchased at Gibco. After rinsing with Phosphate Buffered Saline (PBS), the cell structure is fixated in glutaraldehyde (4% in PBS) for 30 min at room temperature. To avoid damage to the delicate structures inside the cell arising due to surface tension during evaporation of the water, the cell water is slowly exchanged against ethanol by six different ethanol/water concentrations (50%/50%, 60%/40%, 70%/30%, 80%/20%, 90%/10%, and 100%/0%, where the last step is repeated twice). Finally, the cells are critical point dried (Bal-Tec CPD 020)[113]. During this procedure, the ethanol is exchanged stepwise by liquid CO_2 under high pressure and low temperature. Then, the CO_2 is heated such that temperature and pressure exceed the critical point, and the liquid and the gaseous phase coexist without undergoing a phase transition. The now gaseous CO_2 can be released slowly through a valve and the sample is dried. These samples were prepared by Xinyu Cao (Angewandte Physikalische Chemie, Universität Heidelberg).

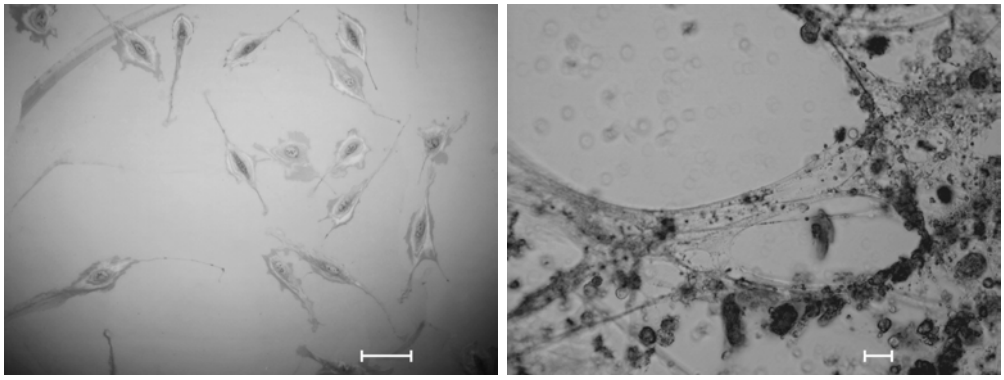

Figure 6.3: Biological cell samples cultivated on Si_3N_4 membranes
left: Critical point dried Rat Embryonic Fibroblasts. The scale bar is 100 µm long. Zeiss Axioplan2, $40\times$ Neofluar, NA0.75
right: Undifferentiated Mesenchymal Stromal Cells. Here, the scale bar is only 10 µm long. Zeiss Axiovert 200M, $40\times$ Plan-Neofluar, NA 0.75

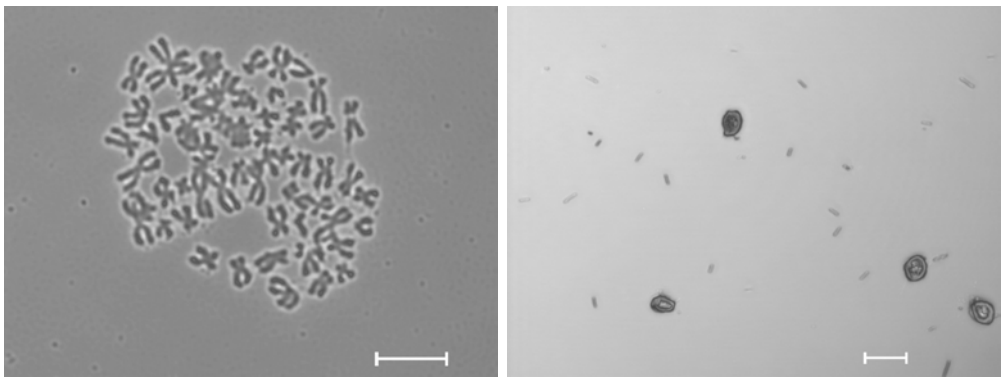

Figure 6.4: Biological samples on Si_3N_4 membranes
left: Chromosome spread of HeLa cells. Zeiss Axiovert 200M, $40\times$ Plan-Neofluar, NA 0.75
right: Spores of the green alga *Ulva linza* settled on a membrane. Zeiss Axiovert 200M, $40\times$ Plan-Neofluar, NA 0.75
The scale bars indicate 10 µm in both pictures.

6.3.2 Mesenchymal Stromal Cells

Mesenchymal Stromal Cells (MSCs) are undifferentiated connective tissue cells extracted from human bone marrow. External stimuli promote their differentiation into osteoblasts (cells responsible for bone formation), chondrocytes (they produce and maintain the cartilaginous matrix), myocytes (muscle fibers), and adipocytes (fat cells) [114]. Like the above mentioned fibroblasts, the undifferentiated MSCs are cultivated on Si_3N_4 membranes and fixated in Trifluoroacetic Acid (TFA) for 10 min at room temperature. After dehydration via the ethanol series, the samples are critical point dried. The cells were cultivated by Dr. Rainer Saffrich at the Universitätsklinikum Heidelberg, Heidelberg. The drying process was done by Xinyu Cao.

6.3.3 HeLa cell chromosome spreads

HeLa TK- cells (human epithelial cell line derived from a cervix carcinoma, thymidine kinase-deficient) are cultivated in Eagle's Minimal Essential Medium (EMEM) supplemented with 10% Fetal Bovine Serum (FBS), 5% Glutamine, penicillin, and streptomycin at 37°C and 5% CO_2 for 24 hours. Afterwards, colcemid is added to inactivate the spindle fibre mechanism and arrest the cells in metaphase. After incubation for 2 hours and washing with PBS, Trypsin-EDTA is added to detach the cells from the flask. The Trypsin-EDTA is exchanged by EMEM, and the suspension is centrifuged at 1000 g for 10 min. Now, the EMEM is replaced by a hypotonic solution (35 mM KCl in HEPES) and the resuspended cells are put in the incubator for 30 min, where they swell due to the osmotic pressure. Then follows another centrifugation step, after which the cells form a pellet and the solution can be extracted completely. The pellet is slowly resuspended in fixation buffer (methanol:pure acetic acid as 3:1 at -20°C), and the last two steps are repeated. Last, a droplet of 10 µl of the suspension is dropped with a pipette from about 10 cm distance onto a Si_3N_4 membrane where some of the swollen cells burst and the chromosomes spread. Finally, the membranes are air dried. The detailed cultivation protocol can be found in the forthcoming PhD thesis of Zuhal Kaya (Anorganisch-Chemisches Institut, Universität Heidelberg) [115], who prepared these samples.

6.3.4 Ulva linza spores

Commonly known as sea lettuce, the green algae *Ulva linza* lives primarily in marine environment and is one of the organisms responsible for biofouling of surfaces. For reproduction, the alga releases its spores, either quadriflagellated zoospores, which settle on surfaces like rocks or ship hulls and form new plants, or biflagellated gametes [116]. Since the gametes are positively phototactic and

swim toward the light source and the zoospores are negatively phototactic and swim towards darker regions, the two types can be separated. For our samples, droplets of artificial sea water with zoospores are applied onto the Si_3N_4 windows, these are left in a dark environment for 45 minutes, and the algae settle on the membrane. Then, the algae are fixated with glutaraldehyde, and the salt water is slowly exchanged with distilled water. The following dehydration is done via an ethanol series, completed by critical point drying. The samples were obtained from Dr. Michala Pettitt from the University of Birmingham, Birmingham, UK, and critical point dried by Christof Christophis (Angewandte Physikalische Chemie, Universität Heidelberg).

7 Experiments with vacuum-ultraviolet radiation and determination of the achieved resolution

The following chapter deals with the proof of principle experiments carried out during the first beamtime and how the achieved resolution can be determined in the reconstructed images.

To test the applicability of in-line holography to X-rays, proof of principle experiments with lithography structures, particle mixtures, and biological cells (REFs) were performed in the vacuum-ultraviolet (VUV) region. These samples were prepared as described in chapter 6. For all experiments presented in this chapter the setup was identical. Commercial pinholes of a nominal size of 1.0 µm were chosen to form the divergent beam since they allow relatively high photon flux but are small enough to completely illuminate the detector at energies up to 110 eV. As already discussed in chapter 5.3, the recorded Airy discs as well as SEM images showed a real pinhole diameter of $A = 1.42 \pm 0.04$ µm and $A = 1.22 \pm 0.06$ µm, respectively. The sample was mounted 10 mm downstream of the pinhole on the same manipulator, the distance to the detector was $L = 1000$ mm. With these parameters, the numerical aperture is limited by the size of the Airy disc on the detector, what leads with equation (4.28) to a theoretical resolution $\delta_{\text{eff}} = 0.70$ µm. The resolution in analogy to the Abbe limit (equation (4.66)) is then $\delta_{\text{Kreuzer}} = 1.15$ µm.

7.1 Lithographic structures

The first test was performed with lithographic structures as well defined test samples. Figure 7.1 (a), shows a hologram of the structure recorded at a photon energy of 90 eV ($\lambda = 13.8$ nm). Five single exposures were added up to improve the photon statistics, the total acquisition time was $T = 2000$ s. The first minimum of the Airy distribution can be seen as a dark oval near the borders of the CCD chip, confirming sufficient divergence of the reference wave. Also,

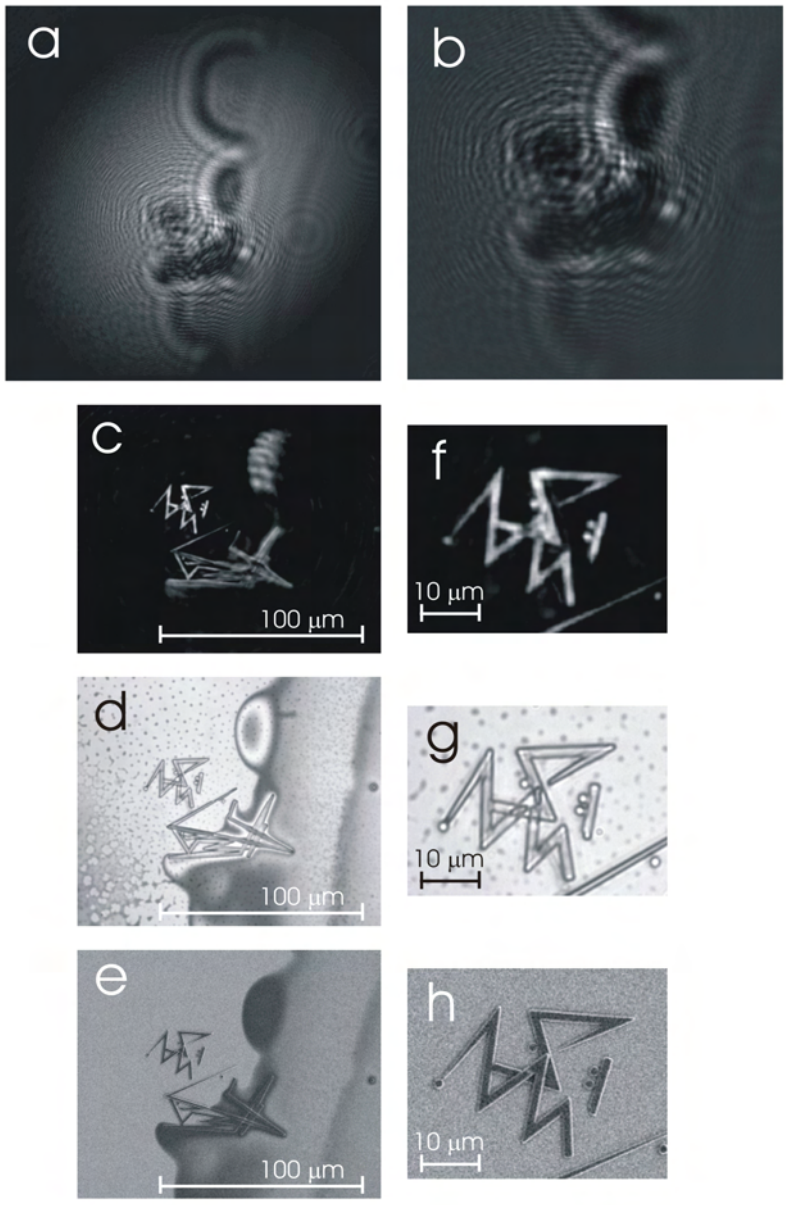

Figure 7.1: Lithographic structures in photoresist
(a): Hologram recorded at $E = 90$ eV. The first minimum of the Airy pattern can be seen as dark oval. The interference fringes are well pronounced.
(b): Difference hologram of (a). Subtraction of the Airy pattern leads to a flat background intensity.
(c): Reconstruction of (b). The photoresist structures are well resolved.
(d): Optical microscopy image. Zeiss Axioplan2, $40\times$ Neofluar, NA 0.75
(e): Scanning electron microscopy image. Leo 1530
(f) to (h): Magnified region of interest of (c) to (e).

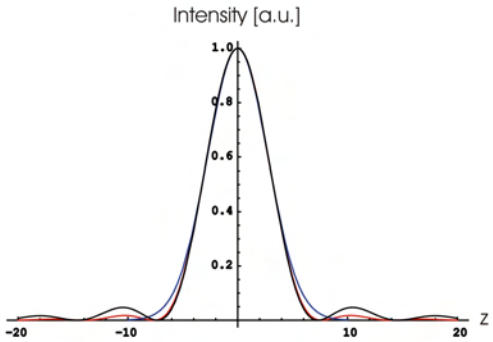

Figure 7.2: Comparison of Point Spread Functions
The intensity distribution behind a rectangular slit (black) and the diffraction pattern from a circular aperture (red) are compared to a Gaussian function (blue).

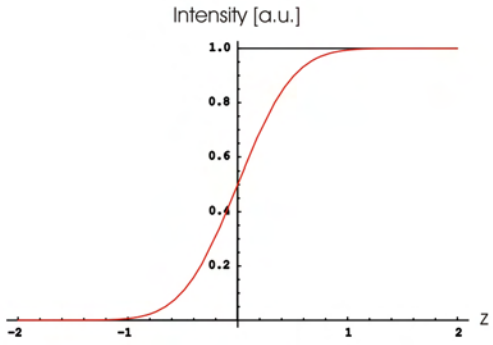

Figure 7.3: Knife-edge criterion
A perfect knife-edge function (step-function, black) and a broadened edge (red), gained through a convolution with a Gaussian function with variance $\sigma = 0.4$.

the interference pattern shows well resolved, pronounced fringes. This indicates adequate coherence of the synchrotron radiation as well as enough material to provide good contrast. The spot due to direct transmission in the center of the image is barely brighter than the maximum of the Airy pattern, which means that the nickel foil is thick enough to block the direct VUV synchrotron beam.

The difference hologram (after subtraction of the source image, compare equation (2.72)) is depicted in figure 7.1 (b), image (c) shows the corresponding reconstruction. The reconstructed structures slightly left of the center are well resolved while the ones on the lower right seem blurred. A comparison with an optical microscopy image (d) and a SEM image (e) of the same field of view reveals that the apparent smearing is real and due to a resist drop edge across the lithographic structure. Taking a closer look at the part of the structure, which is not influenced by the drop, it can be seen in figures (f) to (h) that all details are reproduced in the reconstruction. Even the tapered lines, where the line width is smaller than the theoretical resolution of $\delta_{\text{eff}} = 0.70$ µm, are completely visible.

Assuming the structures have a rectangular cross section, the achieved resolution can be determined via the so called knife-edge criterion. Here, a linecut across the edge of the structure is taken in the image and the width over which the intensity rises from 10% to 90% gives the resolution δ_{edge} [6, 35, 52]. In an ideal case, the edge is an infinitely steep step function and the resolution limit goes towards zero.

In reality, the transition is broadened in the image by the diffraction-limited point spread function (PSF) of the imaging system. So the image wave is described by the convolution of the object wave with the point spread function of the system [70], and the resolution of the system is limited by the resolution of the point spread function.

As already stated in chapter 2.2, for a single rectangular slit with width A illuminated with a wavelength λ and observed in a distance L, the intensity distribution of this PSF varies with the position x on the screen as [69, 80] (compare equation (2.43))

$$I(x) = I_0 \left[\frac{\sin\left(\frac{\pi A}{\lambda} \sin\frac{x}{L}\right)}{\left(\frac{\pi A}{\lambda} \sin\frac{x}{L}\right)} \right]^2 \approx I_0 \left[\frac{\sin\left(\frac{\pi A}{\lambda} \frac{x}{L}\right)}{\left(\frac{\pi A}{\lambda} \frac{x}{L}\right)} \right]^2 = I_0 \,\mathrm{sinc}^2\left(\frac{Ax}{\lambda L}\right). \tag{7.1}$$

Here, I_0 is the peak intensity. In the case of a circular aperture of diameter A, the PSF changes to the Airy distribution (compare equation (2.55))

$$I(r) = I_0 \left[\frac{2\, J_1\left(\frac{\pi A r}{\lambda L}\right)}{\frac{\pi A r}{\lambda L}} \right]^2, \tag{7.2}$$

where $J_1(z)$ is the Bessel function of order 1 and r is the radial distance to the optical axis [69]. Both distributions can be approximated by a Gaussian function, as illustrated in figure 7.2, what will be done in the following analysis for practical purposes.

In numerical simulations a theoretical knife-edge, represented by a step-function, was convoluted with a Gaussian function with variance σ. The result is illustrated in figure 7.3. The resolution δ_{edge}, given by the finite width of the intensity rise, was found to be 8.8% larger than the corresponding resolution determined by the variance of the gaussian $\delta_{\mathrm{gauss}} = \sqrt{8 \ln 2}\,\sigma$. However, this deviation should be in the range or smaller than the experimental errors and therefore negligible.

Analyzing the linecuts of the reconstruction displayed in figure 7.4 with this criterion results in $\delta_{\mathrm{edge}} = 1.13 \pm 0.35$ µm. This value is larger than the theoretical effective resolution of $\delta_{\mathrm{eff}} = 0.70$ µm but matches the Kreuzer-resolution $\delta_{\mathrm{Kreuzer}} = 1.15$ µm [32]. Mechanical or thermal drift is not a resolution limiting factor in this setup, since the sample is fixed relative to the pinhole. A lateral translation of the pinhole/sample manipulator results in a shift of the scattering pattern by the same distance on the CCD detector. So drift only leads to changes in the recorded image if the drifted distance is larger than the pixel size, which is in our case 13.5 µm. Even more, a linecut in the recorded hologram as displayed in figure 7.5 reveals that the fringe to fringe spacing of the smallest fringes is about 10 pixels. Since the fringes are leveled out if the drift is of the order of the fringe spacing, it is only a limiting factor if it is larger than 135 µm. Therefore, these holograms can be considered drift free and the resolution limiting factor is the numerical aperture.

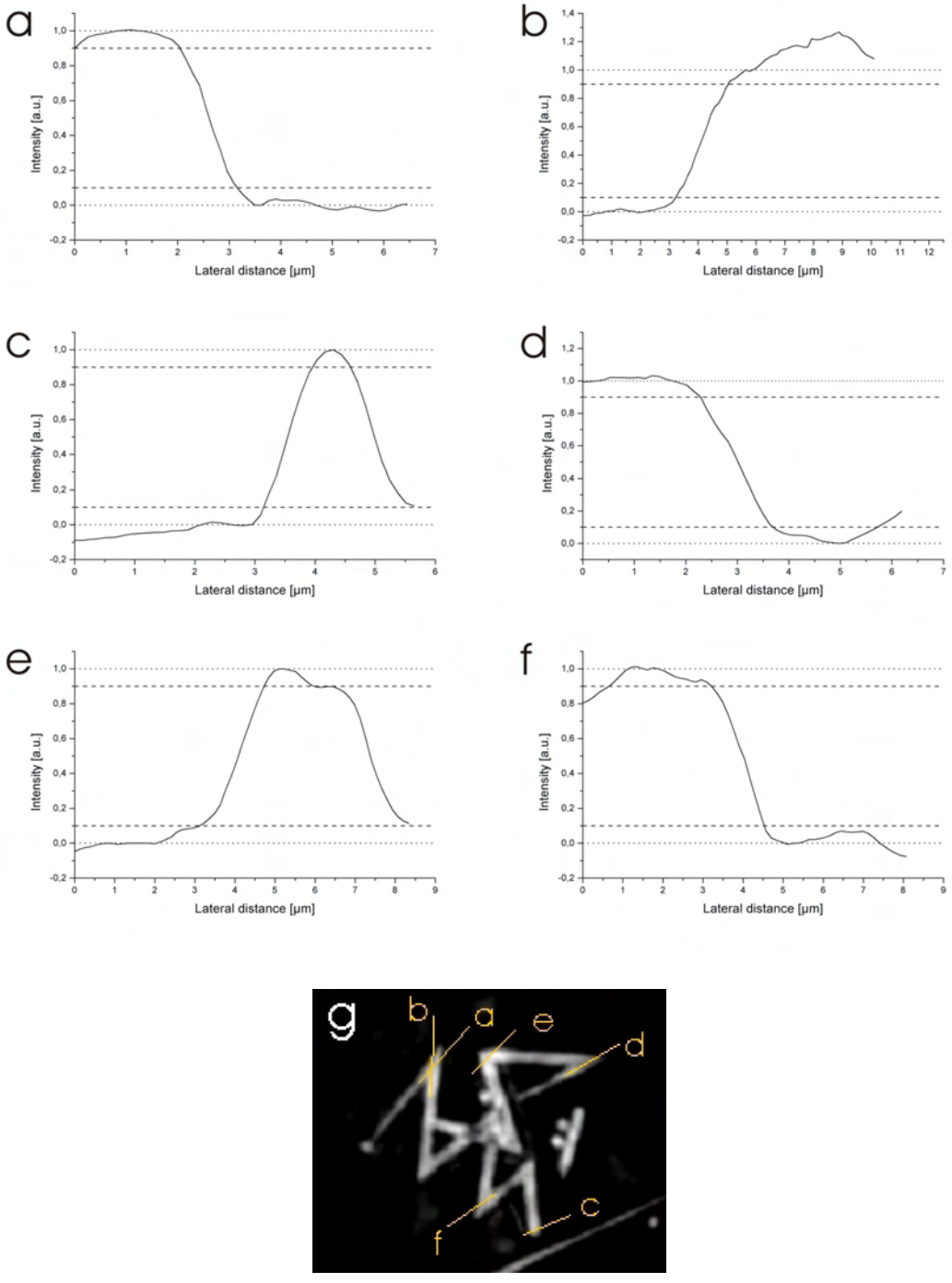

Figure 7.4: Linecuts of a lithographic structure
(a) to (f): Linecuts taken in the reconstruction of the lithographic structure (figure 7.1 (c)). The finite width over which the intensity rises from 10% to 90% gives the resolution $\delta_{\text{edge}} = 1.13 \pm 0.35$ µm.
(g): Positions of the linecuts.

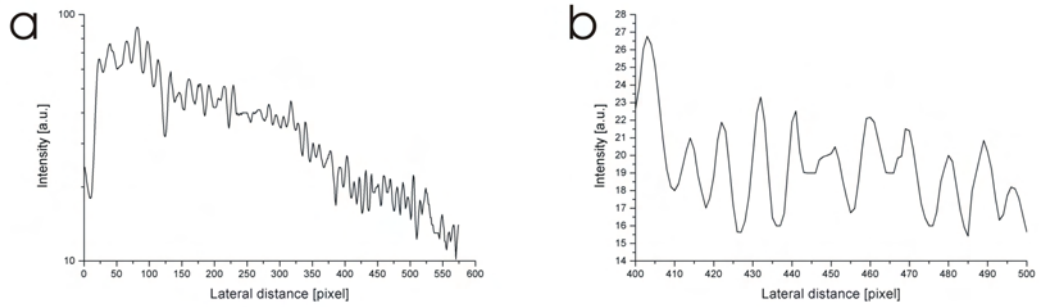

Figure 7.5: Linecuts of a hologram
(a) Linecut taken in the hologram of the lithographic structure (figure 7.1 (a)). The oscillations of the fringes are superimposed on the slope of the Airy disc.
(b): Magnified section from (a). The smallest fringe spacing is 10 pixel, which equals 135 µm.

7.2 Particle mixtures

As another test sample, a mixture of polystyrene beads (size 6 µm) and magnetic pigment was chosen in order to probe whether organic and metal oxide materials show material specific contrast differences at this wavelength. Figure 7.6 (a) shows the corrected hologram. While all other parameters were the same as for the lithographic sample, this hologram consists of only a single exposure with an exposure time of $T = 400$ s. Also here, the interference fringes are well visible, while a direct transmission can barely be seen.

In the reconstruction (figure 7.6 (b)), particles appear which have diverse shapes and sizes but exhibit nearly the same contrast properties. The different species cannot be distinguished by their absorption at this photon energy. Only a comparison with an optical microscopy image (figure 7.6 (c)), where the magnetic pigment appears dark and the polystyrene beads appear brighter, confirms that both types of particles are present in the field of view.

Also for this kind of sample, the resolution was determined via the knife-edge criterion. The linecuts are displayed in figure 7.7. The experimental value is $\delta_{\mathrm{edge}} = 0.90 \pm 0.20$ µm, which is in good agreement with the value found for the lithographic structures. Although beads are round and do not have sharp edges, the attenuation length of polystyrene at $E = 90$ eV of $d_{\mathrm{att}} = 0.306698$ µm [117] is much smaller than the average bead diameter of $d = 6$µm. Therefore, the beads almost work as knife-edge structures for soft X-rays. However, to better verify the results, the resolution was determined via two additional methods.

For the first alternative, one chooses a feature that is smaller than the predicted resolution and determines the apparent full width at half maximum d_{FWHM} [50].

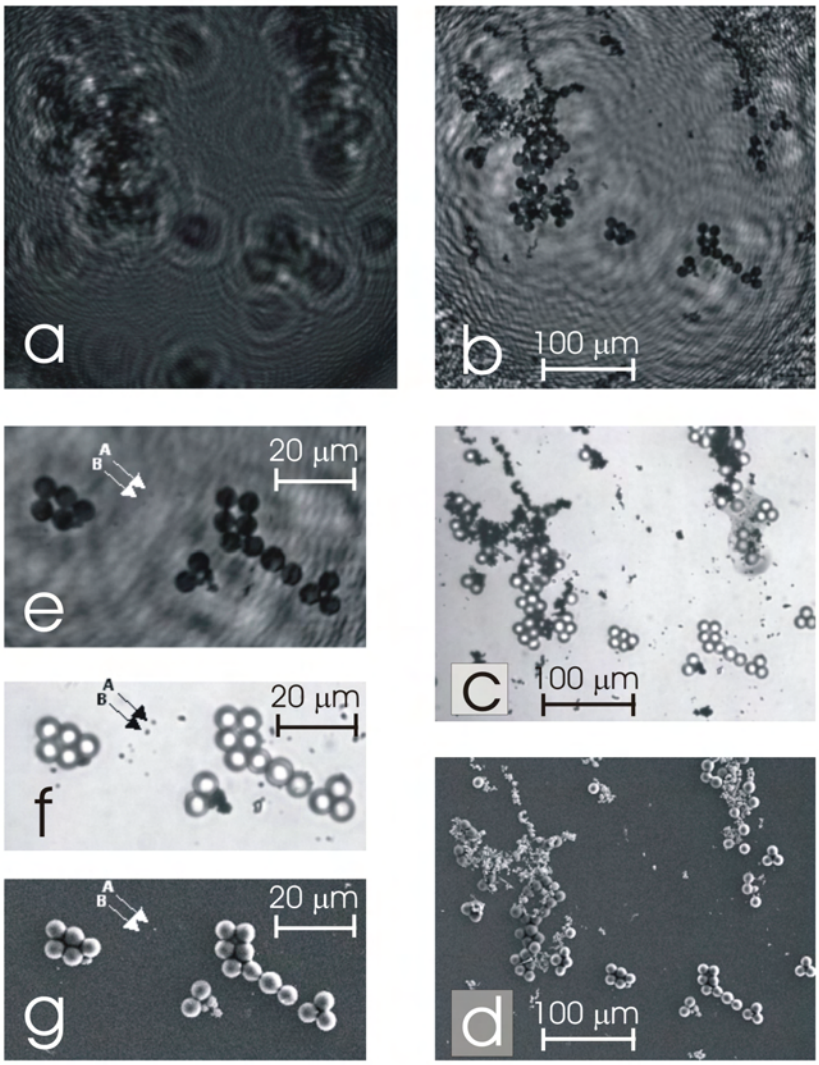

Figure 7.6: Particle mixture of polystyrene beads and magnetic pigment
(a): Hologram recorded at $E = 90$ eV. The interference fringes are well pronounced.
(b): Reconstruction of (a). Both particle types appear in the reconstruction and cannot be distinguished by their contrast.
(c): Optical microscopy image. The iron oxide particles are dark, the polystyrene particles appear brighter. Zeiss Axioplan2, $40\times$ Neofluar, NA 0.75
(d): Scanning electron microscopy image. Leo 1530
(e) to (g): Magnified region of interest of (b) to (d). Two small structures are indicated by arrows A and B.

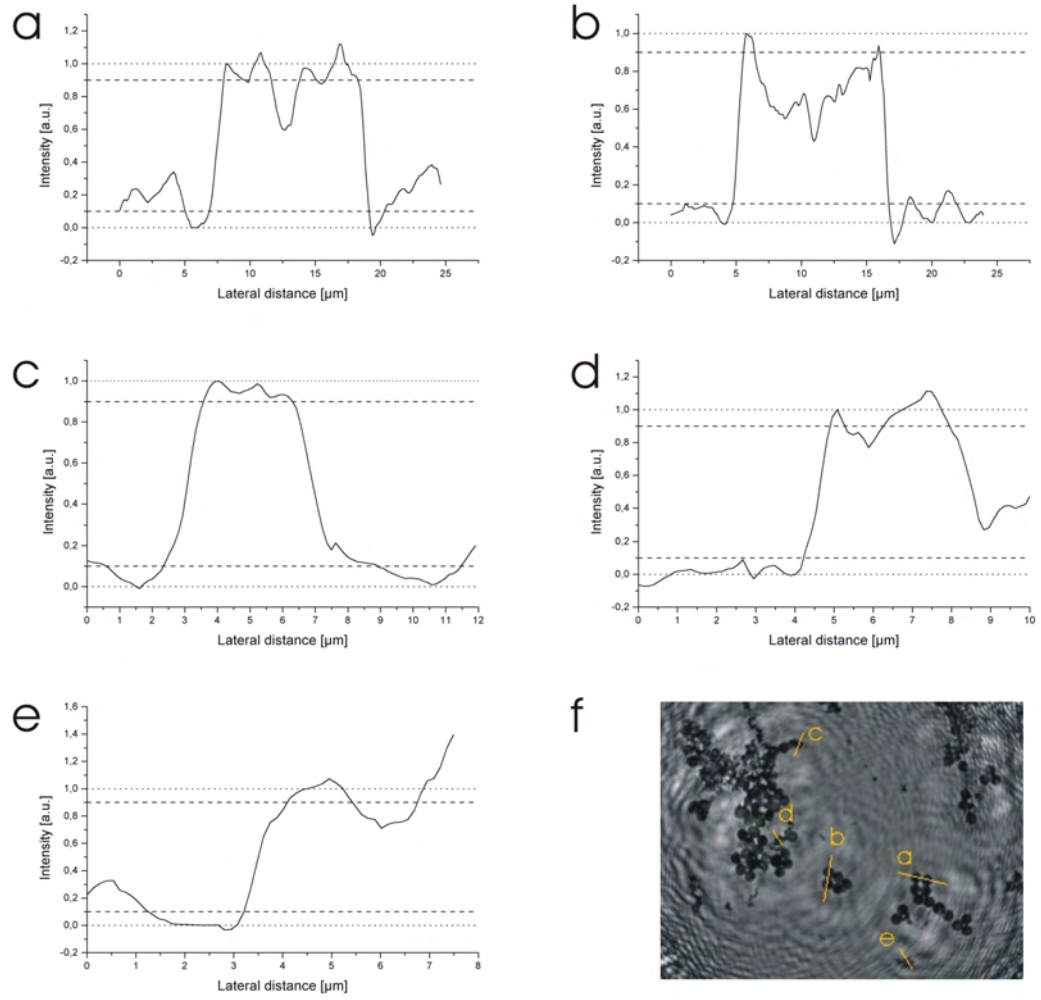

Figure 7.7: Linecuts of polystyrene beads
(a) to (e): Linecuts taken in the reconstruction of the polystyrene beads (figure 7.6 (b)). The finite width over which the intensity rises from 10% to 90% gives the resolution $\delta_{\text{edge}} = 0.90 \pm 0.20$ µm.
(f): Positions of the linecuts.

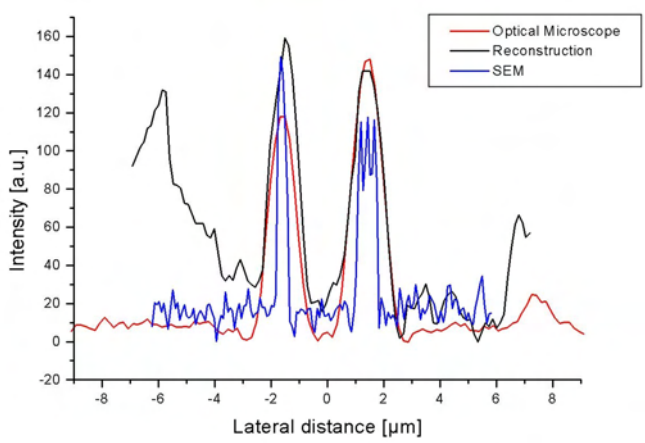

Figure 7.8: Determination of resolution via apparent Full Width at Half Maximum
Linecuts through the structures A and B denoted in figure 7.6 (e) to (g).
black: Reconstruction
red: Optical microscopy image
blue: SEM image
The FWHM of the structures in the reconstruction gives an achieved resolution of $\delta_{\mathrm{FWHM}} = 1.12 \pm 0.10$ µm.

The point spread function of a linear imaging system is the convolution of the point spread functions of the contributing elements. Assuming that the constituent point spread functions are Gaussian, the result is a Gaussian, too, and the total variance is the sum of the variances [99]

$$\sigma_{\mathrm{tot}} = \sum_i \sigma_{\mathrm{i}}. \tag{7.3}$$

As discussed in chapter 4, the variance σ of a Gaussian PSF is related to the resolution δ as

$$\delta = \sqrt{8 \ln 2}\, \sigma. \tag{7.4}$$

If the chosen feature is much smaller than the resolution limit, it can be approximated by a delta function. A convolution of a Gaussian with this function gives again a Gaussian with unchanged width, which means that the measured FWHM equals the attained resolution.

In figure 7.6 (e) to (g), the chosen particles are indicated by arrows A and B. The SEM image gives a true width $d = 0.33$ µm for particle A and $d = 0.65$ µm for particle B, while the linescans from the reconstructed image show $d_{\mathrm{FWHM}} = 1.05$ µm for particle A and $d_{\mathrm{FWHM}} = 1.19$ µm for particle B (compare figure 7.8), this results in an actual resolution of $\delta_{\mathrm{FWHM}} = 1.12 \pm 0.10$ µm.

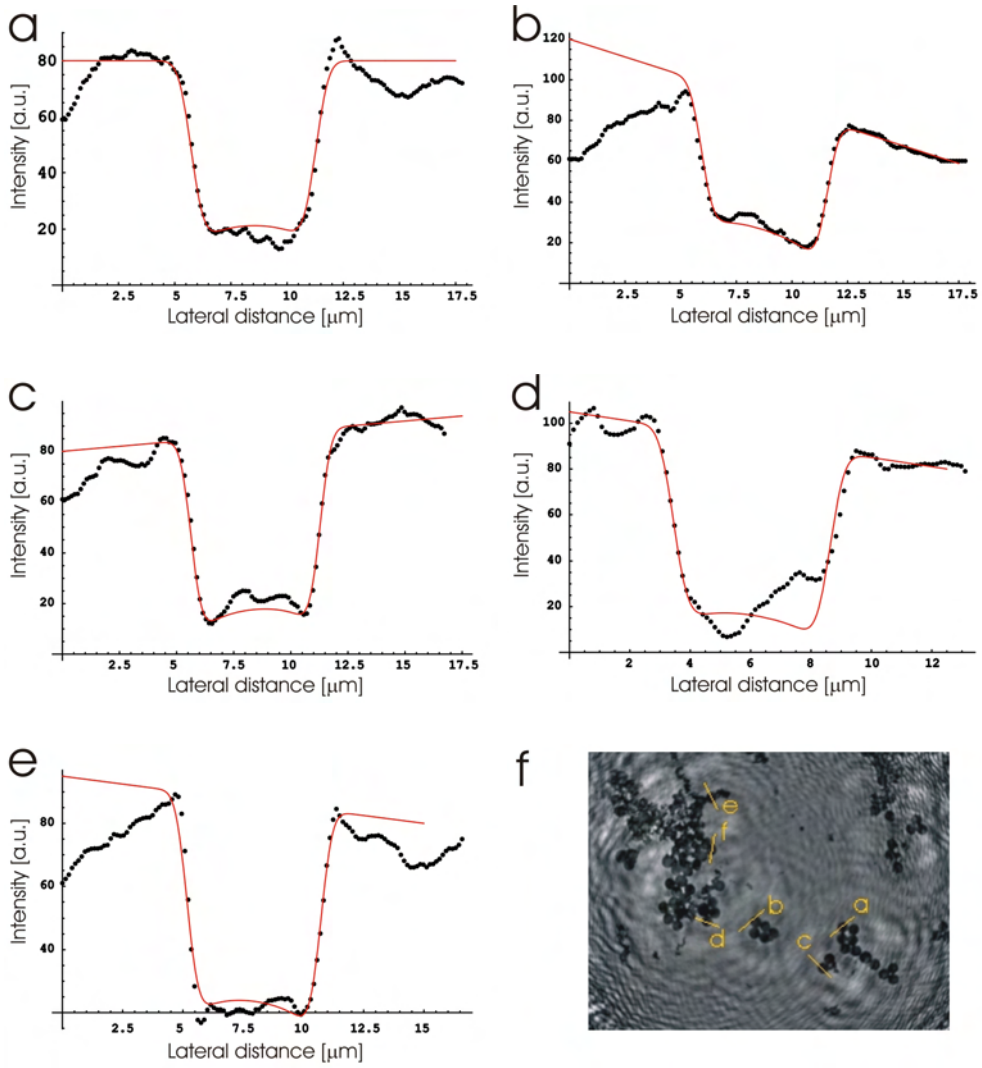

Figure 7.9: Determination of resolution via convolution with Gaussian function
The width σ of the Gaussian is varied until the fit (red curve) matches the data (black dots). With this method, the resolution was determined to $\delta_{\text{conv}} = 0.95 \pm 0.08$ µm.
(a) to (e): Linecuts and fits.
(f): Position of the linecuts in the reconstruction.

The second alternative is the determination of the width of the Gaussian PSF by fitting its convolution with the theoretical transmission of a bead to experimental linescans (compare figure 7.9) [11]. According to Lambert-Beer's law [70, 80], the theoretical transmission of a bead as a function of its thickness d can be written as

$$T(d) = \exp \frac{d}{d_{\text{att}}}, \tag{7.5}$$

with the attenuation length d_{att} as a fixed parameter. In a linescan, the thickness of a bead with radius r varies with the position x as

$$d(x) = 2\sqrt{r^2 - x^2}, \tag{7.6}$$

when the origin is in the center of the bead. The resulting theoretical transmission $T(x)$ is now convoluted with a Gaussian $g(x)$ yielding in a broadened transmission

$$B(x) = (T * g)(x) = \int_{-\infty}^{\infty} T(t)g(x-t)\,dt \tag{7.7}$$

$$= \int_{-\infty}^{\infty} \exp \frac{2\sqrt{r^2 - x^2}}{d_{\text{att}}} \frac{1}{\sigma\sqrt{2\pi}} \exp\left(-\frac{(x-t)^2}{2\sigma^2}\right) dt. \tag{7.8}$$

By varying σ until the fit matches the experimental linecut the best, a resolution of $\delta_{\text{conv}} = 0.95 \pm 0.08$ µm is found (compare equation (4.16)). This value is in agreement with the values above and the theoretical limit of $\delta_{\text{Kreuzer}} = 1.15$ µm is within $2\Delta\delta$.

The three methods for the determination of the resolution gave consistent values, resulting in an experimental resolution of about 1 µm, what is in the range of the theoretical prediction. Concerning the application of the different methods, the knife-edge criterion is probably the most practical one. The FWHM criterion requires objects much smaller than the predicted resolution limit and becomes unreliable when applied to larger structures. For the application of the convolution method, the exact shape of the object and the attenuation length must be known, so irregular structures with position dependent attenuation length are complicated to model. The knife-edge criterion, however, can be applied to any feature which provides an abrupt intensity variation.

7.3 Biological cells

Imaging biological cells with high resolution is a prerequisite for life sciences. To test the imaging properties of cells with digital in-line X-ray holography, dried rat embryonic fibroblast cells (REFs) were chosen. These cells are relatively

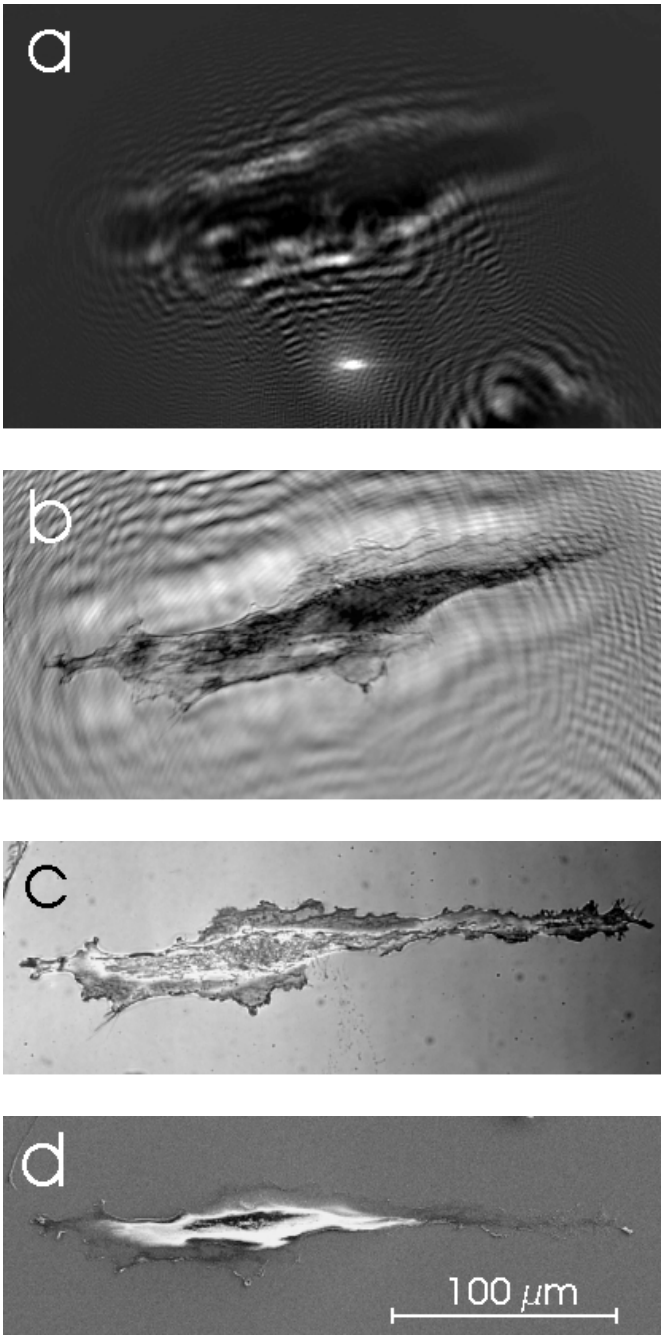

Figure 7.10: Rat embryonic fibroblast cell
(a): Hologram recorded at $E = 90$ eV. The interference fringes are well pronounced.
(b): Reconstruction of (a). The cell membrane appears in the reconstruction, and even structures within the cell are visible.
(c): Optical microscopy image. The membrane as well as structures within the bright nucleus are resolved. Zeiss Axioplan, $40\times$ Neofluar, NA 0.75
(d): Scanning electron microscopy image. Only the outline of the cell is visible. Leo 1530

modest to cultivate and adhere to the Si_3N_4 membranes. When adhered, they are several ten micrometers in size. The main question is whether small structures inside these extended objects such as nucleoli can be resolved by DIXH. Since the reference wave is essential to produce a distinct scattering pattern, it has to be tested if the remaining primary wave outside the object suffices for a reasonable reconstruction of the hologram.

The difference hologram (5 exposures, 2000 s total acquisition time) in figure 7.10 looks promising since well pronounced interference fringes can be seen. In the reconstructed image the cell membrane is imaged with great detail. Obviously, the thin layer of carbon rich material provides sufficient contrast for soft X-rays. Additionally, remarkable intracellular structures like the cell nucleus and filament arrangements[1] in the cytoskeleton are resolved. That means, either the reference wave present outside the object is sufficient, or thinner parts within the cell allow enough transmission for the reference wave.

A comparison with a SEM image (compare figure 7.10 (d)) shows that the outline of the cell reproduces in the reconstruction. Since SEM is a surface sensitive technique, no details within the cell can be resolved. Additionally, electrostatical charging effects lead to bright artifacts in the image. Optical microscopy (compare figure 7.10 (c)) reveals internal features which match with those visible in the reconstruction. But it also shows that the nucleus of the cell, which appears bright in the optical microscopy image, is not clearly resolved in holography. Here, only a dark region reproduces. Obviously, the mass absorption coefficient for carbon containing material of $\mu = 10^4$ cm^2/g [111] at 90 eV is high enough to provide good contrast in holography, but is probably too high to allow significant transmission through the dense material within the nucleus. However, the strong contrast especially of the filament arrangements and other structures within the cell proved VUV digital in-line holography having significant potential as microscopy technique of cell biological applications.

[1] In the cytosceleton, three types of fibers are present: microtubules, intermediate filaments, and actin filaments [118].

8 Development of resolution with pinhole generations

The dependence of the theoretically achievable resolution on the experimental geometry, especially the pinhole diameter, was discussed in chapter 4. In the following chapter, the resolution attained experimentally with the different pinholes is determined and compared to the theoretical expectations. An overview over the experimental parameters and achieved resolution is given in table 8.1.

8.1 Commercial pinholes

Commercial pinholes of two different nominal sizes were used for the experiments, both types were purchased from National Apertures, Inc.

8.1.1 Pinholes with nominal diameter A = 1.0 µm

As discussed in the previous chapter, the first experiments were carried out in the VUV region at 90 eV. The next three paragraphs present a brief summary of the results gained there.

A commercial pinhole of nominal diameter $A = 1.0$ µm was used to illuminate the detector 1 m downstream. The size of the Airy disc on the CCD chip as well as SEM images showed a real pinhole diameter of $A = 1.22 \pm 0.06$ µm and $A = 1.42 \pm 0.04$ µm, respectively. The size of the CCD chip $D = 27.65$ mm and the pinhole-detector distance lead to a geometrical numerical aperture of $\mathrm{NA}_{\mathrm{geom}} = \frac{D/2}{L} = 0.0138$, while the effective numerical aperture $\mathrm{NA}_{\mathrm{eff}} = q/L = 0.0118$ given by the radius q of the Airy disc on the detector and the pinhole-detector distance is slightly smaller.

The resolution was determined using a mixture of polystyrene beads (6 µm diameter) and magnetic pigment on a Si_3N_4 membrane, which was mounted in 10 mm distance to the pinhole. The expected effective resolution is $\delta_{\mathrm{eff}} = 0.70$ µm, while the resolution in analogy to the Abbe limit is $\delta_{\mathrm{Kreuzer}} = 1.15$ µm. Determining the resolution via the knife-edge criterion gives $\delta_{\mathrm{edge}} = 0.90 \pm 0.20$ µm. The achieved resolution was also determined by comparing the broadened full width

at half maximum (FWHM) in the image with the real FWHM gained from high resolution SEM images. This method results in $\delta_{\mathrm{FWHM}} = 1.12 \pm 0.10$ µm. As a last comparison, the theoretical transmission of a bead was convoluted with a Gaussian, and the variance σ was varied until the resulting fit best matched the experimental linecut. In this way, the resolution is $\delta_{\mathrm{conv}} = 0.95 \pm 0.08$ µm. All experimental values are in good agreement with each other but are larger than the theoretical expectation.

Mechanical drift is not a resolution limiting factor in this experimental setup, since the sample is fixed relative to the pinhole. Therefore, only a lateral shift larger than 135 µm leads to a loss of the smallest interference fringes and consequently to a worse resolution.

8.1.2 Pinholes with nominal diameter A = 0.5 µm

Further experiments were performed with a slightly altered setup. First of all, the pinhole was placed in the focus of the synchrotron beam, which was not possible in the previous setup. A higher photon flux is mandatory for shorter exposure times, especially when smaller pinholes should be employed. The pinhole-detector distance was reduced to $L = 800$ mm, and the sample was mounted on a separate manipulator. This change has several advantages. Now, the field of view as well a the magnification can be changed during the experiments, since the manipulator is movable independently from the sample holder in three dimensions. Furthermore, the sample can be retracted completely from the beam path, such that the diffraction pattern of the pinhole alone can be recorded. This so called source image (Airy disc) is subtracted from the recorded hologram to eliminate the image of the source in the reconstruction (compare equation (2.72)). The cost for these benefits is a higher sensitivity to vibrations and drift. A lateral displacement Δx of pinhole or sample relative to each other is projected onto the detector with a magnification depending on the pinhole-sample distance l and the pinhole-detector distance L resulting in a shift of the scattering pattern by the distance

$$\Delta X = \frac{L}{l}\Delta x. \tag{8.1}$$

In other words, a recognizable drift is present, if the shift of the scattering pattern on the detector is larger than the pixel size, in our case $p = 13.5$ µm, therefore, pinhole and sample must not move more than

$$\Delta x = \frac{l}{L}\Delta X = \frac{6\mathrm{mm}}{800\mathrm{mm}} \cdot 13.5\mu\mathrm{m} = 0.1\mu\mathrm{m}. \tag{8.2}$$

Here, an average pinhole-sample distance of $l = 6$ mm was assumed.

As in the VUV experiments (chapter 7), mixtures of polystyrene beads and magnetic pigment were chosen as test samples. Since the previously used polystyrene

beads with a diameter of $d = 6$ µm showed sufficient contrast, smaller particles with a diameter of $d = 2.2 \pm 0.1$ µm were chosen. These polystyrene beads were thus matched to the average size of the magnetic pigment.

A commercial pinhole with a nominal diameter of $A = 0.5$ µm was used. Again, SEM images and the size of the Airy disc on the detector gave a larger pinhole diameter of $A = 0.74 \pm 0.07$ µm and $A = 0.71 \pm 0.06$ µm respectively. The optimal relation between pinhole diameter A, detector distance L, and wavelength λ is given by equation (4.26). Since the pinhole diameter was halved with respect to the one used in the first experiments, but the pinhole-detector distance was reduced by only 20%, shorter wavelenghts—that is higher photon energies—can be accessed compared to the previous experiments.

The hologram of the particle mixture in figure 8.1 (a) was recorded at $E = 220$ eV photon energy. Since a bright spot originating from the direct transmission of the synchrotron beam through the pinhole membrane was present in the images and limited the exposure time to $T = 2$ s, 100 single exposures were added up to get sufficient photon statistics in the scattering pattern. In the corrected hologram, the spot was numerically suppressed and pronounced interference fringes are visible. However, the interference fringes in the vicinity of the spot are partly lost due to the suppression. It also becomes clear in figure 8.1 (a), that the Airy disc was too small to fully illuminate the detector, since the contrast strongly decreases toward the edges.

A comparison of the reconstructed image (figure 8.1 (b)) with optical microscopy (8.1 (c)) and SEM (8.1 (d)) images confirms, that both particle types appear in the reconstruction. The pinhole-sample distance is $l = 4.0$ mm. The particles reconstructed in the vicinity of the transmitted spot seem blurred, as a consequence of the suppression process. Also, since the contrast in the hologram decreases toward the edges of the CCD chip, a similar gradient is visible in the reconstruction. A closer look (figures 8.1 (e) and (f)) reveals, that the polystyrene beads in the reconstruction exhibit a doughnut shaped intensity profile similar to their appearance in optical microscopy, indicating that for this energy they are rather phase objects than absorption objects.

Resolution determination was done with the same three methods as before. The respective linecuts are displayed in figure 8.2 (a) to (e) (red curves). The knife-edge criterion gives $\delta_{\text{edge}} = 0.69 \pm 0.18$ µm, while the FWHM gives $\delta_{\text{FWHM}} = 1.02 \pm 0.35$ µm. In this case, the second method is not very accurate, since it only applies to structures smaller than the resolution limit. The beads through which the linecuts were drawn are 2 µm in diameter, which is significantly larger than the theoretical resolution limit of $\delta_{\text{eff}} = 0.37$ µm and $\delta_{\text{Kreuzer}} = 0.61$ µm, respectively. But the convolution method can be applied to objects of any size and gives $\delta_{\text{conv}} = 0.70 \pm 0.17$ µm. All the above values match with each other and especially with the theoretical prediction, but the large errors indicate the uncertainties

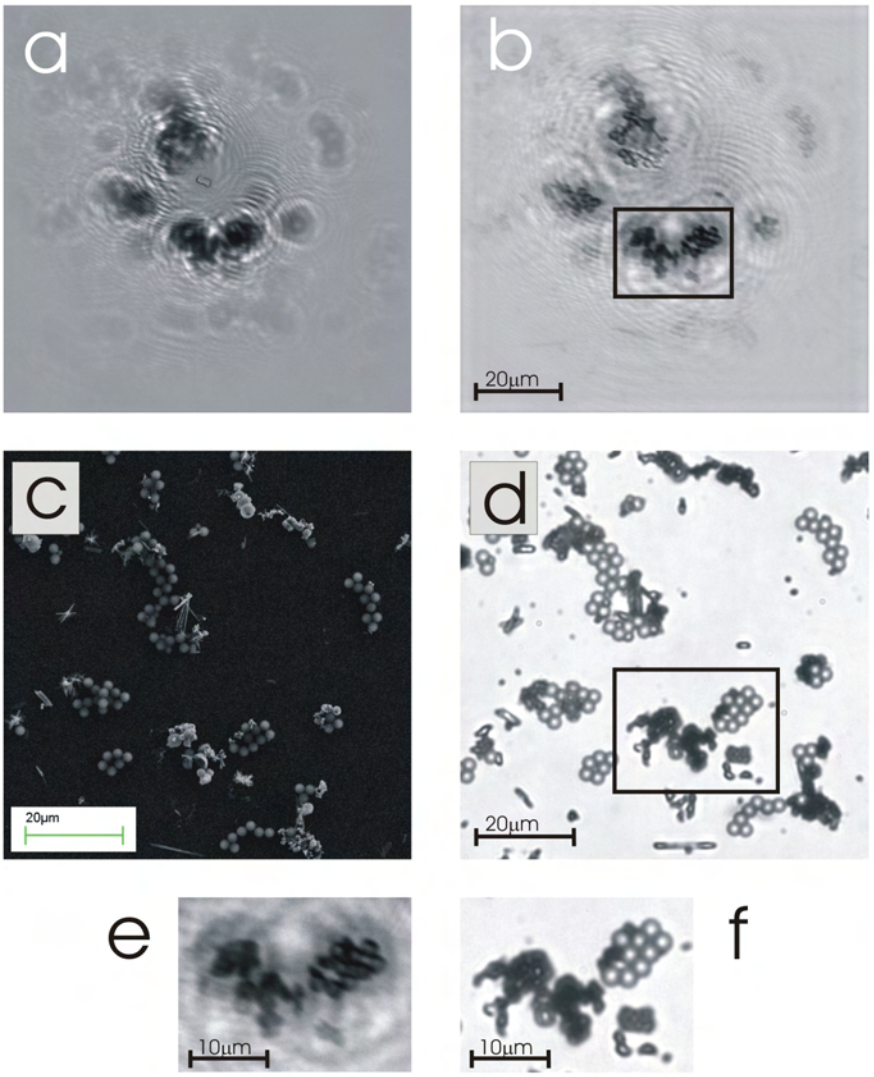

Figure 8.1: Particle mixture imaged with a pinhole of diameter $A = 0.71 \pm 0.06$ µm
(a): Hologram recorded at 220 eV. The direct transmission is numerically suppressed. The contrast decreases toward the edges due to the limiting size of the Airy disc.
(b): Reconstruction of (a) at a pinhole sample distance $l = 4.0$ mm. Both particle types are visible. The particles reconstructed in the vicinity of the transmitted spot appear blurred, since the interference fringes are partly lost in the suppression process.
(c): Scanning electron microscopy image. Leo 1530
(d): Optical microscopy image. The iron oxide particles are dark, while the polystyrene particles appear brighter. Zeiss Axioplan2, $40\times$ Neofluar, NA 0.75
(e) and (f): Magnified sections of (b) and (d), respectively. In both images, the polystyrene beads exhibit a doughnut shaped intensity profile.

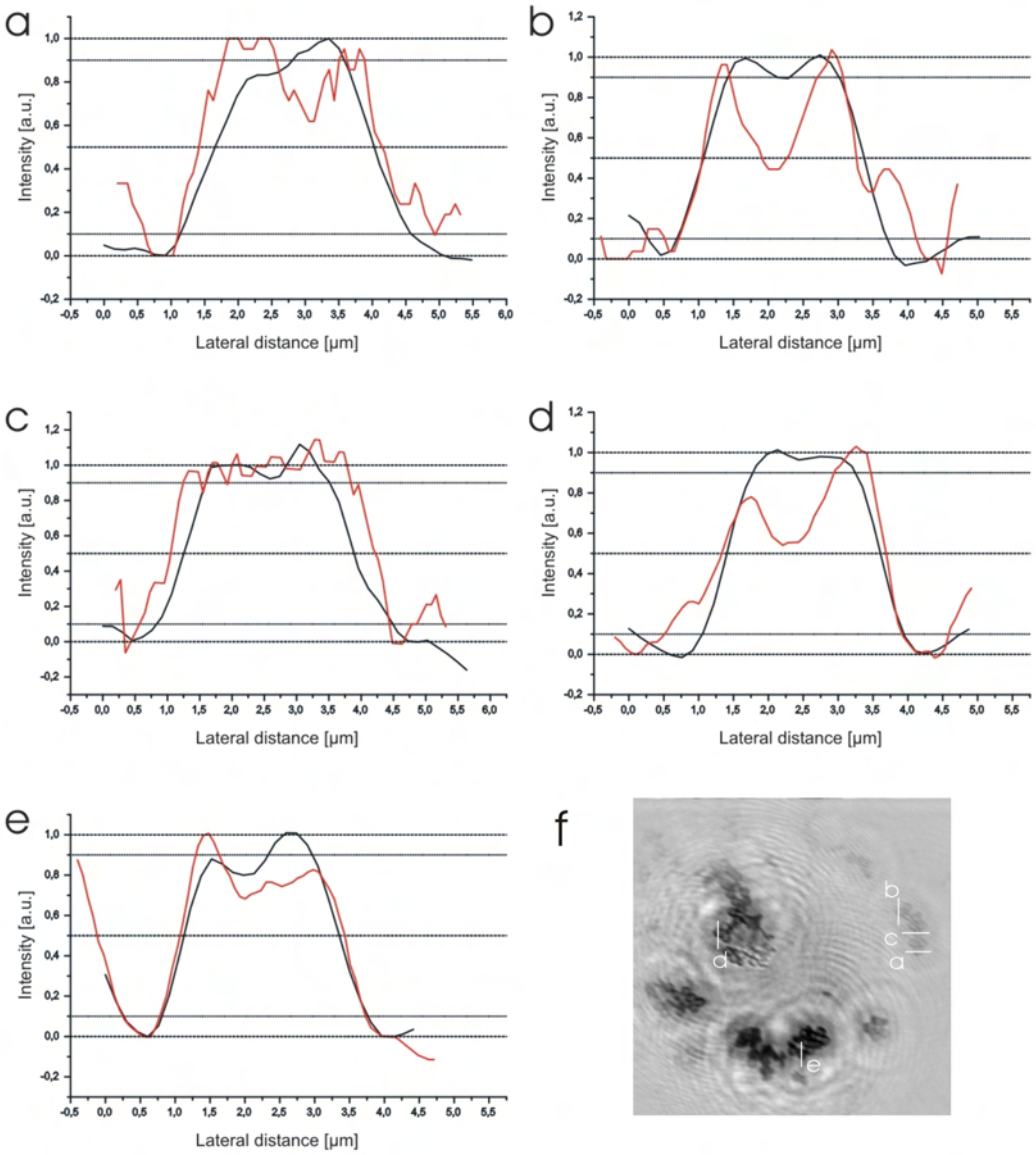

Figure 8.2: Linecuts of polystyrene beads
(a) to (e): Linecuts taken in the reconstruction of the polystyrene beads recorded with a pinhole of diameter $A = 0.71 \pm 0.06$ µm (figure 8.1 (b), red) and $A = 0.41 \pm 0.03$ µm (figure 8.3 (b), black). The knife-edge criterium gives the resolutions $\delta_{\text{edge}} = 0.69 \pm 0.18$ µm and $\delta_{\text{edge}} = 0.80 \pm 0.14$ µm, respectively, while the FWHM gives $\delta_{\text{FWHM}} = 1.02 \pm 0.35$ µm and $\delta_{\text{FWHM}} = 0.88 \pm 0.20$ µm. (f): The positions of the linecuts were identical in both reconstructions.

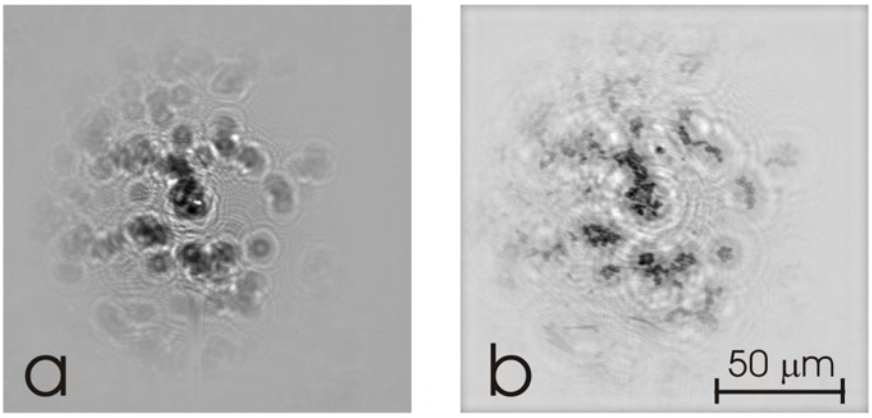

Figure 8.3: Particle mixture imaged with a pinhole of diameter $A = 0.41 \pm 0.03$ µm
(a): Hologram of the same sample as in figure 8.1 recorded at 220 eV.
(b): Reconstruction of (a). Compared to figure 8.1, the field of view is larger due to a slightly lower magnification.

underlying the applied methods.

8.2 Pinholes in thin gold membrane

Various experiments were performed with FIB milled pinholes in a thin gold membrane. Due to the smaller pinhole diameter compared to the commercial pinholes, higher photon energies are accessible. However, a decrease in the pinhole diameter necessitates longer exposition times, as discussed in chapter 5. Hence, drift effects, which were negligible in the experiments presented above, become of importance.

8.2.1 Drift-limited resolution

To test the influence of the pinhole diameter on the resolution, the same sample as in section 8.1.2 was imaged at the same photon energy and detector distance with a pinhole of 0.4 µm diameter, which was FIB milled in a 700 nm thick gold membrane. The gold membrane blocks the direct synchrotron beam better than the nickel foil, which is used as backing in the commercial pinholes. So exposition times of $T = 75$ s for one exposure were possible at a photon energy of $E = 220$ eV. Since the pinhole diameter is smaller than for the commercial pinhole, fewer photons pass the aperture per unit time, and the total acquisition time had to be increased, leading to 20 single exposures of $T = 75$ s each.

Comparing the hologram from figure 8.3 with the one in figure 8.1, one can see that the magnification has changed, which is due to a slightly increased pinhole-sample distance from $l = 4.0$ mm to now $l = 6.4$ mm. Therefore, the magnification changed from $M = 200$ to $M = 125$. The reconstruction itself is similar to the one before, as expected, since sample and photon energy are the same. As theoretical resolution limit, $\delta_{\text{eff}} = 0.20$ µm and $\delta_{\text{Kreuzer}} = 0.33$ µm are calculated. With experimental values of $\delta_{\text{edge}} = 0.80 \pm 0.14$ µm, $\delta_{\text{FWHM}} = 0.88 \pm 0.20$ µm (see figure 8.2 (a) to (e), black curves), and $\delta_{\text{conv}} = 0.88 \pm 0.08$ µm, this expectation is not met.

The most probable reason for the worse resolution is mechanical drift. As the total exposure time of $T_{400\text{nm}} = 20 \cdot 75$ s $= 1500$ s is much longer than $T_{710\text{nm}} = 200$ s for the commercial 500 nm pinhole as described in section 8.1.2, the influence of a constant drift between pinhole and sample onto the resolution drastically increases.

In two consecutive images that were recorded under the same conditions but with 15 min in between, a lateral translation of the interference pattern of $\Delta X = \sqrt{4^2 + 4^2}$ pixels$\hat{=}$76.4 µm was observed. This corresponds to a movement of the sample of

$$\frac{\Delta x}{\Delta t} = \frac{6.4\text{mm}}{800\text{mm}} \frac{76.4\mu\text{m}}{900\text{s}} = \frac{611\text{nm}}{900\text{s}} = 6.8\text{Å/s}. \tag{8.3}$$

Although this absolute value is very small, the drift effects are visible due to the long exposure times and the huge magnification. With equation (8.1) and the total exposure time of $T_{400\text{nm}} = 1500$ s, this value leads to a drift on the detector of $\Delta X_{400\text{nm}} = 127.5$ µm during exposure. This corresponds to 9.4 pixel and is about three times as large as the calculated minimal fringe spacing of $s_{400\text{nm}} = 3.2$ pixel (compare equation (4.39)). So the smallest fringes are lost and the resolution gets worse.

In the case of the commercial pinhole, the same motion over the shorter exposure time of $T_{710\text{nm}} = 200$ s leads to a shift of the interference pattern of only $\Delta X_{710\text{nm}} = 27.2$ µm, which corresponds to 2 pixels. Since the closest fringe spacing with those settings is $s_{710\text{nm}} = 9$ pixels, the drift does not effect the resolution in those experiments.

8.2.2 Drift-corrected holograms

To minimize the effects of drift, it is advisable to record multiple single images with rather short exposure times, correct them for drift, and then add them up to get reasonable photon statistics in the hologram. This method was applied to a sequence of 20 holograms of a chromosome spread sample, each having an exposure time of $T = 180$ s. The photon energy was $E = 260$ eV. With a pinhole-detector distance of $L = 700$ mm, a pinhole-sample distance $l = 1.78$ mm, and a

pinhole diameter of $A = 0.41$ µm, a theoretical resolution of $\delta_{\text{eff}} = 0.20$ µm and $\delta_{\text{Kreuzer}} = 0.34$ µm, respectively, follows.

To minimize the vibrations in the setup, an edge welded bellows was built in between the turbo pump near the sample manipulator and the beamline, and the cooling water of the pump was turned off during the measurements. Analyzing the images for the amount of drift, a lateral shift of $\Delta X = \sqrt{8^2 + 4^2}$ pixels$\hat{=}$120.7 µm over a period of $t = 1620$ s was observed, resulting in a movement of the sample of $\Delta x/\Delta t = 1.9$ Å/s. This is only 28% of the value calculated in equation (8.3). However, integrated over the total exposure time of $T_{\text{total}} = 20 \cdot 180$ s, it would lead to a drift on the screen of $\Delta X_{\text{total}} = 270.0$ µm, corresponding to 20 pixel. The smallest fringe spacing calculated for these experimental parameters is $s = 9.8$ pixel. Hence, the drift would massively influence the resolution.

Since the single exposures are recorded as separate images, it is possible to correct them for the drift before accumulation. In a single image, the drift only amounts to $X_{\text{single}} = 13.5$ µm, which corresponds to one pixel. Hence, the accumulated drift-corrected image can be considered free of drift.

A single exposure hologram, where only the direct transmitted beam is numerically suppressed, is shown in figure 8.4 (a). The first minimum of the Airy pattern can clearly be seen, while the interference fringes are quite faint. From each such image, the source image is subtracted, then the drift is corrected, and the 20 difference holograms are added up. The resulting drift corrected hologram is displayed in figure 8.4 (b). Now the photon statistic has improved and the interference fringes are clearly visible.

The resulting reconstruction and the corresponding microscopy image can be compared in figure 8.4 (c) and (d). Three chromosomes appear in the field of view. Since the cell cycle was stopped in the metaphase of mitosis, the chromosomes exist in the condensed form. In each chromosome, a pair of sister chromatids is attached to each other at the centromer [119]. According to literature, the chromatid pair has a width of 1.4 µm [7]. Determining the width w via the full width at half maximum in linecuts taken in both images (compare figure 8.5), gives $w_{\text{FWHM}} = 1.55 \pm 0.17$ µm for the reconstruction and $w_{\text{FWHM,opt}} = 1.67 \pm 0.18$ µm for the optical microscopy image. These values match the theoretical expectations. However, variations in the separation of the chromatids may occur, as can be seen in figure 6.4, so the theoretical value can be considered a lower border. The variations influence the measured width and lead to large errors.

In the same linecuts, the resolution was determined via the knife-edge criterion. Since the optical microscopy images were taken with a 40× Plan-Neofluar objective with a numerical aperture of NA = 0.75 at a wavelength $\lambda = 543$ nm, the theoretical resolution is $\delta_{\text{opt}} = 0.61\lambda/\text{NA} = 0.442$ µm. The knife-edge criterion gives a resolution of $\delta_{\text{edge,opt}} = 0.41 \pm 0.05$ µm, which is in good agreement with the theoretical value. For the reconstruction, the theoretical values are

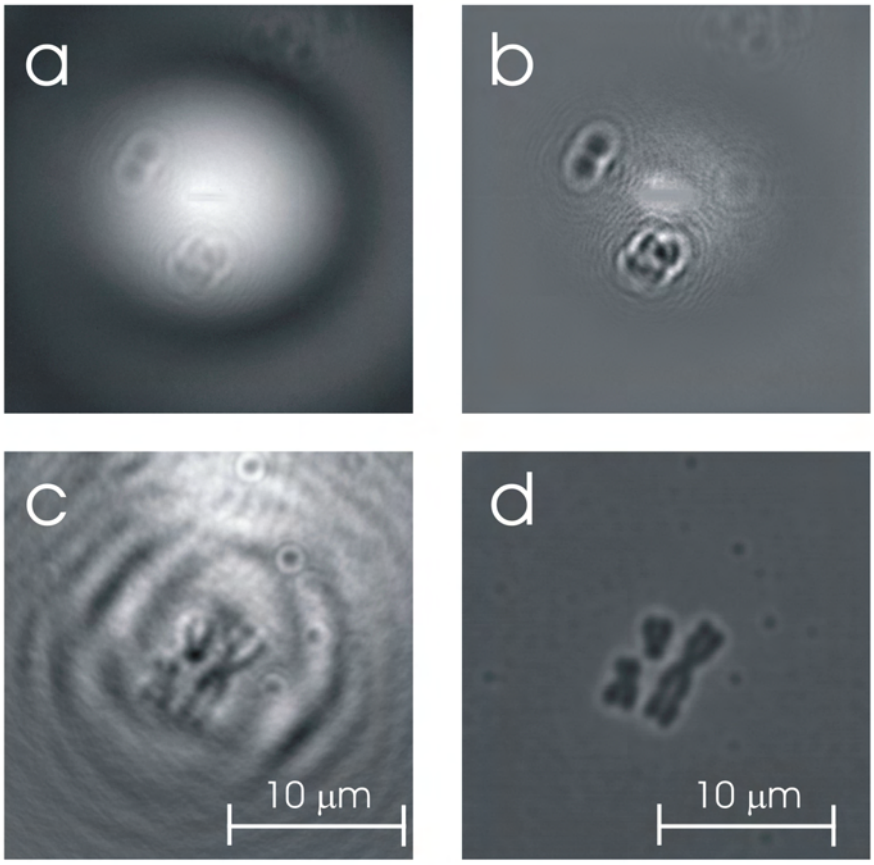

Figure 8.4: Chromosome sample imaged with a pinhole of diameter $A = 0.41 \pm 0.03$ µm
(a): Single hologram recorded at 260 eV. The direct transmission is numerically suppressed. The interference fringes are barely visible.
(b): Drift corrected sum of 20 difference holograms. Now the fringes are visible.
(c): Magnified section of the reconstruction of (b). Three chromosomes appear in the field of view.
(d): Optical microscopy image showing the same section as (c). Zeiss Axiovert 200M, $40\times$ Plan-Neofluar objective, NA 0.75

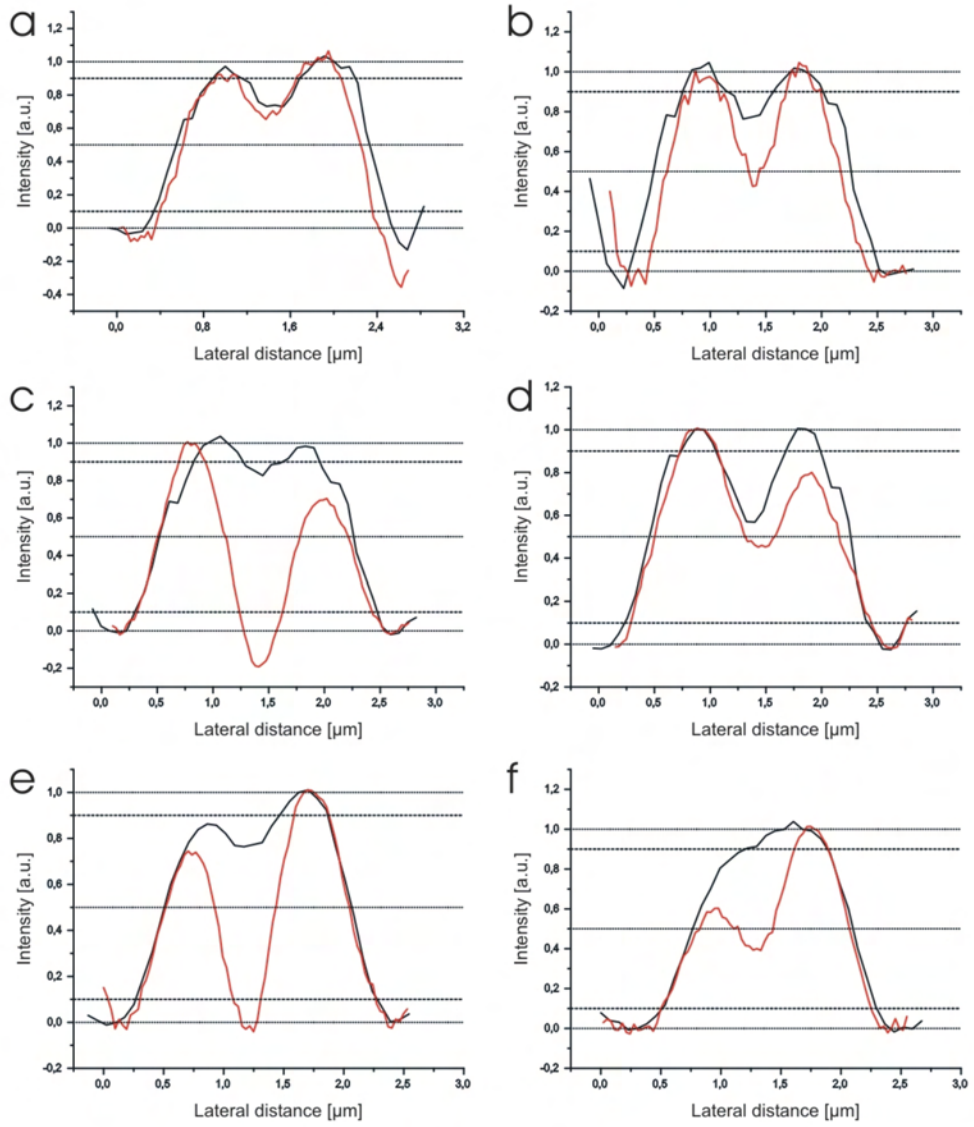

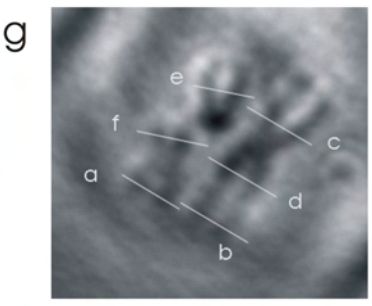

Figure 8.5: Linecuts through chromosome sample
(a) to (f): Linecuts taken in the reconstruction (red) and the optical image (black) of the chromosome sample (figure 8.4 (c) and (d)). The finite width over which the intensity rises from 10% to 90% gives the resolution $\delta_{\text{edge}} = 0.37 \pm 0.04$ µm. The width of the chromatid pairs is $w_{\text{FWHM}} = 1.55 \pm 0.17$ µm. The corresponding results for the optical image are $\delta_{\text{edge,opt}} = 0.41 \pm 0.05$ µm and $w_{\text{FWHM,opt}} = 1.67 \pm 0.18$ µm.
(g): Positions of the linecuts.

sample	*experimental parameters*					
	E [eV]	L [mm]	l [mm]	A [µm]	T [s]	drift
lithography	90	1000	10	1.42	2000	acc
beads	90	1000	10	1.42	400	acc
beads	220	800	4.0	0.71	200	acc
beads	220	800	6.4	0.41	1500	acc
chromosomes	260	700	1.78	0.41	3600	dc

sample	*resolution limit [µm]*						
	δ_{geom}	δ_{eff}	δ_{fringe}	δ_{Kreuzer}	δ_{edge}	δ_{FWHM}	δ_{conv}
lithography	0.60	0.70	0.16	1.15	1.13 ± 0.35	—	—
beads	0.60	0.70	0.16	1.15	0.90 ± 0.20	1.12 ± 0.10	0.95 ± 0.08
beads	0.20	0.37	0.08	0.61	0.69 ± 0.18	1.02 ± 0.35	0.70 ± 0.17
beads	0.20	0.20	0.13	0.33	0.80 ± 0.14	0.88 ± 0.20	0.88 ± 0.08
chromosomes	0.15	0.20	0.04	0.34	0.37 ± 0.04	—	—

Table 8.1: Comparison of the experimental and theoretical resolution limits
An overview over the experimental parameters, the resulting theoretical resolution limits and the experimental values for the experiments presented in the preceding and the present chapter is given. The theoretical resolution was determined as discussed in chapter 4. Concerning the drift effect, it is distinguished between accumulated (acc) and drift corrected (dc) summation of the holograms.

$\delta_{\text{eff}} = 0.20$ µm and $\delta_{\text{Kreuzer}} = 0.34$ µm, respectively. The experimental value is found to be $\delta_{\text{edge}} = 0.37 \pm 0.04$ µm, which also matches the theoretical prediction. So in this measurements, the resolution limit achieved with DIXH is smaller than in optical microscopy.

An overview over the experimental parameters, the resulting theoretical resolution limits and the experimental values for the experiments presented in the preceding and the present chapter is given in table 8.1. Summarizing, by increasing the numerical aperture with smaller pinholes and by correcting for drift effects, the experimental resolution could be improved by a factor of 2.5, meeting the theoretical predictions.

9 Intrinsic Contrast Mechanisms in digital in-line X-ray holography

A major advantage of synchrotron radiation is the tunability of the photon energy, since the absorption of radiation of a certain material strongly depends on it. Three major effects contribute to the absorption mechanism of X-rays in material: photo effect, Compton scattering, and pair production [80].

When the photon energy exceeds twice the rest mass of an electron ($m_e c^2 = 0.511$ MeV), an electron-positron pair can be created by which the energy of the photon is consumed. This process only occurs in a material, since the conservation of momentum is not satisfied in vacuum. The cross section for pair production is proportional to the square of the atomic number Z of the material and increases proportional to the logarithm of the photon energy [80]. In our experiments, this effect does not contribute, since the threshold energy is much higher than the photon energy used in the experiments.

The scattering of photons in material can be elastic or inelastic. In elastic processes, the energy of the photons is conserved, merely their momentum, that is their direction of travel, is altered. However, most scattering processes are inelastic and referred to as Compton scattering. The photon transfers energy and momentum onto an electron, that leads to a decrease in energy and a change in the direction of motion. Even back scattering is possible.

The dominating process in the energy region, in which our experiments were performed, is the photo effect [111]. In the X-ray region, the photons possess enough energy to excite electrons from a core level of the atoms to higher unoccupied shells or even vacuum level. In this process, the photon is absorbed. The created vacancy is filled with electrons from higher shells. The energy difference is radiated via fluorescence or is consumed by another electron which escapes the atom. This electron is called Auger electron. When the photon energy is increased and exceeds the binding energy of the next core level, those electrons can be excited, and the absorption increases abruptly. This sudden rise of the absorption is called absorption edge [80, 120]. Absorption and attenuation length d_{att} are related via Lambert-Beer's law [80]

$$I(z) = I(0) \exp\left\{\frac{z}{d_{\mathrm{att}}}\right\}, \tag{9.1}$$

where z is the covered distance, and $I(z)$ is the intensity of the radiation. So a rise of the absorption leads to a drop in the attenuation length. In figure 9.1, the attenuation length d_{att} of polystyrene and iron oxide as a function of the photon energy E is plotted. While the attenuation length of iron oxide rises slowly, polystyrene exhibits an absorption edge at $E = 284.2$ eV [117] due to the carbon present in the polymer.

The energy of those absorption edges is element specific because the energy levels of the electrons depend on the charge in the nucleus. So it is possible to determine the elemental composition of a material by determining the position of its absorption edges.

It is even possible to distinguish between different chemical states of one element by near edge X-ray absorption fine structure (NEXAFS) spectroscopy [121]. When the photon energy is just below or above the absorption edge of an element in a material, electrons can be excited into unoccupied molecular levels, leading to a fine-structure of the absorption, which is characteristic for the bonding structure of the element [122]. In this way, the presence of specific bonds in molecules can be detected, the lengths of these bonds can be determined, and the orientation of molecules on surfaces or in solids can be derived [121].

A combination of such a technique which is sensitive for the chemical composition of the sample with high spatial resolution enables detailed insights in the probed material. Two of these methods are scanning transmission X-ray microscopy (STXM) and X-ray photoemission electron microscopy (X-PEEM), which enable the determination of the distribution of chemical elements in a sample at better than 50 nm spatial resolution [123, 124].

To test the applicability of intrinsic contrast properties on digital in-line holography, experiments were carried out, which will be explained in the following chapter.

9.1 Elemental contrast experiments

As stated above, elements show characteristic X-ray absorption edges. By recording images on and off resonance of an absorption edge of a certain element and comparing the images with each other, it is possible to map the concentration of this element in the sample [123], since it shows much weaker absorption at energies below the edge than above the edge, while the contrast of the other constituents stays nearly constant (compare figure 9.1).

To explore whether this effect also occurs in holography, holograms of a mixture of polystyrene beads and iron oxide particles with an approximate particle diameter of $d = 2$ µm were recorded at energies below, right at and above the carbon-K-

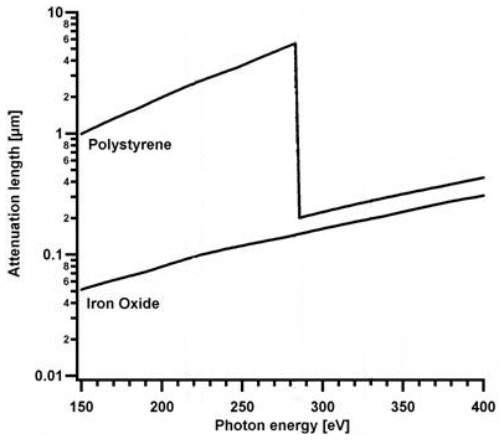

Figure 9.1: Attenuation length of Polystyrene and Iron Oxide as a function of photon energy
At the carbon K-edge, the absorption of polystyrene rises abruptly, while the absorption of iron oxide stays nearly constant.

absorption edge at $E = 284.2$ eV, namely at $E = 220$ eV, $E = 283$ eV, and $E = 330$ eV. The reconstructed images are displayed in figure 9.2.

At $E = 220$ eV, the attenuation length of iron oxide (Fe_2O_3, $\rho = 5.25$ g/cm^2 [125]) is $d_{\text{att}} = 0.09$ µm, constantly rising to $d_{\text{att}} = 0.19$ µm at $E = 330$ eV [117], which is much smaller than the particle size of about 2 µm. Therefore, these particles should give strong absorption contrast for all three wavelengths. The attenuation length for polystyrene ($\rho = 1.1$g/cm^2) of $d_{\text{att}} = 2.48$ µm at $E = 220$ eV, however, is in the range of the particle diameter, until it drops to $d_{\text{att}} = 0.19$ µm at the carbon edge and slowly rises to $d_{\text{att}} = 0.27$ µm at $E = 330$ eV. So one would expect the polystyrene particles to exhibit little contrast for energies below the absorption edge and strong contrast for higher energies. The attenuation length as a function of the photon energy is plotted in figure 9.1.

Looking at figure 9.2, all the particles visible in the reconstruction at 220 eV, figure 9.2 (a), also appear in image 9.2 (c), while some do not show up in image 9.2 (b). The decrease of intensity toward the corners of image 9.2 (c) are due to the Airy disc being smaller than the detector size, while the blurring in the center of the image is an artifact from the numerical suppression of the direct beam. A comparison with the optical microscopy image 9.2 (d) confirms, that those particles which show up in all three images consist of iron oxide, while the polystyrene beads become invisible at the carbon edge. This behavior is in contrast to the considerations above. According to the attenuation length, one would expect the polystyrene particles to exhibit similar contrast for both photon energies below the absorption edge, and much stronger contrast for the higher energy. Consequently, the explanation for this effect cannot be the attenuation length alone. But which other parameter influences the contrast?

In figure 9.3, sections from the reconstructions in figure 9.2 are magnified. The upper row shows predominantly iron oxide particles, while in the bottom row the major part of the imaged particles consists of polystyrene. At 330 eV, the attenuation length for both particle types is small compared to the particle di-

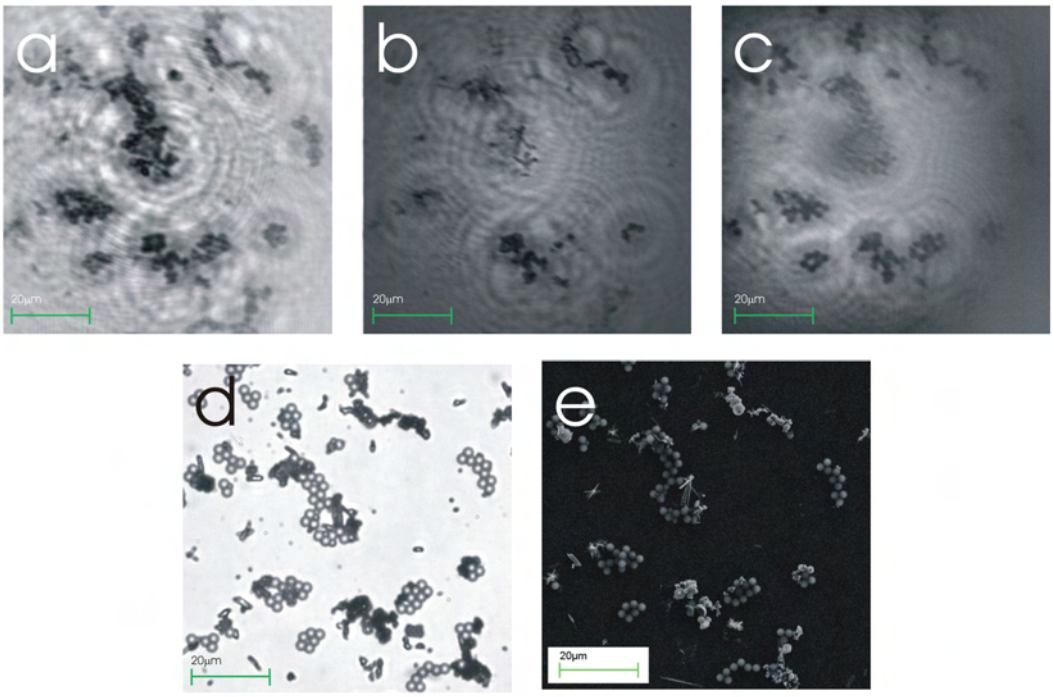

Figure 9.2: Particle mixture imaged at different energies
(a): 220 eV (b): 283 eV (c): 330 eV
(d): Optical microscopy image. Zeiss Axioplan2, $40\times$ Neofluar, NA 0.75
(e) Scanning electron microscopy image. Leo1530
In the optical microscopy image, the iron oxide particles appear dark, the polystyrene beads appear brighter. While both types of particles appear in the reconstructions (a) and (c), the polystyrene particles become invisible for a photon energy at the carbon K-edge and only the iron oxide particles reconstruct in (b).

ameter (compare figure 9.3 (d)), so the particles strongly absorb the X-rays and give good contrast as expected.

Taking a closer look at the polystyrene particles at the lowest energy (figure 9.3 (a) and (f)), the particles appear as a dark ring with a brighter spot in the middle. Such a doughnut-shaped intensity profile is an effect that usually occurs for phase objects in optical microscopy. This fact is an indication, that at this energy, the polystyrene beads rather act as phase objects than as amplitude objects. Phase objects barely absorb the illuminating radiation, but their refractive index n_{obj} differs from the one of the surrounding medium n. Within the object, the wavelength of the radiation is altered to $\lambda_{\mathrm{obj}} = \lambda/n_{\mathrm{obj}}$. Therefore a phase difference between the part of the wave that travels though the object and the part that passes the object is induced. When the parts of the wave brought to interference, this phase shift causes a phase contrast that makes the particles visible. Consid-

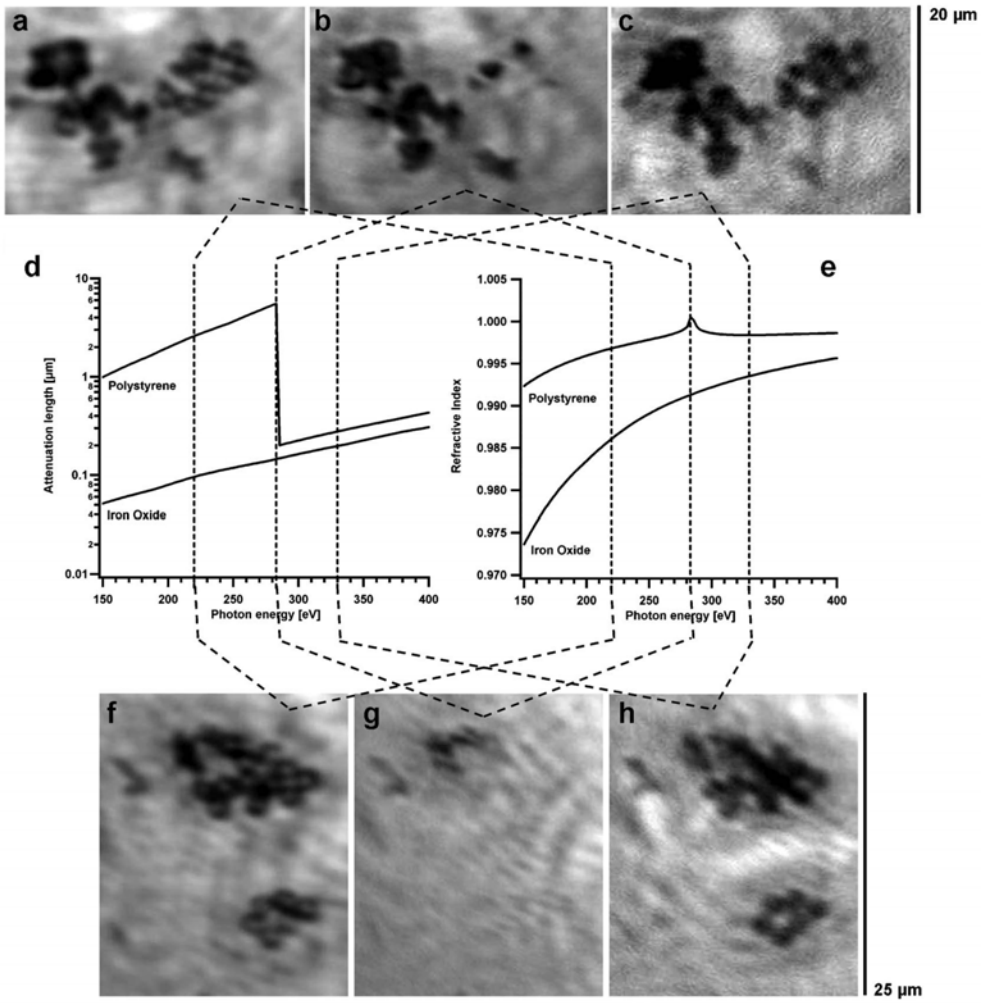

Figure 9.3: Dependence of contrast on photon energy
Magnified regions of interest of figure 9.2
(a) and (f): 220 eV (b) and (g): 283 eV (c) and (h): 330 eV
(d): Attenuation length of polystyrene and iron oxide as a function of the photon energy
(e): Refractive index of polystyrene and iron oxide as a function of the photon energy
At the carbon K-edge, the refractive index of polystyrene approaches the refractive index of vacuum $n = 1$, the particles become invisible for the X-ray beam.

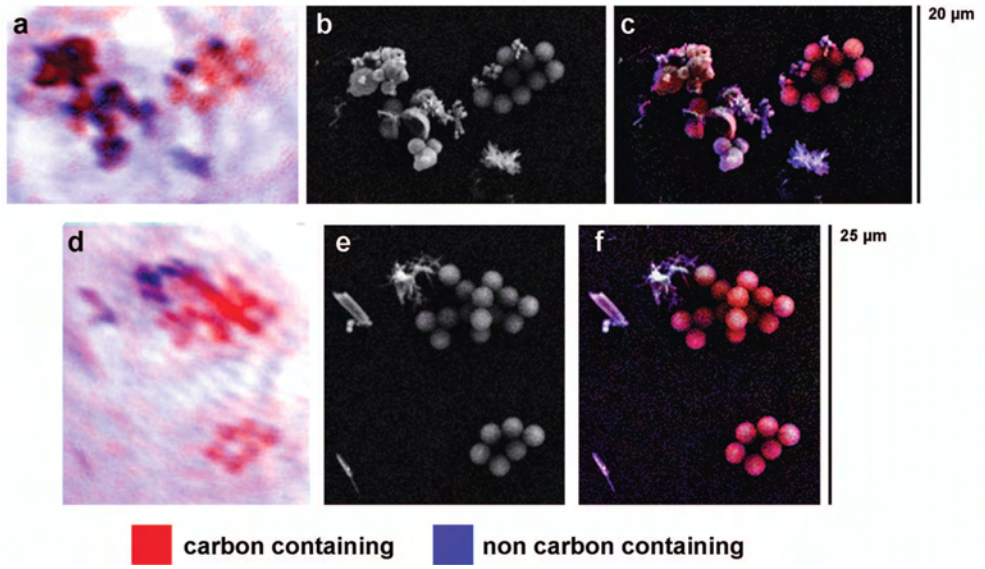

Figure 9.4: Color coded chemical information with high spatial resolution
False color images of the reconstructions in figure 9.3
(a) and (d): The reconstructions at different energies were color coded. Now the carbon rich material is represented in red, the iron oxide particles appear blue.
(b) and (e): Scanning electron microscopy images of the regions of interest. Leo 1530
(c) and (f): Overlay of the color coded reconstructions and the SEM images, unifying high spatial resolution imaging with chemical information.

ering sources for phase differences, the Si_3N_4-membrane can be neglected, since it induces a uniform phase shift on the whole wavefront and therefore no phase differences occur.

Now it can be explained, why the polystyrene beads become invisible at 283 eV (figure 9.3 (b) and (g)). Firstly, the attenuation length doubles with respect to $E = 220$ eV, resulting in even lower absorption. Secondly, and most importantly, toward the absorption edge, the refractive index of polystyrene approaches $n = 1$, the refractive index of vacuum, as plotted in figure 9.3 (e). Hence, the particles become transparent for the X-rays and cannot be imaged.

By comparing the reconstructed image of the hologram recorded at 283 eV, an energy right below the carbon K-absorption edge, with the one recorded above that energy at 330 eV, the different types of particles can be distinguished due to their different contrast behavior, and real elemental contrast is obtained [37].

With the reconstructions above, false-color elemental maps of the sample can be created. The reconstruction at 283 eV is assigned to the blue color channel, while the one at 330 eV is assigned to the red. A combination of both results in an image, where the pixel color indicates the predominant chemistry. The areas

where the carbon-containing material dominates appear red, and the non-carbon-containing material, that is in this case the iron oxide since no other material is present in the sample, appears blue, as can be seen in figure 9.3 (a) and (d).

In order to emphasize the elemental information in electron microscopy images with high spatial resolution (figure 9.3 (b) and (e)), the elemental maps obtained from holography as described above can be combined with the SEM images. The result is a color-coded composite image (figure 9.3 (c) and (f)), in which the additional element information enables the discrimination of the particle types, that cannot be distinguished by their shape alone. Correlative microscopy like this combines the high spatial resolution of electron microscopy and the element contrast of DIXH.

It should be emphasized here, that the advantage of digital in-line holography toward other X-ray microscopy techniques is that no zone plates have to be repositioned when the photon energy is changed. When the energy is altered, the holography setup stays unchanged, so the magnification and the field of view are maintained throughout the measurement. This is especially favorable for stack analysis, as no additional mechanical alignment is necessary.

9.2 Wavelength-dependence of contrast in biological samples

In cell biology, the localization of certain substances within a cell usually cannot be done directly but the substance in question has to be marked with a fluorescent dye so that it becomes prominent in the microscopy image. This staining, however, might influence the structure of the cell itself. Therefore, it is desirable to use intrinsic contrast mechanisms rather than staining.

Since the fundamental sensitivity of DIXH to chemical contrast mechanisms could be shown in the experiments described above, the applicability to biological samples was tested in the following experiments.

9.2.1 Rat Embryonic Fibroblast Cells

As first biological sample for energy-dependent contrast, critical-point-dried rat embryonic fibroblast (REF) cells prepared by the protocol described in chapter 6 were used. In figure 9.5 reconstructions of holograms recorded at $E = 100$ eV, figure 9.5 (a), and $E = 220$ eV, figure 9.5 (b), are displayed. The region of interest showing the cell nucleus is magnified in figures 9.5 (d) and (e). The exposure times for the holograms were $T = 3 \cdot 1000$ s and $T = 50 \cdot 30$ s, respectively, the single holograms were automatically accumulated and not drift corrected.

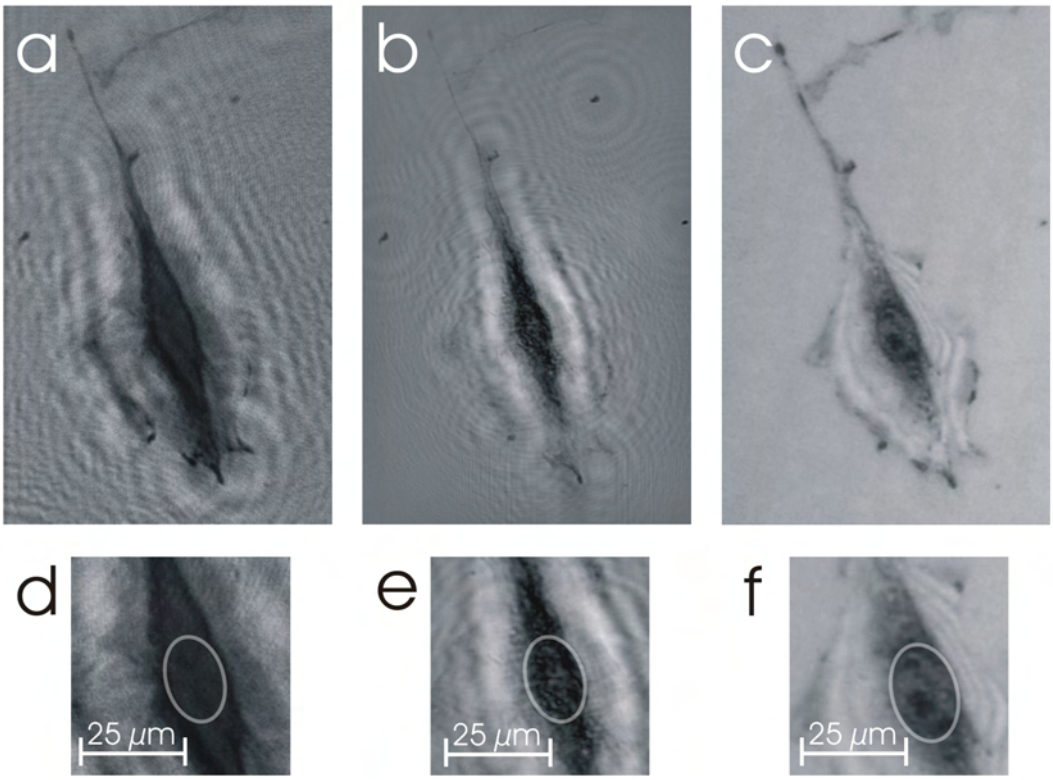

Figure 9.5: Reconstruction of a REF cell at different energies
(a) 100 eV (b) 220 eV
(c) Optical microscopy image. Zeiss Axioplan2, $40\times$ Neofluar, NA 0.75
(d) to (f): Magnified sections of (a) to (c), respectively. The position of the cell nucleus is highlighted.
With rising energy, the material becomes more and more transparent. The cell membrane disappears, and details within the nucleus become visible.

A comparison with an optical microscopy image 9.5 (c) and (f) verifies, that at the lower energy the outline of the cell is visible in the reconstruction while the nucleus cannot be penetrated. Most likely this is because the high absorption coefficient of the material causes a strong decay of the secondary wavefront scattered from this part of the sample. With rising photon energy, the absorption of carbon decreases, and the cell material becomes more and more transparent. The membrane disappears in the reconstruction, while now details within the nucleus and the cytoplasm are resolved.

Figure 9.6 shows images of another REF cell. In figure (a) the hologram ($T = 30 \cdot 40$ s, automatically accumulated and not drift corrected) recorded at 220 eV is shown, figure (b) is the reconstruction of (a). The nucleoli within the nucleus are clearly visible as dark features and exhibit good contrast, while the reconstruction

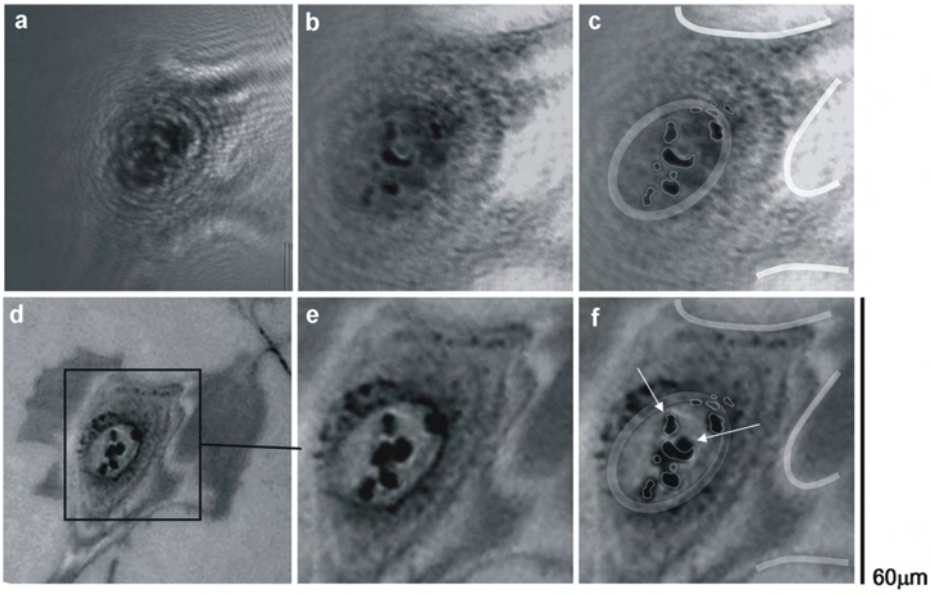

Figure 9.6: Reconstruction of a REF cell at different energies
(a) Hologram recorded at 220 eV
(b) Reconstruction of (a)
(c) The outline of the cell and some features in the nucleus are highlighted.
(d) Optical microscopy image. Zeiss Axioplan2, $40\times$ Neofluar, NA 0.75
(e) Region of interest as in (b)
(f) Image (e) with highlighted features.
The structure indicated by the left arrows appears the same in the reconstruction and in the optical microscopy, while the structure indicated by the right arrow is not visible with DIXH at 220 eV.

of the membrane is fuzzy. In order to guide the eye, some main features visible in figure 9.6 (b) were marked by a threshold and edge determination algorithm (figure 9.6 (c)). Additionally, the general shape of the cell is emphasized as well as the position of the nuclear membrane. For a comparison, an optical microscopy image is displayed in figure 9.6 (d). Figure (e) is a magnification of (d) showing the same section as (b). The highlighting shapes from figure (c) were directly transferred on the optical microscopy image (e), and the result is shown in (f).

While the general outline of the nucleus is the same, some of the structures within the nucleus exhibit different contrast properties in the reconstruction with respect to optical microscopy. For example, the feature indicated by the left arrow in figure 9.6 (f) appears similarly in both images, but the feature indicated by the right arrow is not present in the reconstruction. Obviously, it has lower contrast in X-ray holography at 220 eV than in optical microscopy. A cell nucleus might contain several types of sub-organelles, like nucleoli, Cajal bodies and Gemini of

coiled bodies (gems) (0.2–2.0 µm), and polymorphic interphase karyosomal associations (PIKA) domains (5 µm) [7, 126], to name only those in the size range of the observed structures, depending on the cell type and the state in cell cycle. The different contrast behavior expressed by various sub-organelles therefore might be due to different chemical composition, which leads to differences in the absorption and refractive index for X-rays and optical light. Identification of the different types is possible in fluorescence microscopy by specific staining. So cross-correlation experiments will be carried out in future. Another explanation might be a different material density in several sub-organelles, which considerably affects the attenuation length for X-rays. Visible light has a lower power to penetrate material, therefore even the sub-organelles with the least density would absorb the radiation and give good contrast. So all sub-organelles would appear dark in the optical image, while some of them do not absorb the X-ray sufficiently and hence do not appear in the reconstruction.

A definite explanation is still to be found, so further experiments will be carried out in our group with the goal of a more detailed biological interpretation. Cross-correlation experiments comparing DIXH with fluorescence microscopy should lead to a concept to translate material contrast in X-ray holography into the dye-localization-based language of biology.

9.2.2 Ulva linza

To test the energy-dependent contrast mechanism for a second biological sample, critical point dried zoospores of the green algae *Ulva linza* were imaged at various photon energies. In figure 9.7 (a) and (d) drift corrected holograms recorded at $E = 220$ eV ($T = 15 \cdot 5$ min) and $E = 500$ eV ($T = 6 \cdot 10$ min) respectively are displayed. The attenuation length of carbon ($\rho = 2.2$ g/cm^2 [125]) at 220 eV of $d_{\mathrm{att}} = 1.17$ µm is a factor of 3.5 higher than at 500 eV with $d_{\mathrm{att}} = 0.33$ µm [117]. In the first case, this value is larger than the average thickness of a dried cell, in the second case it is smaller. This fact explains why the second hologram shows high absorption within the scattering pattern of the algae, while the intensity at lower energy is more uniform throughout the hologram.

Figures 9.7 (b) and (e) are the corresponding reconstructions. At both energies, the outline of the cell is clearly visible, and intracellular structures are resolved. Obviously, even at an energy, where the attenuation length is higher than the sample thickness, the transmission of the object wave is high enough to convey sufficient information about internal structure. To facilitate the comparison of the two images, some features were identically highlighted in figures 9.7 (c) and (f). Those features appear in both reconstructions, however with inverted contrast with respect to each other. The reason for this behavior is not yet found. But an assumption is, that those areas consist of a material that has a much lower

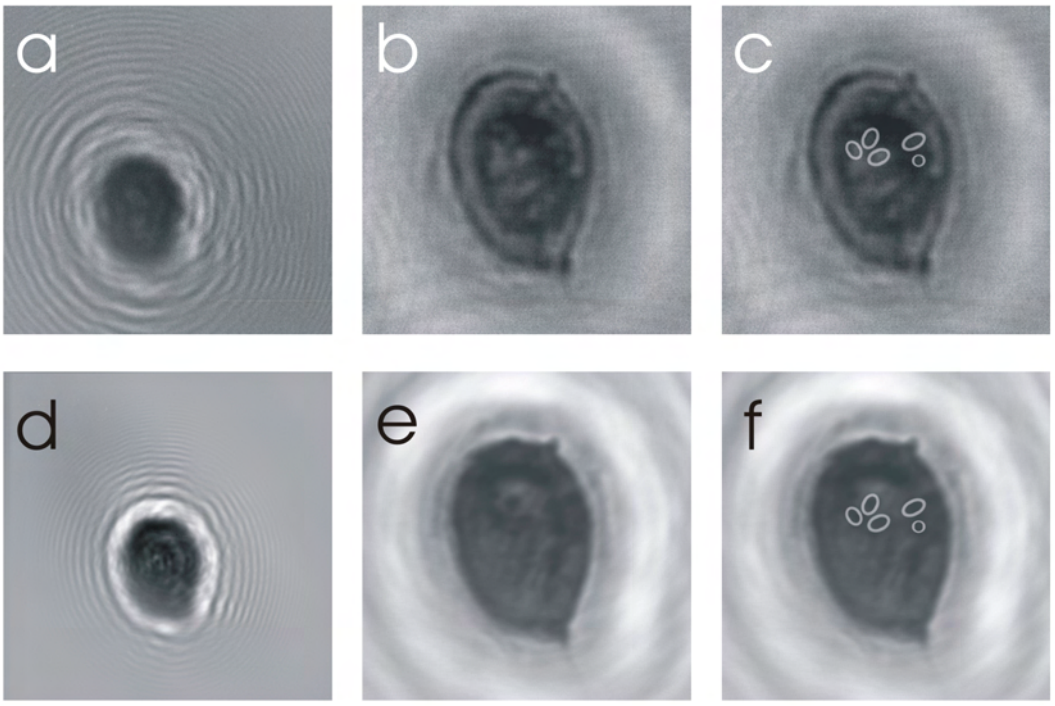

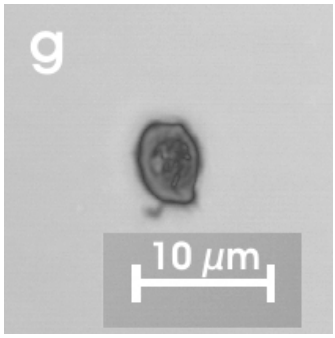

Figure 9.7: Reconstruction of a *Ulva linza* at different energies
(a) Drift corrected hologram recorded at 220 eV.
(b) Reconstruction of (a).
(c) Some features within the algae are highlighted.
(d) Drift corrected hologram recorded at 500 eV.
(e) Reconstruction of (d).
(f) The same features are highlighted as in (c).
(g) Optical microscopy image. Zeiss Axiovert 200M, $40\times$ Plan-Neofluar, NA 0.75
For some structures within the algae, the contrast behavior inverts when increasing the photon energy from 220 eV to 500 eV.

attenuation length at 220 eV than at 500 eV, possibly due to an absorption edge in this energy range. Elements, which occur in biological tissue in a significant amount and possess absorption edges in that energy region, are [111]

- carbon (K-edge at $E = 284.2$ eV),
- potassium (L-edge at $E = 294.6$ eV, $E = 297.3$ eV and $E = 378.6$ eV),
- nitrogen (K-edge at $E = 409.9$ eV), and
- calcium (L-edge at $E = 346.2$ eV, $E = 349.7$ eV and $E = 438.4$ eV).

The absorption edge of oxygen (K-edge at $E = 543.1$ eV) is beyond the probed energy range. A series of reconstructions at various energies in this range should make it possible to pinpoint the position of the edge and therewith the nature of the element.

9.3 Conclusion

In experiments with mixtures of polystyrene and iron oxide particles, which were imaged at energies below and above the carbon K-absorption edge, real elemental contrast was observed. The next step will be probing chemical contrast mechanisms as it is already done in NEXAFS spectroscopy. Experiments exploring intrinsic contrast mechanisms in biological cells were performed with rat embryonic fibroblast cells and zoospores of the green algae Ulva. Both samples showed regions which exhibit different contrast properties depending on the wavelength of the probing radiation. A probable reason is different chemical composition and/or material density leading to differences in the absorption and refractive index.

10 Conclusion and Outlook

In this thesis, the implementation of an in-line holographic setup with synchrotron radiation in the vacuum-ultraviolet (VUV) and soft X-ray region was successfully demonstrated. In the VUV region at a photon energy of $E = 90$ eV, lithographic structures in photo resist, mixtures of polystyrene beads and iron oxide particles, and dried rat embryonic fibroblast cells were imaged. All samples provided good contrast and led to reconstructable holograms. The achieved resolution was determined via the knife-edge criterion, giving a resolution of $\delta_{\mathrm{edge,L}} = 1.13 \pm 0.35$ µm for the lithography structure, and $\delta_{\mathrm{edge,P}} = 0.90 \pm 0.20$ µm for the particle mixture. In the reconstruction of the particle mixture, the resolution was also determined via two alternative methods. First, a feature that is smaller than the predicted resolution was chosen and the apparent full width at half maximum d_{FWHM} was determined. This number equals the attained resolution $\delta_{\mathrm{FWHM}} = 1.12 \pm 0.10$ µm. As second alternative, experimental linescans were fitted with a convolution of the theoretical transmission of a bead with a Gaussian point spread function. The width σ of the Gaussian function then gave an achieved resolution of $\delta_{\mathrm{conv}} = \sqrt{8 \ln 2}\,\sigma = 0.95 \pm 0.08$ µm. This value is consistent with the values above and the theoretical limit of $\delta_{\mathrm{Kreuzer}} = 1.15$ µm is within $2\Delta\delta$. The reconstructed image of the REF cell displays the cell membrane as well as intracellular structure, both in great detail. Thus, also extended objects can be imaged with DIXH.

As derived in chapter 4 the theoretical resolution limit for DIXH depends on the diameter of the pinhole used for the generation of the diverging wavefront. But not only the diameter determines whether a pinhole is suitable for DIXH. In order to sufficiently block the transmission of the synchrotron beam, a minimal thickness of the pinhole membrane is required. Hence, suitable pinholes were designed and fabricated by Focused Ion Beam milling.

A decrease in the pinhole diameter however leads to an increase in the exposure times required for hologram recording, therefore the influence of a constant drift between pinhole and sample onto the resolution increases, too. By application of smaller pinholes and correction for drift effects, the achieved resolution could be improved by a factor of 2.5, resulting in $\delta_{\mathrm{exp}} = 0.37 \pm 0.04$ µm. This value meets the theoretical prediction of $\delta_{\mathrm{theo}} = 0.34$ µm.

It could also be shown that by recording holograms on and off resonance with absorption edges, element contrast can be obtained. Also in biological samples,

a wavelength dependent contrast was observed.

For future developments, probing chemical contrast mechanisms similar to NEXAFS spectroscopy is planned. Also, a more detailed biological interpretation of the contrast differences observed in the images of the biological samples is aspired. Cross-correlation experiments comparing DIXH with fluorescence microscopy should lead to a concept to translate material contrast in X-ray holography into the dye-localization-based language of biology.

Another development is the application of DIXH to ultrashort pulsed, brilliant X-ray sources as free electron lasers. First experiments have been carried out in our group and the preliminary results look promising.

The introduction of an off-axis reference wave presents the possibility to enhance the resolution and simultaneously minimize the twin-image effect. In DIXH, the implementation can be realized by a double pinhole design. Also here, first promising experiments were performed.

In order to be able to access higher wavelengths and to further decrease the resolution limit, the concept for the creation of diverging wavefronts might have to be modified. The high aspect ration which is necessary in the current pinhole design already poses a challenge concerning pinhole fabrication. Waveguide based designs have been implemented for hard X-rays [35] and might be an alternative for the pinhole-based sources.

Bibliography

[1] E. Abbe.
Beiträge zur Theorie des Mikroskops und der mikroskopischen Wahrnehmung.
Arch. Mikrosk. Anat., 9:412–468, 1873.

[2] D. Wilkens.
Einblick in den Mikrokosmos.
`http://www.biokular.de/1999_2/Mikroskop.html`.
Accessed September 8th, 2005.

[3] Carl Zeiss AG.
Mikroskopie/Objektive für Forschung.
http://www.zeiss.de, retrieved September 8th, 2005.

[4] M. Schrader, K. Bahlmann, G. Giese, and S.W. Hell.
4Pi-Confocal Imaging in Fixed Biological Specimens.
Biophysical Journal, 75:1659–1668, 1998.

[5] H.J. Kreuzer, K. Nakamura, A. Wierzbicki, H.-W. Fink, and H. Schmid.
Theory of the point source electron microscope.
Ultramicroscopy, 45:381, 1992.

[6] W. Meyer-Ilse, D. Hamamoto, A. Nair, S.A. Lelièvre, G. Denbeaux, L. Johnson, A.L. Pearson, D. Yager, M.A. Legros, and C.A. Larabell.
High resolution protein localization using soft X-ray microscopy.
Journal of Microscopy, 201(3):395–403, 2001.

[7] Bruce Alberts, Alexander Johnson, Julian Lewis, Martin Raff, Keith Roberts, and Peter Walter.
Molecular biology of the cell.
Garland Science, 4th edition, 2002.

[8] P. Guttmann, B. Niemann, J. Thieme, D. Hambach, G. Schneider, U. Wiesemann, D. Rudolph, and G. Schmahl.
Instrumentation advances with the new X-ray microscopes at BESSY II.
Nuclear Instruments and Methods in Physics Research A, 467-468:849–852, 2001.

[9] D. Weiß, G. Schneider, B. Niemann, P. Guttmann, D. Rudolph, and G. Schmahl.
Computed tomography of cryogenic biological specimens based on X-ray microscopic images.
Ultramicrocsopy, 84(3–4):185–197, 2000.

[10] Janos Kirz, Chris Jacobsen, and Malcolm Howells.
Soft X-ray microscopes and their biological applications.
Quarterly Reviews of Biophysics, 28(1):33–130, 1995.

[11] C. Jacobsen, S. Williams, E. Anderson, M. T. Browne, C. J. Buckley, D. Kern, J. Kirz, M. Rivers, and X. Zhang.
Diffraction-limited imaging in a scanning transmission X-ray microscope.
Optics Communications, 86:351–364, 1991.

[12] C. Jacobsen, J. Kirz, and S. Williams.
Resolution in soft X-ray microscopes.
Ultramicroscopy, 47:55–79, 1992.

[13] A.P. Hitchcock, I. Koprinarov, T. Tyliszczak, E.G. Rightor, G.E. Mitchell, M.T. Dineen, F. Hayes, W. Lidy, R.D. Priester, S.G. Urquhart, A.P. Smith, and H. Ade.
Optimization of scanning transmission X-ray microscopy for the identification and quantitaion of reinforcing particles in polyurethanes.
Ultramicroscopy, 88:33–49, 2001.

[14] Noriyuki Iwata, Katsuhiko Tani, Atsuyuki Watada, Hiromi Ikeura-Sekiguchi, Toru Araki, and Adam P. Hitchcock.
Chemical component mapping of pulverized toner by scanning transmission X-ray microscopy.
Micron, 37(4):290–295, 2006.

[15] Günter Schmahl, Dietbert Rudolph, Bruno Lengeler, and Christian Schroer.
Röntgenlinsen.
Physikalische Blätter, 57(1):43, 2001.

[16] G. Binnig, C. F. Quate, and Ch. Gerber.
Atomic Force Microscope.
Physical Review Letters, 56(9):930–933, 1986.

[17] G. Binnig, Ch. Gerber, E.Stoll, T. R. Albrecht, and C. F. Quate.
Atomic Resolution with Atomic Force Microscope.
Europhysics Letters, 3(12):1281, 1987.

[18] J. Wintterlin, J. Wiechers, H. Brune, T. Gritsch, H. Höfer, and R. J. Behm.
Atomic-Resolution Imaging of Close-Packed Metal Surfaces by Scanning Tunneling Microscopy.
Physical Review Letters, 62(1):59, 1989.

[19] G. Binnig and H. Rohrer.
Scanning tunneling microscopye.
IBM Journal of Research and Development, 44(1/2):279–293, 2000.

[20] U.Ch. Fischer and D.W. Pohl.
Observation of Single-Particle Plasmons by Near-Field Optical Microscopy.
Physical Review Letters, 62(4):458, 1989.

[21] M.G.L. Gustafsson, D.A. Agard, and J.W. Sedat.
I^5M: 3D widefield light microscopy with better than 100 nm axial resolution.
Journal of Microscopy, 195:10, 1999.

[22] V. Westphal and S.W. Hell.
Nanoscale Resolution in the Focal Plane of an Optical Microscope.
Physical Review Letters, 94:143903, 2005.

[23] T.A. Klar, S. Jakobs, M. Dyba, A. Egner, and S.W. Hell.
Fluorescence microscopy with diffraction resolution barrier broken by stimulated emission.
PNAS, 97(15):8206–8210, 2000.

[24] A. Egner, S. Jakobs, and S.W. Hell.
Fast 100-nm resolution three-dimensional microscope reveals structural plasticity of mitochondria in live yeast.
PNAS, 99(6):3370–3375, 2002.

[25] M. Dyba and S.W. Hell.
Focal Spots of Size $\lambda/23$ Open Up Far-Field Florescence Microscopy at 33 nm Axial Resolution.
Physical Review Letters, 88:1639011–1639014, 2002.

[26] D. Baddeley, C. Carl, and C. Cremer.
4Pi microscopy deconvolution with variable point-spread-function.
Applied Optics, 45(27):7056–7064, 2006.

[27] D. Gabor.
A New Microscopic Principle.
Nature, 161(8):777, 1948.

[28] John J. Barton.
Photoelectron Holography.
Physical Review Letters, 61(12):1356–1359, 1988.

[29] H. J. Kreuzer, M. J. Jericho, I. A. Meinertzhagen, and Wenbo Xu.
Digital in-line holography with photons and electrons.
Journal of Physics: Condensed Matter, 13:10729–10741, 2001.

[30] A. Gölzhäuser, B. Völkel, M. Grunze, and H.J. Kreuzer.
Optimization of the low energy electron point source microscope: imaging of macromolecules.
Micron, 33:241–255, 2002.

[31] Jorge Garcia-Sucerquia, Wenbo Xu, Stephan K. Jericho, Peter Klages, Manfred H. Jericho, and H. Jürgen Kreuzer.
Digital in-line holographic microscopy.
Applied Optics, 45(5):836–850, 2006.

[32] S. K. Jericho, J. Garcia-Sucerquia, Wenbo Xu, M. H. Jericho, and H. J. Kreuzer.
Submersible Digital In-Line Holographic Microscope.
Review of Scientific Instruments, 77:043706/1–043706/10, 2006.

[33] L. Cser, Gy. Török, G. Krexner, I. Sharkov, and B. Faragó.
Holographic Imaging of Atoms Using Thermal Neutrons.
Physical Review Letters, 89:175504, 2002.

[34] Norio Watanabe and Sadao Aoki.

Three-dimensional tomography using a soft X-ray holographic microscope and CCD camera.
Journal of Synchrotron Radiation, 5:1088–1089, 1998.

[35] C. Fuhse, C. Ollinger, and T. Salditt.
Waveguide-Based Off-Axis Holography with Hard X Rays.
Physical Review Letters, 97(25):254801–1–254801–4, 2006.

[36] A. Rosenhahn, R. Barth, X. Cao, M. Schürmann, M. Grunze, and S. Eisebitt.
Vacuum-ultraviolet Gabor holography with synchrotron radiation.
Ultramicrocsopy, 107(12):1171–1177, 2007.

[37] A. Rosenhahn, R. Barth, F. Staier, T. Simpson, S. Mittler, S. Eisebitt, and M. Grunze.
Digital in-line soft x-ray holography with element contrast.
Journal of the Optical Society of America A, 25(2):416–422, 2008.

[38] P. Korecki, G. Materlik, and J. Korecki.
Complex γ-ray hologram: Solution to twin images problem in atomic resolution imaging.
Physical Review Letters, 86:1534–1537, 2001.

[39] R. Fitzgerald.
X-ray and g-ray Holography Improve Views of Atoms in Solids.
Physics Today Online (http://www.physicstoday.org/pt/vol-54/iss-4/p21.html), retrieved September 1st, 2005.

[40] P. Hariharan.
Basics of Holography.
Cambridge University Press, 2002.

[41] Ulf Schnars and Werner Jueptner.
Digital Holography.
Springer, 2005.

[42] E. N. Leith and J. Upatnieks.
Reconstructed Wavefronts and Communication Theory.
Journal of the Optical Society of America, 53(81):1377, 1962.

[43] W. Xu, M.H. Jericho, I.A. Meinertzhagen, and H.J. Kreuzer.
Digital in-line holography for biological applications.
Proceedings of the National Academy of Sciences, 98(20):11301–11305, 2001.

[44] H. J. Kreuzer, M. H. Jericho, and W. Xu.
Digital in-line holography with numerical reconstruction: three dimensional particle tracking.
Proceedings of SPIE, 4401:234–244, 2001.

[45] W. Xu, M.H. Jericho, I.A. Meinertzhagen, and H.J. Kreuzer.
Digital in-line holography of microspheres.
Applied Optics, 41(25):5367–5375, 2002.

[46] J. Garcia-Sucerquia, Wenbo Xu, M. H. Jericho, and H. Jürgen Kreuzer.

Immersion digital in-line holographic microscopy.
Optics Letters, 31(9):1211–1213, 2006.

[47] M. Howells, C. Jacobsen, J. Kirz, R. Feder, K. McQuaid, and S. Rothman.
X-ray holograms at improved resolution: a study of zymogen granules.
Science, 238:514, 1987.

[48] J.E. Trebes, S.B. Brown, E.M. Campbell, D.L. Matthews, D.G. Nilson, G.F. Stone, and D.A. Whelan.
Demonstration of X-ray Holography with an X-ray Laser.
Science, 238:517–519, October 1987.

[49] Steve Lindaas, Malcolm Howells, Chris Jacobsen, and Alex Kalinovsky.
X-ray holographic microscopy by means of photoresist recording and atomic-force microscope readout.
Journal of the Optical Society of America A, 13(9):1788, 1996.

[50] Anne-Sophie Morlens, Julien Gautier, Gilles Rey, Philippe Zeitoun, Jean-Pascal Caumes, Marylène Kos-Rosset, Hamed Merdji, Sophie Kazsmias, Kevin Cassou, and Marta Fajardo.
Submicrometer digital in-line holographic microscopy at 32 nm with high-order harmonics.
Optics Letters, 31(21):3095–3097, 2006.

[51] Ian McNulty, Janos Kirz, Chris Jacobsen, Erik H. Anderson, Malcolm R. Howells, and Dieter P. Kern.
High-Resolution Imaging by Fourier Transform X-ray Holography.
Science, 2563:1009, 1992.

[52] S. Eisebitt, J. Lüning, W. F. Schlotter, M. Lörgen, O. Hellwig, W. Eberhardt, and J. Stöhr.
Lensless imaging of magnetic nanostructures by X-ray spectro-holography.
Nature, 432:885–888, 2004.

[53] Olav Hellwig, Stefan Eisebitt, Wolfgang Eberhardt, William F. Schlotter, Jan Lüning, and Joachim Stöhr.
Magnetic imaging with soft x-ray spectroholography.
Journal of Applied Physics, 99:08H307–1, 2006.

[54] Jianlin Zhao, Hongzhen Jiang, and Jianglei Di.
Recording and reconstruction of a color holographic image by using digital lensless Fourier transform holography.
Optics Express, 16(4):2514–2519, 2008.

[55] M. Tegze and G. Faigel.
X-ray holography with atomic resolution.
Nature, 380:49, 1996.

[56] A. Szöke.
In D.T. Attwood and J. Bokor, editors, *Short Wavelength Coherent Radiation: Generation and Applications*, number 147 in AIP conference proceedings, page 361. AIP, New York, 1986.

[57] T. Gog, P.M. Len, G. Materlik, D. Bahr, C.S. Fadley, and C. Sanchez-

Hanke.
Multiple-Energy X-Ray Holography: Atomic Images of Hematite (Fe_2O_3).
Physical Review Letters, 76(17):3132, 1996.

[58] M. Tegze, G. Faigel, S. Marchesini, M. Belakhovsky, and A.I. Chumakov.
Three Dimensional Imaging of Atoms with Isotropic 0.5Å Resolution.
Physical Review Letters, 82(24):4847, 1999.

[59] M. Tegze, G. Faigel, S. Marchesini, M. Belakhovsky, and O. Ulrich.
Imaging light atoms by X-ray holography.
Nature, 407(22):38, 2000.

[60] J.J. Barton.
Removing Multiple Scattering and Twin Images from Holographic Images.
Physical Review Letters, 67(22):3106, 1991.

[61] Jianwei Miao, Tetsuya Ishikaw, Bart Johnson, Erik H. Anderson, Barry Lai, and Keith O. Hodgson.
High Resolution 3D X-Ray Diffraction Microscopy.
Physical Review Letters, 89(8):088303, 2002.

[62] Jianwei Miao, Keith O. Hodgson, Tetsuya Ishikawa, Carolyn A. Larabell, Mark A. LeGros, and Yoshinori Nishino.
Imaging whole Escherichia coli bacteria by using single-particle x-ray diffraction.
Journal of Microscopy, 100(1):110–112, 2002.

[63] Jianwei Miao, Tetsuya Ishikawa, Erik H. Anderson, and Keith O. Hodgson.
Phase retrieval of diffraction patterns from noncrystalline samples using the oversampling method.
Physical Review B, 67:174104, 2003.

[64] Henry N. Chapman, Anton Barty, Michael J. Bogan, Sébastien Boutet, Matthias Frank, Stefan P. Hau-Riege, Stefano Marchesini, Bruce W. Woods, Saša Bajt, W. Henry Brenner, Richard A. London, Elke Plönjess, Marion Kuhlmann, Rolf Treusch, Stefan Düsterer, Thomas Tschentscher, Jochen R. Schneider, Eberhard Spiller, Thomas Möller, Christoph Bostedt, Matthias Hoener, David A. Shapiro, Keith O. Hodgson, David van der Spoel, Florian Burmeister, Magnus Bergh, Carl Caleman, Gösta Huldt, M. Marvin Seibert, Filipe R. N. C. Maia, Richard W. Lee, Abraham Szöke, Nicusor Timneanu, and Janos Hajdu.
Femtosecond diffractive imaging with a soft-X-ray free-electron laser.
Nature Physics, 2:8394, 2006.

[65] Henry N. Chapman, Stefan P. Hau-Riege, Michael J. Bogan, Saša Bajt, Anton Barty, Sébastien Boutet, Stefano Marchesini, Matthias Frank, Bruce W. Woods, W. Henry Brenner, Richard A. London, Urs Rohner, Abraham Szöke, Eberhard Spiller, Thomas Möller, Christoph Bosted, David A. Shapiro, Marion Kuhlmann, Rolf Treusch, Elke Plönjess, Florian Burmeister, Magnus Bergh, Carl Caleman, Gösta Huldt, M. Marvin Seibert, and Janos Hajdu.

Femtosecond time-delay X-ray holography.
Nature, 448:676, 2007.

[66] Eugene Hecht.
Optik.
Oldenbourg, 4th edition, 2005.

[67] Miles V. Klein and Thomas E. Furtak.
Optik.
Springer-Verlag, 25th edition, 1988.

[68] Dieter Meschede.
Optik, Licht und Laser.
Teubner, 2nd edition, 2005.

[69] Bahaa E.A. Saleh and Malvin Carl Teich.
Fundamentals of Photonics.
Wiley, 2nd edition, 2007.

[70] multiple authors.
Bergmann - Schaefer: Lehrbuch der Experimentalphysik: Optik, volume 3.
Walter de Gruyter, 10th edition, 2004.

[71] Max Born and Emil Wolf.
Principles of Optics.
B. G. Teubner, 7th (expanded) edition, 1999.

[72] B. Taylor.
Methodus Incrementorum Directa et Inversa.
London, 1715.

[73] Frank L. Pedrotti and Leno S. Pedrotti.
Introduction to Optics.
Prentice-Hall, 1987.

[74] I. N. Bronstein and K. A. Semendjajew.
Taschenbuch der Mathematik.
B. G. Teubner, 25th edition, 1991.

[75] Fritz Kurt Kneubühl.
Repetitorium der Physik.
Teubner, 2nd edition, 1982.

[76] H.J. Kreuzer.
Holographic Microscope and Method of Hologram Reconstruction.
US Patent 6/411/406 B1, 2002.

[77] H.J. Kreuzer.
Low Energy Electron Point Source Microscopy.
Micron, 26(6):503–509, 1995.

[78] Arthur L. Robinson.
X-ray Data Booklet, History of Synchrotron Radiation.
`http://xdb.lbl.gov/Section2/Sec_2-2.html`.
Accessed November 6th, 2007.

[79] HMilch.

Röntgenstrahler.
`http://de.wikipedia.org/wiki/R%C3%B6ntgenstrahler`.
Accessed February 12th, 2008.

[80] Christian Gerthsen and Helmut Vogel.
Physik.
Springer-Verlag, 17th edition, 1993.

[81] Joachim Lang.
Unterweisung für Ärzte über den Strahlenschutz in der Diagnostik mit Röntgenstrahlen.
`http://mitglied.lycos.de/DrJoachimLang/skript03.htm`.
Accessed January 29th, 2008.

[82] unknown author.
Peak brilliance of X-ray sources.
`http://www.xfel.eu/XFELpresse/en/hintergrund/was/index.html`.
Accessed October 22nd, 2007.

[83] Andreas Magerl.
Vorlesung Strukturphysik, Universität Erlangen-Nürnberg.
`http://www.lks.physik.uni-erlangen.de/struphy/Netz%20Teil2.pdf`.
Accessed October 22nd, 2007.

[84] Marcelo Alonso and Edward J. Finn.
Physics.
Addison Wesley, 1992.

[85] BESSY GmbH.
Bessy.
`http://www.bessy.de`.
Accessed February 12th, 2008.

[86] Bastian Holst.
Schematic drawing of an undulator.
`http://de.wikipedia.org/wiki/Undulator`.
Accessed October 23rd, 2007.

[87] Kwang-Je Kim.
X-ray Data Booklet, Characteristics of Synchrotron Radiation.
`http://xdb.lbl.gov/Section2/Sec_2-1.html`.
Accessed November 6th, 2007.

[88] Kai Godehusen.
Data sheet of beamline UE52-SGM at BESSY II.
`http://www.bessy.de`.
Accessed May 8th, 2007.

[89] Andor Technology.
Andor DO436, CCD camera.
`http://www.andor-tech.com`.
Data sheet.

[90] J. W. Strutt (Lord Rayleigh).
Investigations in Optics, with special reference to the Spectroscope.
Philosophical Magazine, VIII(49):261–274, 1879.

[91] J. W. Strutt (Lord Rayleigh).
On the Resolving-power of Telescopes.
Philosophical Magazine, X:116–119, 1880.

[92] Wikipedia.
Beugungsscheibchen.
`http://de.wikipedia.org/wiki/Beugungsscheibchen`.
Accessed January 29th, 2008.

[93] Wikipedia.
Rayleigh-Kriterium.
`http://de.wikipedia.org/wiki/Rayleigh-Kriterium.htm`.
Accessed January 29th, 2008.

[94] Pablo F. Meilan and Mario Garavaglia.
Braz. J. Phys. [online]. 1997, vol. 27, no. 4 [cited 2008-02-13], pp. 638-643.

[95] V. P. Nayyar and N. K. Verma.
Two-point resolution of Gaussian aperture operating in partially coherent light using various resolution criteria.
Applied Optics, 17(14):2176–2180, 1978.

[96] Michael A. O'Keefe, Lawrence F. Allard, and Douglas A. Blom.
Resolution Quality and Atom Positions in Sub-Ångström Electron Microscopy.
Microscopy and Microanalysis, 11(Suppl 2):540–541, 2005.

[97] C. M. Sparrow.
On Spectroscopic Resolving Power.
Astrophysical Journal, 447:76–86, 1916.

[98] Toshimitsu Asakura.
Resolution of two unequally bright points with partially coherent light.
Nouv. Rev. Optique, 5(3):169–177, 1974.

[99] D. Van Dyck, S. Van Aert, A.J. den Dekker, and A. van den Bos.
Is atomic resolution transmission electron microscopy able to resolve and refine amorphous structures?
Ultramicrocsopy, 98:27–42, 2003.

[100] Peter Divos.
Resolution power of digital in-line holographic microscope.
unpublished, 2007.

[101] Wikipedia.
Nyquist-Shannon-Abtasttheorem.
`http://de.wikipedia.org/wiki/Nyquist-Shannon-Abtasttheorem`.
Accessed January 29th, 2008.

[102] C. E. Shannon.
Communication in the presence of noise.

Proc. Institute of Radio Engineers, 37(1):10–21, 1949.

[103] Thomas G. Brown, Katherine Creath, and Herwig Kogelnik, editors.
The Optics Encyclopedia. Basic Foundations and Practical Applications, volume 4 [O-S].
Wiley-VHC, 2004.

[104] Melles Griot.
Commercial pinholes.
`http://www.mellesgriot.com`.
Accessed February 12th, 2008.

[105] National Aperture, Inc.
Commercial pinholes.
`http://www.nationalaperture.com/pinhole.htm`.
Accessed February 12th, 2008.

[106] Space Environment Technologies.
ISO 21348 Definitions of Solar Irradiance Spectral Categories.
`http://www.spacewx.com`.
Accessed March 9th, 2007.

[107] Xinghua Li, Takashi Abe, and Masayoshi Esashi.
Deep reactive ion etching of Pyrex glass using SF_6 plasma.
Sensors and Actuators A, 87:139–145, 2001.

[108] E. W. Becker, W. Ehrenfeld, P.Hagmann, A. Maner, and D. Münchmeyer.
Fabrication of microstructures with high aspect ratios and great structural heights by synchrotron radiation lithography, galvanoforming, and plastic moulding (LIGA process).
Microelectronic Engineering, 4:35–56, 1986.

[109] Fraunhofer Institut Integrierte Systeme und Bauelementtechnologie.
FIB Focused Ion Beam - Applications, Specifications and Principle.
`http://www.iisb.fraunhofer.de/en/arb_geb/technology_an_fib.htm#Absatz2`.
Accessed March 10th, 2008.

[110] Ilan Gavish and Yucal Greenzweig.
Focused ion beam metal deposition.
`http://www.patentstorm.us/patents/6492261-description.html`.
Accessed March 9th, 2008.

[111] Center for X-ray Optics and Advanced Light Source, Lawrence Berkeley National Laboratory.
X-ray data booklet, January 2001.

[112] Martina Schürmann.
Digital In-Line Holographic Microscopy with Various Wavelengths and Point Sources Applied to Static and Fluidic Specimens.
PhD thesis, Ruprecht-Karls-Universität Heidelberg, 2007.

[113] D.G. Robinson, U. Ehlers, R. Herken, B. Herrmann, F. Mayer, and F.-W. Schürmann.

Präparationsmethodik in der Elektronenmikroskopie.
Springer-Verlag, 1985.

[114] Wikipedia.
Mesenchymal stem cell.
`http://en.wikipedia.org/wiki/Mesenchymal`.
Accessed March 16th, 2008.

[115] Zuhal Kaya.
Entwicklung von neuen nahinfrarot emittierenden Anthrachinonfluoreszenzfarbstoffen und deren Evaluierungen in der angewandten, biologischen Grundlagenforschung.
PhD thesis, Ruprecht-Karls-Universität Heidelberg, 2008.

[116] J.A. Finlay, M.E. Callow, M.P. Schultz, G.W. Swain, and J.A. Callow.
Adhesion strength of settled spores of the green alga Enteromorpha.
Physical Review Letters, 18:251–256, 2002.

[117] Berkeley Lab.
X-Ray Attenuation Length.
`http://henke.lbl.gov/optical_constants/atten2.html`.
Accessed January 25th, 2008.

[118] National Institute of General Medical Sciences.
Inside the Cell.
`http://publications.nigms.nih.gov/insidethecell/index.html`.
Accessed March 12th, 2008.

[119] Wikipedia.
Chromosome.
`http://en.wikipedia.org/wiki/Chromosome`.
Accessed March 11th, 2008.

[120] Wikipedia.
Röntgen-Nahkanten-Absorptions-Spektroskopie.
`http://de.wikipedia.org/wiki/R%C3%B6ntgen-Nahkanten-Absorptions-Spektroskopie`.
Accessed February 18th, 2008.

[121] Joachim Stoehr.
NEXAFS Spectroscopy.
Springer-Verlag, 1992.

[122] Ivaylo Koprinarov and Adam P. Hitchcock.
X-ray Spectromicroscopy of Polymers: An introduction for the non-specialist.
`http://unicorn.mcmaster.ca/research/stxm-intro/polySTXMintro-all.htm`.
Accessed January 24th, 2007.

[123] U. Neuhäusler, S. Abend, C. Jacobsen, and G. Lagaly.
Soft X-ray spectromicroscopy on solid-stabilized emulsions.
Colloid & Polymer Science, 277(8):719–726, 1999.

[124] Adam P. Hitchcock, Cynthia Morin, Xuering Zhang, Tohru Araki, Jay Dynes, Harald Stöver, John Brash, John R. Lawrence, and Gary G. Leppard.
Soft X-ray spectromicroscopy of biological and synthetic polymer systems. *Journal of Electron Spectroscopy*, 144-147:259–269, 2005.

[125] Mark Winter.
WebElements Periodic Table.
`http://www.webelements.com/`.
Accessed February 18th, 2008.

[126] Wikipedia.
Cell nucleus.
`http://en.wikipedia.org/wiki/Cell_nucleus`.
Accessed March 12th, 2008.

List of Figures

Danke

Danke an alle, die mich im letzten Jahr in irgendeiner Weise unterstützt und direkt oder indirekt zum Gelingen dieser Arbeit begetragen haben.

Danke

... an Prof. Dr. Michael Grunze für die Aufnahme in die Arbeitsgruppe.
... an Prof. Dr. Annemarie Pucci für die Bereitschaft, die Betreuung von Seiten der Fakultät für Physik zu übernehmen.
... an Dr. Axel Rosenhahn für die Betreuung.
... an den gesamten Arbeitskreis Grunze für die kollegiale Atmosphäre.
... an das Team aus der Verwaltung, Edeltraud Boczek, Robert Läufer, Benjamin Scherke, Andrea Miech, Swetlana Duchnay, Waldemar Fröschen und Stefan Haßlinger, für all die Arbeit, die man als Doktorand nicht immer sieht.
... an das technische Team, Reinhold Jehle, Peter Jeschka und Günter Meinusch, für Ratschläge und Unterstützung.
... an Georg Albert für das Bedampfen der Goldfolien.
... an die Werkstatt des Instituts für die Anfertigung diverser Bauteile.
... an Dr. Tamás Haraszti und Simon Schulz vom AK Spatz für diverse Mikroskopiebilder.
... to Prof. Dr. H. Jürgen Kreuzer for sharing with us his knowledge about holography and his reconstruction algorithm.
... an Prof. Dr. Zabel für die Bereitstellung der Alice-Kammer.
... an Dr. Kai Godehusen für den Beamline support.
... an Dr. Stefan Eisebitt und seine Jungs für die Unterstützung und tatkräftige Hilfe während der Strahlzeiten am BESSY.
... an Prof. Dr. Silvia Mittler und ihre Familie für die Einladung nach London (Canada!).
... to Dr. Todd Simpson for everything he taught me about FIB milling.
... an Reiner Dahint, Alex Küller, Fanny Liu, Sören Schilp, Martin Schmid und Martin Schmidt für all die netten Unterhaltungen zwischendurch.
... an Jörg Fick, Marco Maccarini, Svetlana Stoycheva und Elka Trileva, die ehemaligen aus 229, für all den Spaß, den wir zusammen hatten.
... an die aus 229, die noch da sind, dafür, dass man nicht immer nur über die Arbeit redet.
... an Xinyu Cao und Florian Staier, für das geteilte Leid bei den Strahlzeiten.
... an Reiner Dahint fürs Unterschreiben der Urlaubsanträge.

. . . an Axel Rosenhahn für das nötige Verständnis und das verständnislose Kopfschütteln.
. . . an Martina Schürmann für die gemeinsame Zeit.
. . . an Andrea Seehuber, Sebastian Weisse und Matthias Heydt für all die Kaffeepausen und Lästerrunden.
. . . an meine Korrektur-Helden Sebastian, Matthias und Axel. Ohne euch wäre ich verloren gewesen.
. . . an meine Freunde, die ich in den letzten Monaten stäflichst vernachlässigt habe, in der Hoffnung, dass sie mir das nachsehen.
. . . an meine Familie, die immer für mich da ist und auf die ich mich immer verlassen kann.
. . . an Dennis — ohne Worte.